DEVELOPMENT OF PHYSIOLOGICALLY REALISTIC *IN VITRO* MODELS OF THE GASTROINTESTINAL TRACT

A Dissertation

Presented to the Faculty of the Graduate School

of Cornell University

In Partial Fulfillment of the Requirements for the Degree of

Doctor of Philosophy

by

Gretchen Jennifer McAuliffe

May 2008

DEVELOPMENT OF PHYSIOLOGICALLY REALISTIC *IN VITRO* MODELS OF THE GASTROINTESTINAL TRACT

Gretchen Jennifer McAuliffe, Ph. D.

Cornell University 2008

The gastrointestinal (GI) tract is the largest surface exposed to the environment in the human body. Intestinal absorption is the entry route for most essential nutrients and the preferred method for pharmaceutical administration. Understanding how compounds interact with and are absorbed through the small intestinal epithelium, and how they go on to affect the rest of the body, is crucial for nutritional and toxicological evaluation. Our group has developed an *in vitro* cell culture model of the gastrointestinal tract that includes digestion and physiologically realistic cell populations with a mucus layer. The applications of this model include predicting iron bioavailability, studying the effects of oral exposure to nanoparticles, and measuring the metabolism and toxicity of ingested chemicals or drugs.

Co-cultures of absorptive and mucus-producing cells were incorporated into an existing *in vitro* digestion/cell culture model used to assess iron bioavailability. At physiologically relevant ratios of Caco-2 absorptive cells to HT29-MTX mucus-producing cells, a mucus layer completely covered the cell monolayer and the *in vitro* digestion model was nearly as responsive to changes in sample iron bioavailability as pure Caco-2 cultures. The existing *in vitro* digestion/Caco-2 cell culture model correlates well with human iron bioavailability studies, but, as mucus appears to play a role in iron absorption, the addition of a physiologically realistic mucus layer and goblet-type cells to this model may give more accurate iron bioavailability predictions.

An *in vitro* cell culture model of the intestinal epithelium with absorptive,

goblet, and M cells was used to study the effects of nanoparticle exposure on iron uptake and transport. Polystyrene 50 nm and 200 nm particles were found to interfere with cellular iron uptake and transport, indicating that oral exposure to nanoparticles could potentially have an effect on the normal physiological functions of intestinal epithelial cells. These preliminary results suggest that nanoparticle size, concentration, and charge can influence the uptake and transport of iron.

Microscale cell culture analogs (μCCAs) are used to study the metabolism and toxicity of a chemical or drug. These *in vitro* devices are physical replicas of physiologically based pharmacokinetic models that combine microfabrication and cell culture. A GI tract μCCA, together with a multi-chamber silicon chip μCCA, has been used to recreate the toxic effects of acetaminophen. Proof of concept experiments show that acetaminophen passes through the *in vitro* intestinal epithelium and is metabolized by liver cells, resulting in liver cell toxicity.

BIOGRAPHICAL SKETCH

Gretchen Jennifer McAuliffe was born on November 21, 1979 in Greenfield, Massachusetts to Michael and Nora McAuliffe. She was the first of three children and the older sister of Jessica and Maxwell McAuliffe. Gretchen grew up in Turners Falls, Massachusetts, where she attended school and learned to love science. In 1998, Gretchen graduated as the valedictorian from Turners Falls High School, and later that year she began college at the University of Massachusetts Amherst in the chemical engineering program. She met Jason Mahler, her future husband, in September of 2001 at a friend's birthday party. In 2002, Gretchen graduated with honors from the University of Massachusetts Amherst with a Bachelor of Science degree in chemical engineering. She moved to Ithaca that summer to begin work on her doctorate in the School of Chemical and Biomolecular Engineering at Cornell University with Dr. Michael Shuler as her advisor. Gretchen defended her thesis in February of 2008 and will begin a postdoctoral research position in March of 2008 with Dr. Jonathan Butcher in the Biomedical Engineering Department at Cornell University.

ACKNOWLEDGEMENTS

I would first like to first acknowledge my thesis advisor, Dr. Michael Shuler, for guiding my research while still allowing me a great deal of freedom. Working with him has allowed me to become an independent, thoughtful researcher. I would also like to thank my committee members, Dr. Ray Glahn, for allowing me full access to his laboratory and many useful research meetings; Dr. Dave Putnam, for teaching a great drug delivery class, offering constructive laboratory advice, and sharing lab equipment; and Dr. Wayne Schwark for being an excellent pharmacology teacher.

There were many people who provided time and energy toward the completion of this project. I am grateful to have been a part of the Shuler research group, and especially would like to thank the μCCA group (Dan, Hui, and Jay) for their help and suggestions. The μCCA chip design calculations in Appendix B were based on calculations previously done by Dan Tatosian, and the PBPK model in Chapter 4 and Appendix C was based on a PBPK model developed by (Jay) Jong Hwan Sung. The Shuler group staff has been wonderful to work with; Paula Miller has been an excellent resource for cell culture training and general lab knowledge and Bonnie Sisco keeps everything running smoothly. Glenn Swann fabricated the GI tract μCCA devices and chip μCCA housings and has been instrumental in this work. I am thankful for his patience and expertise. Mary Bodis, Pei Pei Cheng and Zhiqiang Cheng provided technical support in the Glahn lab and were a pleasure to work with. Jung Yun Chang, a visiting scientist from the KFDA, was responsible for the design of the first generation GI tract μCCA and the idea to use acetaminophen as a model drug. Mandy Esch, a postdoctoral researcher in the Shuler lab, fabricated the second generation μCCA chips. The HT29-MTX cell line was kindly contributed by Dr. Thécla Lesuffleur of INSERM U560 in Lille, France.

Financial support for this work was provided by the Nanobiotechnology Center (NBTC), an STC Program of the National Science Foundation, under Agreement No. ECS-9876771; the New York State Office of Science, Technology and Academic Research (NYSTAR) program through a grant to MLS as a NYSTAR Distinguished Professor; and Army Corp of Engineers under Agreement ID W9132T-07-2-0010. Parts of this work were performed at the Cornell NanoScale Facility, a member of the National Nanotechnology Infrastructure Network that is supported by the National Science Foundation (Grant ECS-0335765), and the USDA-ARS US Plant, Soil and Nutrition Laboratory.

Ithaca has been a great place to live because of the people I have met here and spent time with. I can't list everyone, but a special thanks to Toby, Dave, Bettina, and Sharon for making first year less painful; Jordan and BJ for being great officemates; Tricia and Connor for some excellent dinners; Ginny, Mike, and Amy for being friends with nothing to do with Cornell; and Jill, Jerry, Maegan, and Kevin for coming up to visit and starting the annual Central New York wine tour.

I would like to finish by thanking my family because they are largely responsible for the person I am today. I am grateful to my parents for allowing me the freedom to make my own decisions, but never denying me any opportunity. I am proud to be a McAuliffe with siblings like Jessica and Max, who are good people and also incredibly fun to be around. I am thankful to Suz, Gary, Andrea, Jim, Owen, Olivia, Bruce, and Peg for making me a part of their family. Finally, I am grateful to my future husband, Jay Mahler, for his help, his encouragement, his cooking, and for being my best friend.

TABLE OF CONTENTS

LIST OF FIGURES

Chapter 4.

Chapter 5.

Appendix A.

LIST OF TABLES

LIST OF ABBREVIATIONS

AA	Ascorbic acid
ADMET	Absorption, distribution, metabolism, elimination, toxicity
AP	Apical
APAP	Acetaminophen
APAP-GLUC	Acetaminophen glucuronide
APAP-SULF	Acetaminophen sulfate
AUC	Area under the curve
BA	Basolateral
CCA	Cell culture analog
CYP	Cytochrome P450
DMEM	Dulbecco's Modified Eagle Medium
FBS	Fetal bovine serum
Fe	Iron
GI	Gastrointestinal
HSF	Horse spleen ferritin
MCB	Monochlorobimane
μCCA	Microscale cell culture analog
MEM	Minimal essential medium
MWCO	Molecular weight cut-off
NAPQI	N-acetyl-*p*-benzoquinone
PBPK	Physiologically based pharmacokinetic
PBS	Phosphate buffered saline
TER	Transepithelial electrical resistance

CHAPTER 1

INTRODUCTION TO *IN VITRO* MODELS OF THE GASTROINTESTINAL TRACT

1.1. Motivation

The lining of the gastrointestinal (GI) tract is the largest surface exposed to the external environment in the human body [1]. One of the main functions of the small intestine is absorption, and intestinal absorption is the route used by most essential nutrients and many pharmaceuticals to enter the body [2]. Understanding the effects of digestion, how compounds interact with and are absorbed through the small intestinal epithelium, and how these compounds go on to affect the rest of the body is therefore critical for nutritional and toxicological evaluation. The goal of this project is to create physiologically realistic *in vitro* models of the human GI tract that provide rapid, inexpensive, and accurate predictions of the digestion, absorption, cellular response to, and interactions between ingested compounds.

1.2. Relevant GI tract anatomy and physiology

Soon after food enters the stomach it is mixed with gastric juice to form a viscous, acidic mixture called chyme. The main components of gastric juice are hydrochloric acid (HCl), which is secreted by parietal cells, pepsin, which is secreted by chief cells as the inactive proenzyme pepsinogen, and gastric lipase [2]. The acidic environment created by HCl kills many of the microbes present, partially denatures proteins and inactivates most enzymes in the food, helps to break down the connective tissue in meat and plant cell walls, and converts pepsinogen into pepsin [2]. The protein-digesting enzyme pepsin, which is most effective at pH 2 and inactivated at

higher pH, digests peptide chains in chyme into smaller peptide fragments [3]. Gastric lipase digests triglyciderides into fatty acids and monoglycerides [3].

Acidic chyme entering the duodenum stimulates duodenal enteroendocrine cells to release secretin, which promotes the secretion of bile and buffering bicarbonate (HCO_3^-) ions by the liver and pancreas [2]. Amino acids from partially digested proteins and fatty acids from partially digested triglycerides trigger the release of cholecystokinin (CCK) by enteroendocrine cells [3]. CCK activates both the secretion of pancreatic juice, which is rich in digestive enzymes, and the ejection of bile, which aids in the emulsification, digestion, and absorption of fats [3].

Almost all absorption and chemical digestion occur in the small intestine, and its structure is specifically adapted for these functions. The small intestine is approximately 600 cm long, 2.5 to 4 cm in diameter, and divided into three unequal sections: the duodenum, the jejunum, and the ileum [2]. The duodenum receives chyme from the stomach and is ~25 cm long, the jejunum follows the duodenum and is ~250 cm long, and the ~350 cm long ileum is the last section [4]. The surface area in the small intestine available for digestion and absorption is ~$2x10^6$ cm^2 due to circular folds (10 mm high ridges) and villi (0.5-1 mm high fingerlike projections) along the intestinal wall and microvilli on the apical cell membrane of absorptive enterocytes, although most absorption occurs in the duodenum and proximal jejunum [4, 5]. The apical surface of the intestinal epithelium faces the intestinal lumen, while the basolateral surface faces the body cavity and is responsible for the exchange of molecules between the intestine and the rest of the body. Segmentation (annular contraction of smooth muscle) and peristalsis (successive waves of smooth muscle contraction) within the intestine mix chyme with digestive juices, bring food into contact with the intestinal epithelium for absorption, and propel chyme through the small intestine [5].

The membrane lining the small intestine is composed of more than 8 different cell types that are joined together by tight junctions, which are proteins that interconnect epithelial cells to reduce passive diffusion between the cells [6]. Absorptive enterocytes make up about 90% of the cell population in the upper intestine and are covered with 1 μm long, tightly packed microvilli that contain digestive enzymes; the metabolizing microvilli form a brush border [7]. Absorptive cells allow the passage of small molecules by one or more of four different routes: passive transcellular (through the cell), passive paracellular (between cells), active (energy-dependent) carrier-mediated, and transcytosis (transport across the epithelium with uptake into coated vesicles) [8]. Goblet cells are the second most common cell type in the human small intestine, with the ratio of goblet cells ranging from 10% in the small intestine to 24% in the distal colon [9]. Goblet cells secrete mucus, which is largely composed of heavily glycosylated proteins, providing a barrier that prevents viruses, bacteria, and large molecules from reaching the membrane surface [10]. The mucus also lubricates the epithelial surface, protects the epithelial cells from mechanical damage by solid food, protects the cells from chemical damage due to the influx of acid from the stomach, and aids in the digestion process by immobilizing enzymes near the epithelium surface, which allows for better nutrient hydrolysis and absorption [10, 11]

The connective tissue layer (lamina propria) of the intestinal membrane contains B and T lymphocytes, which are the cells that produce antibodies and destroy infected cells, respectively [7]. Clusters of B and T cells in the connective tissue are called aggregated lymphatic follicles, or Peyer's patches, and overlying the Peyer's patches are M cells [7]. Human M cells have small folds over their luminal surface instead of microvilli, produce almost no digestive enzymes, and are located near very few mucus producing cells [12]. These features allow microorganism and

macromolecule approach and adherence to the M cell surface. M cells also contain only a few lysosomes, which permits the transcytosis of attached macromolecules and microorganisms in almost un-degraded form. After M cell transport across the intestinal epithelium the antigens are taken up and processed by macrophages and presented to T lymphocytes, which stimulate B lymphocytes to produce antibodies [12].

M cells and the immune-associated cells in the lamina propria form the gut-associated lymphoid tissue or GALT. The lining of the gastrointestinal tract is the largest vulnerable surface facing the external environment and it must defend the body against many potentially toxic substances in food or produced by bacteria [1]. The GALT is the defense mechanism the small and large intestines have developed for defending the epithelial membrane. Overall, 70-80% of the immune cells of the body are in the gut [13].

1.3. In vitro models of the GI tract

1.3.1. In vitro digestion model

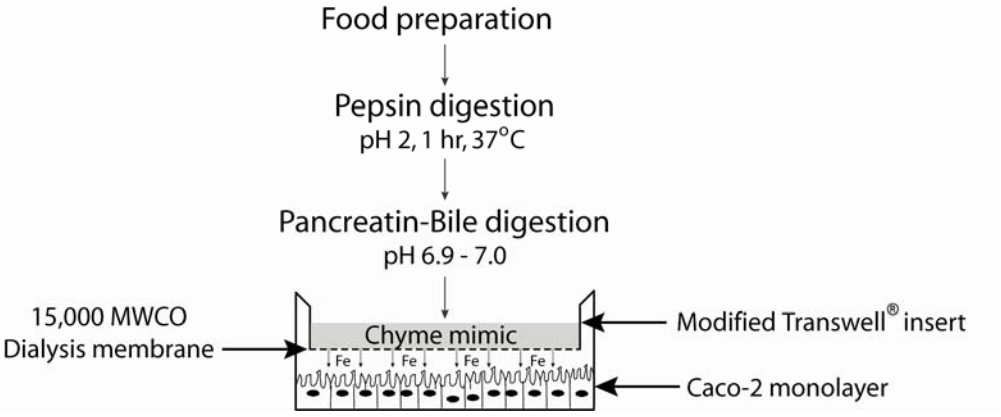

Figure 1.1. Schematic of the *in vitro* digestion/Caco-2 cell culture model used for evaluating iron bioavailability developed by Glahn et al. [14].

An *in vitro* digestion/Caco-2 cell culture model has been developed by Glahn et al. for studying iron bioavailability from food (Figure 1.1) [14]. The food of interest is cooked and freeze dried before it is subjected to an hour-long digestion at 37^{o}C and pH 2 with porcine pepsin. The pepsin is then deactivated by raising the pH to 5.5-6.5 with sodium bicarbonate, a porcine pancreatin-bile solution is added to the mixture, the pH is readjusted to 7.0 with sodium bicarbonate, and the chyme mimic is placed into 15,000 molecular weight cut-off (MWCO) dialysis membrane inserts above a Caco-2 human colon carcinoma cell monolayer. The 15,000 MWCO membrane on the insert prevents large particles from reaching the cells and protects the cells from digestive enzymes in the mixture. After 2 hours, the insert and food mixture are removed from the cells, and after another 22 hours the cells are harvested, lysed, and cell protein content and ferritin assays are performed.

1.3.2. In vitro models of the intestinal epithelium

Figure 1.2. Diagram of intestinal epithelial cells grown in a Transwell insert. The top or apical chamber represents the intestinal lumen, and the bottom or basolateral chamber corresponds to the capillary network surrounding the small intestine.

The most common *in vitro* model for the intestinal epithelium involves culturing intestinal epithelial cell lines on semi-permeable membrane inserts that divide the wells of the culture plate into apical (top) and basolateral (bottom) chambers separated by the confluent monolayer of epithelial cells grown on the membrane (Figure 1.2). When seeded onto Type I collagen-coated plates or polycarbonate membranes under normal culture conditions, Caco-2 cells differentiate

into a polarized, absorptive enterocyte-like epithelial barrier that is morphologically and biochemically very similar to the small intestinal epithelium [15]. Type I collagen is used to model the epithelial basement membrane because it has been found to best stimulate proliferation, cell spreading, and differentiation in static Caco-2 cultures [16]. After a growth period of two to three weeks, the Caco-2 monolayers express tightly packed microvilli, tight junctions, and are capable of paracellular, transcellular, active, and transcytotic transport [8, 17]. Any material that is absorbed in the intestine must first diffuse across the mucus layer, the epithelial cells lining the intestine, the lamina propria, and the endothelial cells that line the capillaries [3]. The epithelial cell layer, however, has been shown to be the rate-limiting step and, therefore, the use of Caco-2 cells is appropriate for nutrient and drug absorption studies [18].

Goblet cells can be mimicked *in vitro* using mucus secreting cell lines such as HT29-MTX. HT29-MTX are a subpopulation of HT29 human colonic adenocarcinoma cells, which, after a slow adaptation to methotraxate (MTX), consist exclusively of differentiated, gastric-like mucus secreting, goblet-type cells that retain their differentiated phenotype after reversion to MTX-free medium [19, 20]. Co-cultures of Caco-2 and HT29-MTX represent the two major cell types (absorptive and goblet) found in the small intestinal epithelium.

The co-culture of Caco-2 cells with the Raji B-cell lymphoma cell line has been shown to induce the differentiation of Caco-2 epithelial cells into cells with an M cell-like morphology, including up-regulated Sialyl Lewis A antigen, β1 integrin localization on the apical pole of the cells, loss of microvilli, and increased particle transport (Figure 1.3A and 1.3C) [21, 22]. Using an inverted *in vitro* M cell model (Raji cells were cultured on top of Caco-2 monolayers instead of in the basolateral Transwell chamber, Figure 1.3B) it was found that between 15 and 30% of the Caco-2 cells differentiated into M cells [23].

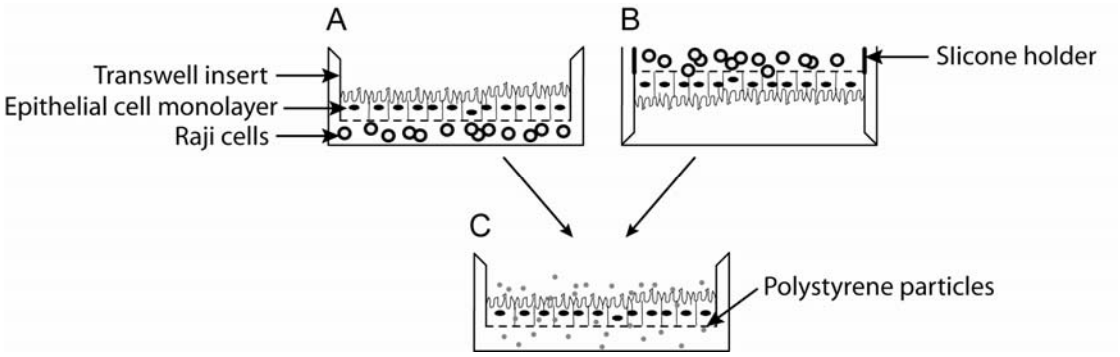

Figure 1.3. *In vitro* M cell models. (A) Caco-2 cells are cultured on a Transwell insert and M cell differentiation is induced by culturing the Raji B cell line in the basolateral chamber. The M cell culture discussed in Chapter 3 was performed in this orientation. (B) The inverted *in vitro* M cell model developed by des Rieux et al. [23]. A silicone holder allows the Raji cells to be cultured on top of the basolateral side of the Caco-2 monolayer. (C) Particle transport studies are performed with the Caco-2 monolayer in the upright position.

A frequently used method for evaluating epithelial monolayer integrity and tight junction functionality is measuring the transepithelial electrical resistance or TER. TER is a measurement of ion permeability across the cell monolayer, and is assessed by passing a current across monolayers grown on permeable membrane inserts and measuring the resulting voltage across the cells. The resistance is then calculated using Ohm's law, which states that resistance = voltage/current. The TER across Caco-2 monolayers generally increases with culture time and reaches a maximum after approximately 9 days. TER values of Caco-2 monolayers depend on the surface area of the Transwell inserts, filter support material, culture conditions, and especially passage number of the cells, and have been reported to range between 150 and >1400 Ω/cm^2 [24].

1.4. Iron absorption across the intestinal epithelium

1.4.1. Iron absorption in vivo

Iron is an essential nutrient in the body that is absorbed from food through the

intestinal epithelium, but there is a delicate balance between iron absorption, utilization, and loss [25]. An excess of systemic iron exceeds the capacity of the proteins that sequester it and catalyzes the formation of free radicals [26]. Free radicals go on to attack cell membranes, proteins, and DNA, causing tissue damage. A lack of iron, on the other hand, results in anemia, which is characterized by not having enough hemoglobin to adequately oxygenate tissues [26]. Because the body has no significant mechanism for eliminating excess iron, iron balance is dependent on tightly linking body iron requirements with intestinal iron absorption from food.

The percentage of iron absorbed from a meal (i.e. bioavailability) partly depends on dietary composition. Meat, poultry, and fish all contain heme iron, which is two to three times more absorbable than the nonheme iron found in plant-based and iron fortified foods [27]. The bioavailability of nonheme iron is affected by other foods ingested in the meal. Nonheme iron absorption enhancers include heme iron from meat and vitamin C or ascorbic acid, which has the ability to chelate iron and promotes nonheme iron reduction [27-29]. Inhibitors of iron absorption include the polyphenols found in some vegetables, tannins in tea, phytates in bran, and calcium [30, 31].

Most iron absorption takes place in the proximal small intestine, near the gastro-duodenal interface [32]. There are currently heme, ferrous, and ferric iron absorption pathways that have been identified in the intestinal epithelium. Heme iron is transported into enterocytes intact through the heme carrier 1 (HCP1) protein [33]. Inorganic, nonheme iron, which is mostly in the Fe^{3+} form, is reduced to the ferrous state by the ferrireductase duodenal cytochrome B (Dcytb) [34]. Fe^{2+} is transported into the cell by divalent metal iron transporter 1 (DMT1) [35]. In the IMP or integrin-mobileferrin pathway, ferric iron is transported across the apical surface of intestinal cells by β3-integrin and mobilferrin before cytosolic reduction by paraferritin [36, 37].

Once inside the cell, some iron is stored within ferritin and some is exported as Fe^{2+} across the basolateral membrane through the basolateral iron transport protein ferroportin 1 (FPN1) [38]. Fe^{2+} must be oxidized to Fe^{3+} by hephaestin (Heph) and ceruloplasmin (Cp) in order to bind transferrin, the blood iron carrier protein [39, 40]. Figure 1.4 is a diagram of the major iron uptake, storage, transport, and carrier proteins.

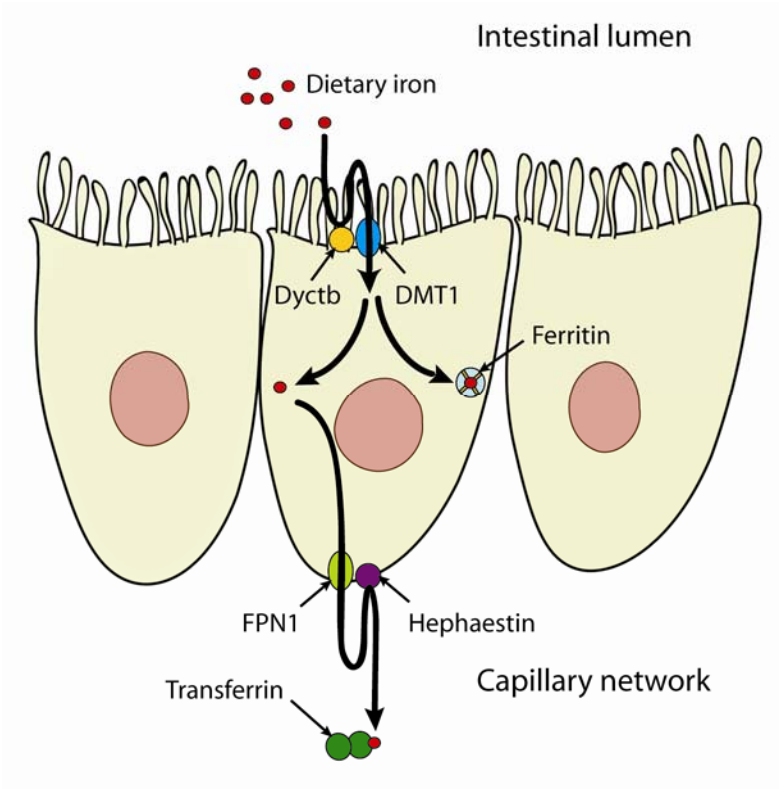

Figure 1.4. Iron uptake, storage, transport, and carrier proteins in the small intestinal epithelium.

Understanding of the molecular mechanisms involved in iron absorption by duodenal enterocytes has increased dramatically, but the mechanism by which iron is transported from the apical pole of enterocytes to the basolateral membrane is only beginning to become clear. There is evidence for an endocytic/exocytic cycling mechanism involving apotransferrin, or transferrin that does not contain bound iron, which stimulates transepithelial iron transport in a dose-dependent manner when

added to the basolateral surface of Caco-2 monolayers [41-43]. The apotransferrin containing endosomes are routed towards the apical pole of the cell where they co-localise with DMT1 that has endocytosed from the apical surface [44]. It has been proposed that during the endosome co-localization, Fe^{2+} bound by DMT1 is oxidized to Fe^{3+} by Heph and transferred to apotransferrin [45]. The newly formed holotransferrin, or iron saturated transferrin, then cycles out to the blood. Experiments using a combination of biochemical inhibitors to disrupt the vesicular network in Caco-2 cells have shown that this pathway may account for as much as 50% of the transepithelial iron transport [45, 46].

The mucus layer covering the intestinal epithelium is also thought to play a role in iron absorption. Some ingested metals remain soluble throughout the 1-8 pH range of the GI tract (Na, Mg, and Ca), but others (Al, Cu, Fe, Mn, and Zn) are susceptible to hydroxy-polymerization, which is the formation of insoluble metal hydroxides that cannot be absorbed [47]. Hydroxy-polymerization occurs when, in the absence of soluble ligands, acid soluble Al, Cu, Fe, and Zn form hydroxide precipitates as the intestinal lumen pH increases. Work by Conrad et al. has shown that mucins, which are the heavily glycosylated proteins secreted by goblet cells, bind iron at an acidic pH when iron is soluble and prevent iron precipitation as the pH in the small intestine increases [48]. These findings, along with the ability of mucin to accept iron from ascorbate, fructose, and histidine chelates at neutral pH, suggest that mucin presents iron to the intestinal mucosa in an acceptable form for absorption [49]. More recently two main iron transport proteins, DMT1 and mobilferrin, were found to be concentrated in mucin vesicles near the luminal surface, strengthening the role of mucin in iron uptake [50]. All of these attributes illustrate that mucus plays an essential role in human nutrition and health. The concentration of mobilferrin and DMT1 found in mucin and the ability of mucin to stabilize soluble iron as the luminal

pH rises and to accept iron from chelates, however, also indicate that mucus influences iron bioavailability.

1.4.2. In vitro iron absorption models

Halleux and Schneider were the first to propose the use of Caco-2 cells cultured on permeable membranes for iron absorption studies [51]. Alvarez-Hernandez et al. found that there was significantly more $^{59}Fe^{2+}$ uptake and transport by Caco-2 monolayers when compared with $^{59}Fe^{3+}$ [52]. Iron deficient cells also took up and transported more iron than cells grown in iron-rich medium, which agreed with results in humans and animals [52]. Later experiments showed that Caco-2 cells express Dcytb, DMT1, ferritin, FPN-1, Heph, and synthesize and secrete transferrin, which are all of the major iron uptake, storage, transport, and carrier proteins [51, 53].

Models that combine Caco-2 cells and *in vitro* digestion measure iron bioavailability from food due to both iron solubility and iron uptake by a living component. Gangloff et al. developed an *in vitro* digestion/Caco-2 cell culture model for predicting iron bioavailability from food that demonstrated the enhancing effect of ascorbic acid and beef on Caco-2 cell ^{59}Fe uptake, which is in agreement with *in vivo* observations. Glahn et al. showed that ^{59}Fe uptake by Caco-2 cells from extrinsically labeled foods in an *in vitro* digestion/Caco-2 model corresponded with *in vivo* studies [54, 55]. Glahn et al. later eliminated the need for extrinsic food labeling by showing Caco-2 ferritin formation accurately predicts iron bioavailability from food [14].

1.5. Nanoparticle transport across the intestinal epithelium

1.5.1. Nanoparticle absorption in vivo

In animal studies, orally delivered particles are taken up by both M cells and absorptive enterocytes *in vivo* [56]. Oral administration of nanoparticles to rats has

shown that differences in particle uptake and distribution are due to hydrophobicity, particle shape, particle size, and surface chemistry [57, 58]. Water soluble, ultrafine (<0.1 μm) ^{192}Iridium and C_{60} fullerene nanoparticles were not significantly absorbed through the rat GI tract [59-61]. Water insoluble titanium dioxide (TiO_2) particles in the 150-500 nm range, however, were absorbed into the blood stream and found in rat liver, spleen, lung, and peritoneal tissue [62]. The water insoluble, lipophilic particles most likely passively diffuse via the transcellular route. Pontefract et al. found 0.2-2 μm long asbestos fibers in the air and city drinking water [58]. After finding a 23.55 μm long fiber in a rat's blood stream, Pontefract et al. concluded that smaller fibers pass through the intestinal wall by pinocytosis, while larger fibers pierce the epithelium like a needle [58]. The uptake of orally delivered polystyrene nanoparticles in rats showed a size and surface charge dependent trend. In experiments with non-ionized particles, 6.6% of 50 nm particles, 5.8% of 100 nm particles, 0.8% of 1 μm particles, and 0% of 3 μm particles were taken up into rat liver, spleen, blood, and bone marrow [63]. Carboxylated polystyrene particles were less well absorbed than non-ionized particles of the same size [64]. The gastrointestinal tract epithelial cells carry a negative charge on their surface due to the presence of negatively charged protein residues and selective active ion pumps in the cell membranes [65]. The mucus that covers the intestinal epithelial surface also has a negative charge, and the charge of the epithelial cell membrane and mucus could contribute to the increased absorption of non-ionized or positively charged particles when compared with negatively charged particles.

Fine (1.0-0.1 μm) and ultrafine (<0.1 μm) particles primarily composed of TiO_2 and aluminosilicates are food additives that account for the ingestion of 10^{12}-10^{14} particles per day for the average person in a developed country [66]. These particles are resistant to gastrointestinal degradation and are taken up by M cells and passed on

to underlying macrophages [67]. The inorganic microparticles are also resistant to macrophage degradation, therefore human intestinal lymphoid aggregates often appear pigmented due to particle accumulation [68, 69].

1.5.2. In vitro nanoparticle uptake and transport studies

The use of *in vitro* cell culture models of the intestinal epithelium for studying orally delivered nanoparticle uptake and transport is widespread. A study by Behrens et al., however, showed that including mucus in the *in vitro* intestinal epithelial models is critical when evaluating the uptake and transport of hydrophobic particles [70]. Behrens et al. studied the effects of a mucus layer on particle transport in Caco-2 absorptive and MTX-E12 goblet-like intestinal cell models [70]. It was found that the presence of mucus decreased the association of non-ionized, 200 nm polystyrene nanoparticles with cell cultures by 60%, suggesting that mucus provides a barrier to hydrophobic particle absorption.

des Rieux et al. used an *in vitro* model of Caco-2 monolayers containing M cells to study polystyrene nanoparticle transport [71]. Smaller size and positive charge were both shown to increase the transport of nanoparticles through monolayers with M cells, which agrees with *in vivo* observations. A later study by des Rieux at al. determined that the transport of polystyrene particles by M cells occurred by non-specific absorptive endocytosis through a non-clatherin dependent route that was most likely macropinocytosis [23].

1.5.3. Nanoparticle toxicity after oral exposure

There have been few studies on the acute toxicity or chronic effects related to oral exposure to nanoparticles. Chen et al. found that orally delivered copper nanoparticles, but not copper microparticles, were toxic to mice [72]. The kidney, liver, and spleen were found to be target organs of the copper nanoparticles. Gerhart et

al. observed that chronic administration of 125 μm coal particles to fat-head minnows (*Pimephales-promelas*) resulted in increased mucus secretion from goblet cells, which is consistent with the idea that mucus secretion is a mechanism for protecting the intestinal lumen from abrasion [73]. Jani et al. showed that orally administered 50 nm polystyrene nanoparticles translocated to rat liver, spleen, and bone marrow and later showed that 500 nm TiO_2 particles reached to the liver, spleen, and lungs [62, 64].

Humans in developed nations regularly ingest TiO_2, silicates, and aluminosilicates nanoparticles, and these particles accumulate at the base of Peyer's Patches [67]. The ingestion of these particles has been hypothesized to promote the development of Crohn's disease, which is characterized by transmural inflammation of the GI tract that first appears over Peyer's patches [66]. This link is uncertain because there was no difference in microparticle consumption found between healthy patients and those with Crohn's disease, and limiting the amount of microparticles in the diet of Crohn's disease patients resulted in no improvement in their symptoms [74, 75]. A recent study, however, showed that dietary microparticles that interact with macrophages may increase the antigenic response toward bacterial antigens in the GI tract [76].

1.6. Drug transport across the intestinal epithelium

1.6.1. Oral drug transport in vivo

The majority of cells in the duodenum and proximal jejunum, which is where most absorption takes place, are absorptive enterocytes, and these cells are responsible for most drug absorption (Figure 1.5) [7]. The intestinal epithelium provides both a physical and biochemical barrier to orally administered drugs. The tight junctions formed between cells and hydrophobicity of the cell membranes provide a physical barrier, while the digestive and metabolizing enzymes expressed by enterocytes form a

biochemical barrier. Human absorptive enterocytes express digestive enzymes such as peptidases, esterases, and lipases; phase I cytochrome P450 (CYP) metabolizing enzymes; and phase II metabolizing enzymes such as UDP-glucuronyltransferase, N-acetyltransferase, sulfotransferase, and glutathione-S-transferase [77, 78]. Enzymes in the CYP superfamily oxidize compounds, especially chemicals or drugs that are hydrophobic and relatively insoluble, to form a reactive intermediate [79]. The reactive intermediate is then susceptible to conjugation by phase II enzymes [80].

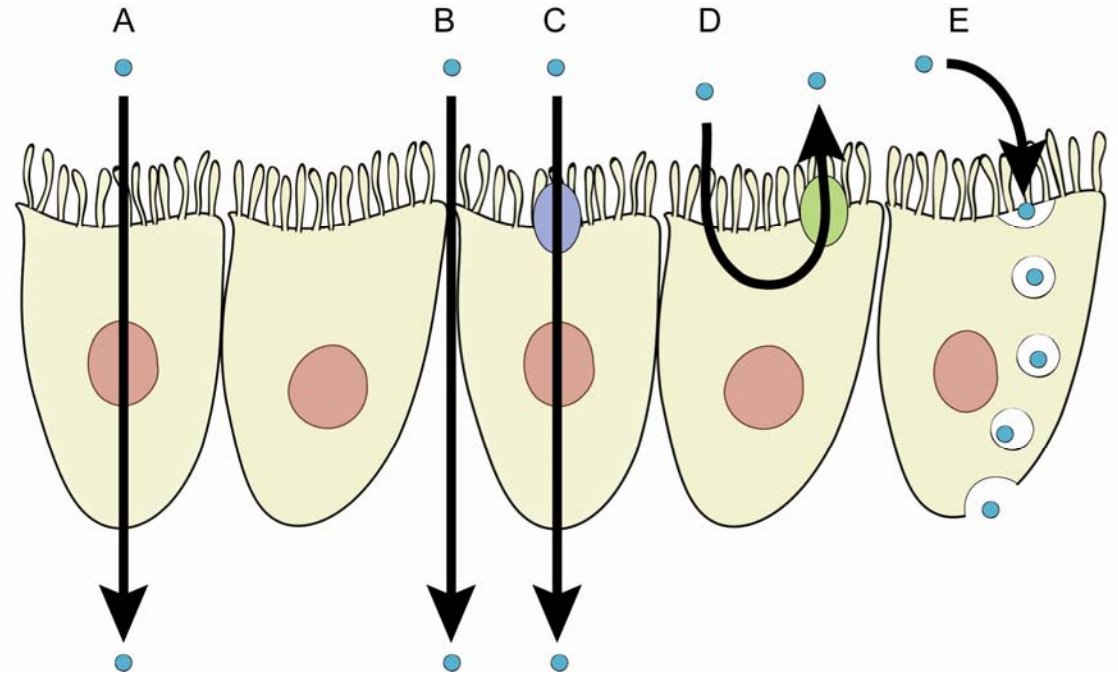

Figure 1.5. Drug absorption pathways through absorptive enterocytes in the small intestinal epithelium. (A) passive transcellular, (B) passive paracellular, (C) active carrier-mediated, (D) apical efflux, and (E) transcytosis.

Absorption of small lipophilic molecules occurs mainly by passive transcellular diffusion, and these drugs are rapidly and completely absorbed [8]. Small hydrophilic drugs and peptides partition poorly into cell membranes and this type of drug is most likely transported through the water filled pores of the paracellular pathway [8]. Some nutrients, vitamins, and their structural analogs are transported

across the epithelium by active, carrier-mediated transport [8]. Two families of apical efflux transporters, multidrug resistance (MDR) and multidrug resistance-associated protein (MRP), export drugs out of enterocytes and back into the intestinal lumen [81, 82]. P-glycoprotein (P-gp), which is the product of the MDR1 gene and one of the most studied apical efflux transporters, has been shown to limit the absorption of many drugs [77]. Macromolecular drugs can be transported by enterocytes via transcytosis across the intestinal epithelium, but low transport capacity and proteolytic enzymes within vesicles make this route less attractive for oral drug delivery [83]. Transcytosis of macromolecules is more effective in M cells, as this cell type has lower vesicle proteolytic activity and a higher transport capacity [12]. The low number of M cells in the human intestinal epithelium (<10%), however, makes this pathway viable only for highly potent drugs such as peptide antigens [8, 84].

Blood that reaches the liver from the portal vein is derived from splanchnic circulation, which includes blood flow from the stomach, small intestine, large intestine, pancreas, and spleen [85]. Once a drug has absorbed across the small intestine and reached the blood within the surrounding capillary network, it is immediately delivered to the liver, which is a phenomenon called first pass metabolism. The result of first pass metabolism can be an extensively reduced concentration of bioavailable, active drug due to phase I and phase II liver metabolism.

1.6.2. In vitro orally administered drug transport studies

Caco-2 cells have been found to express a number of phase I drug metabolizing genes including CYP1A1, CYP1A2, CYP2C8-19, CYP2D6, CYP2E1, and CYP3A5 [86]. Expression of CYP3A4 and CYP2B6/7, however, was below the detection limit. Caco-2 cells were also found to have measurable UDP-

glucuronyltransferase, N-acetyltransferase, sulfotransferase and glutathione-S-transferase activity [78, 87]. The gene expression in Caco-2 cells was found to be closer to that of cells in the human duodenum after 16 days in culture when compared with Caco-2 cells cultured for only 4 days [88].

Lennernäs et al. compared drug transport rates in Caco-2 monolayers with those obtained in the human jejunum *in vivo* [89]. Caco-2 cells were found to be an excellent model for the passive, trancellular pathway. The permeability of rapidly and completely absorbed compounds transported by the transcellular route in Caco-2 cells differed only 2 to 4-fold from *in vivo* results. The permeability of slowly or incompletely absorbed drugs in Caco-2 monolayers agreed with the permeability *in vivo* qualitatively, but not quantitatively; the permeability values found with Caco-2 cells were 30 to 80-fold lower than those in the human jejunum *in vivo*. This discrepancy is most likely related to the larger amount of absorptive surface area *in vivo* and possibly because the human jejunum has a leakier paracellular pathway. The transepithelial resistance in the human jejunum is approximately 25-50 Ω/cm^2, while the TER in Caco-2 monolayers ranges between 150 and >1400 Ω/cm^2 [24, 90]. The carrier-mediated drug transport rates were also found to be lower in Caco-2 monolayers when compared with the human jejunum because Caco-2 cells express lower levels of most transporters. A study by Sun et al. showed a 2 to 595-fold difference in the expression of transporters, channels, and metabolizing enzymes between the human duodenum and Caco-2 cells [88].

One approach used to increase paracellular permeability and make the *in vitro* model more physiologically realistic was the co-culture of Caco-2 and mucus secreting, goblet-like cell lines. The paracellular permeability of HT29-H mucus secreting cell monolayers was found to be 50-fold higher than the permeability of Caco-2 monolayers, and the mucus layer formed by HT29-H cells was shown to be a

barrier to lipophilic drug absorption [91]. Co-cultures of Caco-2 and HT29-H mucus secreting cells were first characterized by Wilkman-Larhead and Artursson for *in vitro* drug and peptide absorption studies [92]. For co-cultures with ~50% HT29-H cells, the TER decreased by 1.5 fold and the mannitol permeability increased by 2.6 fold. Co-cultures of 50% Caco-2 and 50% HT29-MTX were used by Walter et al. to generate human and rat *in vivo-in vitro* drug permeability correlations; passively diffused, well absorbed drugs were found to correlate best with fractions absorbed in humans [93]. Hilgendorf et al. studied different seeding ratios of Caco-2 and HT29-MTX for *in vitro* drug absorption and intestinal permeability applications [93, 94]. It was shown that varying the ratio of Caco-2 and HT29-MTX cells allows for the modification of monolayer paracellular resistance and secretory transport via P-gp. All of the previously mentioned studies showed that when Caco-2 and goblet-like cells are grown together they form monolayers with tight junctions between the two cell populations. The co-cultures were also found to have a higher permeability to ions, hydrophilic molecules, and peptides than Caco-2 only cultures.

There have been several *in vitro* models developed that mimic first pass metabolism. Choi et al. cultured Caco-2 cells on a permeable Transwell membrane and cultured the HepG2 liver cell line on the bottom of the same well [95]. Benzo[a]pyrene (B[a]P), a chemical that is metabolized by CYP1A1/2 into toxic metabolites, was added to the apical chamber as a model compound. HepG2 and Caco-2 cells were found to actively metabolize B[a]P, and Caco-2 cells were shown to protect the HepG2 cells from B[a]P toxicity by transporting toxic metabolites back to the apical chamber, which agrees with rat *in vivo* data. Lau et al. developed a similar system to predict orally administered drug bioavailability [96]. Caco-2 cells were cultured on permeable Transwell membranes and immediately before experiments primary human hepatocytes were added to the basolateral chamber. Drugs of interest

were added to the apical compartment and samples from the basolateral compartment were analyzed with mass spectrometry. The oral bioavailability predicted from these *in vitro* experiments correlated with human data for 22 of the 24 compounds studied.

Brand et al. developed an *in vitro* diffusion/perifusion system which studied peroxovanadium (a drug with insulin-like properties) transport across Caco-2 cells cultured on a semi-permeable membrane and downstream response by HepG2 liver cells in a separate cell culture compartment [97]. Peroxovanadium was found to passively diffuse across the Caco-2 monolayer, flow downstream to the liver cell compartment, and cause increased glucose consumption by HepG2 cells. This system required two syringe pumps and computer control, ran at a flow rate of 4 mL/hr without recirculation, and only one experiment could be performed at a time. Choi et al. developed a physiologically based, multi-compartment, *in vitro* perfusion system with recirculation that could be used to study intestinal B[a]P absorption and first pass metabolism by the liver [98]. The bioreactor consisted of three compartments which included Caco-2 cells cultured on a semi-permeable membrane with an apical and basolateral chamber, HepG2 liver cells cultured in cellulose-based microcarrier beads, and a third empty compartment that represented the fluid distribution in other tissues. B[a]P was introduced to the system on the apical side of the Caco-2 monolayer, and total of 28 mL of culture medium was re-circulated between the intestinal basolateral, liver, and other tissues compartments. It was found that CYP1A1/2 activity was significantly increased in co-culture systems, but this increase was also seen in static Transwell co-culture systems. The large volume of culture medium used in this system prevents physiologically realistic residence times, *in vivo*-like liquid:cell ratios, and requires a large amount of the compound being studied.

1.7. Physiologically based pharmacokinetic models and cell culture analogs

A physiologically based pharmacokinetic (PBPK) mathematical model describes an organism as a set of interconnected compartments based on vasculature structure, and is designed to describe the time-dependent distribution of a chemical or drug in various tissues [85]. This type of model is based on known physiological parameters such as blood flow rates, tissue volumes, and chemical characteristics such as partition coefficients and metabolic rates [85]. A PBPK model can be useful for cross-species extrapolation and as a human surrogate for estimating risks associated with chemical or drug exposure [99].

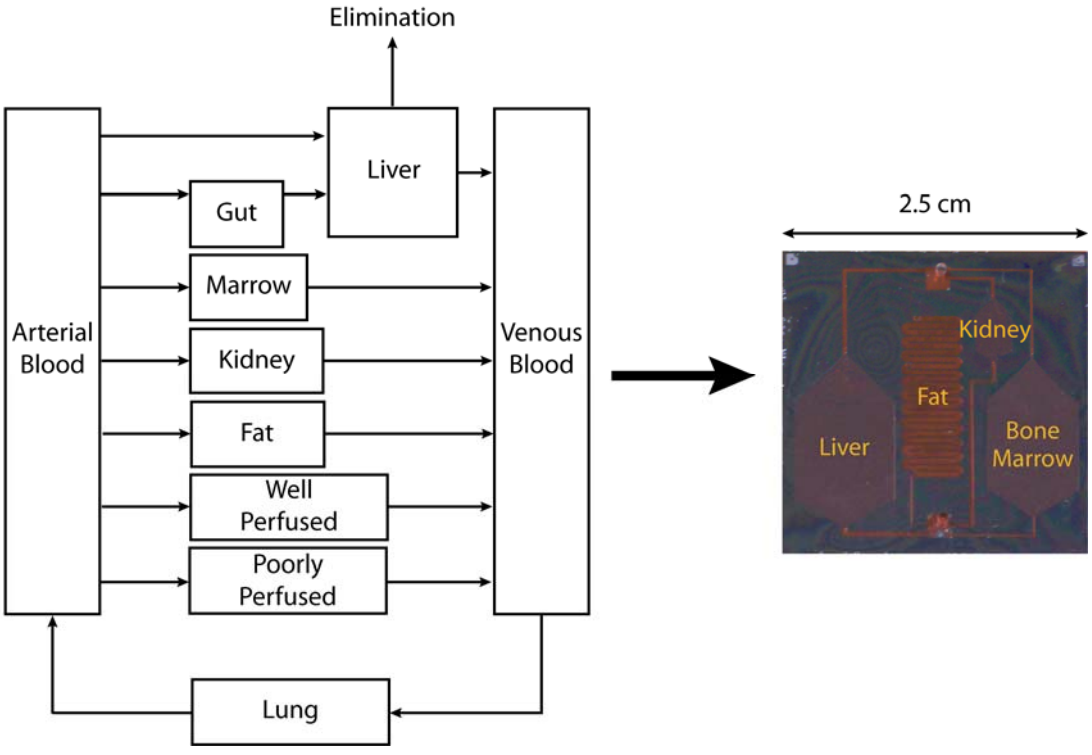

Figure 1.6. A schematic of a physiologically based pharmacokinetic (PBPK) model and a photograph of silicon, chip microscale cell culture analog (μCCA). A PBPK model includes tissues of interest (e.g. the liver) explicitly, but other tissues known to have minimal interaction with the compound being studied can be combined into either well perfused tissues (e.g. the lungs) or slowly perfused tissues (e.g. the muscle) to help maintain an accurate description of chemical dilution in the body. A μCCA is a physical replica of a PBPK model.

A cell culture analog (CCA) is a physical representation of a PBPK model (Figure 1.6). The CCA devices consist of channels and chambers arranged and sized to mimic the residence time and flow distribution of the corresponding PBPK model. Where the PBPK model mathematically specifies an organ or tissue compartment the CCA has an actual chamber holding a cell type that mimics the organ or tissue, while recirculating culture medium represents the circulatory system. The goal of a CCA is to create an *in vitro* system that can replicate some of the cell-cell interactions (i.e. interactions through soluble proteins and metabolites) in humans or animals not easily studied *in vivo* or *in silico* and to apply these observations to toxicology studies. Results obtained with CCA devices can also help to refine the corresponding PBPK models.

A three chamber (lung, liver, and other tissues) microscale cell culture analog (μCCA) was developed using tools from the semiconductor industry [100]. The μCCA was a 2.5 cm x 2.5 cm silicon chip etched to contain cell compartments connected by channels. Culture medium was recirculated through the chip using a peristaltic pump. A four chamber (lung, liver, fat, and other tissues) proof of concept μCCA was used to demonstrate the effects of naphthalene exposure and metabolism on various tissues [101]. Two chambers (lung and liver) contained living cells; the other tissue and fat compartments had no cells, but mimicked the distribution of fluid in rapidly and slowly perfused tissues. Naphthalene added directly to the circulating culture medium was converted to reactive metabolites by CYP1A1/2 in the liver compartment. When these metabolites circulated to the lung compartment the concentration of glutathione, a protective compound, was reduced in the lung cells, resulting in lung cell death. In control experiments without liver cells, however, there was no lung cell death. Later experiments using adipocyte-like cells in the fat chamber showed how fat could modify the response [102]. These experiments show that the system can recreate the

known effects of a toxic chemical. The microscale size of the device allows for near *in vivo* organ residence times, fluid to tissue ratios, and cellular shear stress values. The small size decreases manufacturing costs, reagent amounts, and space needed; and multiple μCCAs can be run simultaneously.

1.8. Summary

This thesis will describe the development of *in vitro* models of the GI tract for studying iron bioavailability, nanoparticle toxicity, and the absorption, distribution, metabolism, elimination, and toxicity (ADMET) of orally administered pharmaceuticals. Chapter 2 will describe the incorporation of mucus producing, goblet-like cells into an existing *in vitro* digestion/cell culture model used for predicting iron bioavailability from food. Mucus has increasingly been shown to affect iron bioavailability *in vivo*, and including mucus in this *in vitro* model may help to make better iron bioavailability predictions. Chapter 3 will discuss the use of static co-cultures of Caco-2 and HT29-MTX and tri-cultures of Caco-2, HT29-MTX, and Raji to determine the effects of nanoparticle exposure on iron absorption. Iron is an essential nutrient transported across the intestinal epithelium by complex mechanisms, and little work has been done to characterize the more subtle effects of chronic exposure to nanoparticles. The development of a GI tract μCCA using acetaminophen as a model drug is discussed in Chapter 4. Previous work with chip μCCAs has been useful for characterizing the ADMET of intravenously administered compounds, but the addition of an independent GI tract μCCA, which includes digestion and a mucus layer, offers an improved *in vitro* method for studying oral drug administration. Chapter 5 will summarize the conclusions made from this work and recommendations for future work with this system.

REFERENCES

1. Furness JB, Kunze WAA, Clerc N. 1999. Nutrient tasting and signaling mechanisms in the gut II. The intestine as a sensory organ: Neural, endocrine, and immune responses. *American Journal of Physiology-Gastrointestinal and Liver Physiology*. 277(5):G922-G928.

2. Martini FH. 2004. Fundamentals of anatomy and physiology. 6th ed. Upper Saddle River, NJ: Prentice Hall, Inc.

3. Tortora GJ, Grabowski SR. 2000. Principles of anatomy and physiology. 9th ed. New York, NY: John Wiley and Sons.

4. DeSesso JM, Jacobson CF. 2001. Anatomical and physiological parameters affecting gastrointestinal absorption in humans and rats. *Food and Chemical Toxicology*. 39(3):209-228.

5. Granger DN, Barrowman JA, Kvietys PR. 1985. Clinical gastrointestinal physiology. Philadelphia, PA: W.B. Saunders Company.

6. Madara JL, Trier JS. 1987. Functional morphology of the mucosa of the small intestine. Johnson R, editor. Physiology of the gastrointestinal tract, 2nd ed. New York, NY: Raven Press.

7. Kararli TT. 1995. Comparison of the gastrointestinal anatomy, physiology, and biochemistry of humans and commonly used laboratory animals. *Biopharmaceutics and Drug Disposition*. 16:351-380.

8. Artursson P, Palm K, Luthman K. 2001. Caco-2 monolayers in experimental and theoretical predictions of drug transport. *Advanced Drug Delivery Reviews*. 46:27-43.

9. Forstner JF, Forstner GG. 1994. Gastrointestinal mucus. Johnson LR, editor. Physiology of the gastrointestinal tract. 3rd ed. New York: Raven Press.

10. Montagne L, Piel C, Lalles JP. 2004. Effect of diet on mucin kinetics and composition: Nutrition and health implications. *Nutrition Reviews*. 62(3):105-114.

11. Sernka TJ, Jacobson ED. 1983. Gastrointestinal physiology - the essentials. 2nd ed. Baltimore: Williams & Wilkins.

12. Owen RL. 1999. Uptake and transport of intestinal macromolecules and microorganisms by M cells in Peyer's patches - a personal and historical perspective. *Seminars in Immunology*. 11:157-163.

13. Castro GA, Arntzen CJ. 1993. Immunophysiology of the gut - a research frontier for integrative studies of the common mucosal immune-system. *American Journal of Physiology*. 265(4):G599-G610.

14. Glahn RP, Lee OA, Yeung A, Goldman MI, Miller DD. 1998. Caco-2 cell ferritin formation predicts nonradiolabeled food iron availability in an *in vitro* digestion/Caco-2 cell culture model. *Journal of Nutrition*. 128:1555-1561.

15. Hidalgo IJ, Raub TJ, Borchardt RT. 1989. Characterization of the human-colon carcinoma cell-line (Caco-2) as a model system for intestinal epithelial permeability. *Gastroenterology*. 96(3):736-749.

16. Basson MD, Turowski G, Emenaker NJ. 1996. Regulation of human (Caco-2) intestinal epithelial cell differentiation by extracellular matrix proteins. *Experimental Cell Research*. 225:301-305.

17. Artursson P, Karlsson J. 1991. Correlation between oral drug absorption in humans and apparent drug permeability coefficients in human intestinal epithelial (Caco-2) cells. *Biochemical and Biophysical Research Communications*. 175(3):880-885.

18. Audus KL, Bartel RL, Hidalgo IJ, Borchardt RT. 1990. The use of cultured epithelial cells for drug transport and metabolism studies. *Pharmaceutical Research*. 7(5):435-451.

19. Lesuffleur T, Barbat A, Dussaulx E, Zweibaum A. 1990. Growth adaptation to methotrexate of HT-29 human colon-carcinoma cells is associated with their ability to differentiate into columnar absorptive and mucus-secreting cells. *Cancer Research*. 50(19):6334-6343.

20. Dahiya R, Lesuffleur T, Kwak KS, Byrd JC, Barbat A, Zweibaum A, Kim YS. 1992. Expression and characterization of mucins associated with the resistance to methotrexate of human colonic adenocarcinoma cell line HT29. *Cancer Research*. 52(17):4655-62.

21. Kerneis S, Bogdanova A, Kraehenbuhl J-P, Pringault E. 1997. Conversion by Peyer's patch lymphocytes of human enterocytes into M cells that transport bacteria. *Science*. 277:949-952.

22. Gullberg E, Leonard M, Karlsson J, Hopkins AM, Brayden D, Baird AW, Artursson P. 2000. Expression of specific markers and particle transport in a new human intestinal M-cell model. *Biochemical and Biophysical Research Communications*. 279(3):808-813.

23. des Rieux A, Fievez V, Theate I, Mast J, Preat V, Schneider YJ. 2007. An improved *in vitro* model of human intestinal follicle-associated epithelium to study nanoparticle transport by M cells. *European Journal of Pharmaceutical*

Sciences. 30(5):380-391.

24. Lu S, Gough AW, Bobrowski WF, Stewart BH. 1996. Transport properties are not altered across Caco-2 cells with heightened TEER despite underlying physiological and ultrastructural changes. *Journal of Pharmaceutical Sciences*. 85(3):270-273.

25. Andrews NC, Schmidt PJ. 2007. Iron homeostasis. *Annual Review of Physiology*. 69:69-85.

26. Andrews NC. 1999. Disorders of iron metabolism. *The New England Journal of Medicine*. 341(26):1986-1995.

27. Cook JD, Monsen ER. 1976. Food iron-absorption in human subjects. 3. Comparison of effect of animal proteins on nonheme iron-absorption. *American Journal of Clinical Nutrition*. 29(8):859-867.

28. Sayers MH, Lynch SR, Jacobs P, Charlton RW, Bothwell TH, Walker RB, Mayet F. 1973. Effects of ascorbic-acid supplementation on absorption of iron in maize, wheat and soya. *British Journal of Haematology*. 24(2):209-218.

29. Kapsokefalou M, Miller DD. 1991. Effects of meat and selected food components on the valence of nonheme iron during *in vitro* digestion. *Journal of Food Science*. 56(2):352.

30. Gillooly M, Bothwell TH, Torrance JD, Macphail AP, Derman DP, Bezwoda WR, Mills W, Charlton RW, Mayet F. 1983. The effects of organic-acids, phytates and polyphenols on the absorption of iron from vegetables. *British Journal of Nutrition*. 49(3):331-342.

31. Hallberg L, Brune M, Erlandsson M, Sandberg AS, Rossanderhulten L. 1991. Calcium - effect of different amounts on nonheme-iron and heme-iron absorption in humans. *American Journal of Clinical Nutrition*. 53(1):112-119.

32. Muir A, Hopfer U. 1985. Regional specificity of iron uptake by small intestinal brush-border membranes from normal and iron-deficient mice. *American Journal of Physiology*. 248(3):G376-G379.

33. Shayeghi M, Latunde-Dada GO, Oakhill JS, Laftah AH, Takeuchi K, Halliday N, Khan Y, Warley A, McCann FE, Hider RC and others. 2005. Identification of an intestinal heme transporter. *Cell*. 122(5):789-801.

34. McKie AT, Barrow D, Latunde-Dada GO, Rolfs A, Sager G, Mudaly E, Mudaly M, Richardson C, Barlow D, Bomford A and others. 2001. An iron-regulated ferric reductase associated with the absorption of dietary iron. *Science*. 291(5509):1755-1759.

35. Gunshin H, Mackenzie B, Berger UV, Gunshin Y, Romero MF, Boron WF, Nussberger S, Gollan JL, Hediger MA. 1997. Cloning and characterization of a mammalian proton-coupled metal-ion transporter. *Nature*. 388(6641):482-488.

36. Conrad ME, Umbreit JN, Moore EG, Hainsworth LN, Porubcin M, Simovich MJ, Nakada MT, Dolan K, Garrick MD. 2000. Separate pathways for cellular uptake of ferric and ferrous iron. *American Journal of Physiology-Gastrointestinal and Liver Physiology*. 279(4):G767-G774.

37. Umbreit JN, Conrad ME, Hainsworth LN, Simovich M. 2002. The ferrireductase paraferritin contains divalent metal transporter as well as mobilferrin. *American Journal of Physiology-Gastrointestinal and Liver Physiology*. 282(3):G534-G539.

38. McKie AT, Marciani P, Rolfs A, Brennan K, Wehr K, Barrow D, Miret S, Bomford A, Peters TJ, Farzaneh F and others. 2000. A novel duodenal iron-regulated transporter, IREG1, implicated in the basolateral transfer of iron to the circulation. *Molecular Cell*. 5(2):299-309.

39. Vulpe CD, Kuo YM, Murphy TL, Cowley L, Askwith C, Libina N, Gitschier J, Anderson GJ. 1999. Hephaestin, a ceruloplasmin homologue implicated in intestinal iron transport, is defective in the sla mouse. *Nature Genetics*. 21(2):195-199.

40. Cherukuri S, Potla R, Sarkar J, Nurko S, Harris ZL, Fox PL. 2005. Unexpected role of ceruloplasmin in intestinal iron absorption. *Cell Metabolism*. 2(5):309-319.

41. Alvarez-Hernandez X, Smith M, Glass J. 1994. Regulation of iron uptake and transport by transferrin in Caco-2 cells, an intestinal-cell line. *Biochimica et Biophysica Acta-Biomembranes*. 1192(2):215-222.

42. Alvarez-Hernandez X, Smith M, Glass J. 1998. The effect of apotransferrin on iron release from Caco-2 cells, an intestinal epithelial cell line. *Blood*. 91(10):3974-3979.

43. Nunez MT, Tapia V. 1999. Transferrin stimulates iron absorption, exocytosis, and secretion in cultured intestinal cells. *American Journal of Physiology-Cell Physiology*. 276(5):C1085-C1090.

44. Ma YX, Specian RD, Yeh KY, Yeh M, Rodriguez-Paris J, Glass J. 2002. The transcytosis of divalent metal transporter 1 and apo-transferrin during iron uptake in intestinal epithelium. *American Journal of Physiology-Gastrointestinal and Liver Physiology*. 283(4):G965-G974.

45. Linder MC, Mortya M, Whon A, Kassa A, Gilley C. 2006. Vesicular transport of Fe and interaction with other metal ions in polarized Caco2 cell monolayers.

Biological Research. 39(1):143-156.

46. Moriya M, Linder MC. 2006. Vesicular transport and apotransferrin in intestinal iron absorption, as shown in the Caco-2 cell model. *American Journal of Physiology-Gastrointestinal and Liver Physiology*. 290(2):G301-G309.

47. Powell JJ, Jugdaohsingh R, Thompson RPH. 1999. The regulation of mineral absorption in the gastrointestinal tract. *Proceedings of the Nutrition Society*. 58(1):147-153.

48. Conrad ME, Umbreit JN, Moore EG. 1993. Regulation of iron-absorption - proteins involved in duodenal mucosal uptake and transport. *Journal of the American College of Nutrition*. 12(6):720-728.

49. Conrad ME, Umbreit JN, Moore EG. 1994. Iron absorption and cellular uptake of iron. *Advances in Experimental Medicine and Biology*. 356:69-79.

50. Simovich M, Hainsworth LN, Fields PA, Umbreit JN, Conrad ME. 2003. Localization of the iron transport proteins mobilferrin and DMT-1 in the duodenum: The surprising role of mucin. *American Journal of Hematology*. 74(1):32-45.

51. Halleux C, Schneider YJ. 1991. Iron absorption by intestinal epithelial cells: 1. Caco-2 cells cultivated in serum-free medium, on polyethyleneterephthalate micropourous membranes, as an *in vitro* model. *In Vitro Cell Developmental Biology*. 27A:293-302.

52. Alvarez-Hernandez X, Nichols GM, Glass J. 1991. Caco-2 cell line: A system for studying intestinal iron transport across epithelial cell monolayers. *Biochemica et Biophysica Acta*. 1070:205-208.

53. Han OH, Wessling-Resnick M. 2002. Copper repletion enhances apical iron uptake and transepithelial iron transport by Caco-2 cells. *American Journal of Physiology-Gastrointestinal and Liver Physiology*. 282(3):G527-G533.

54. Glahn RP, Wien EM, VanCampen DR, Miller DD. 1996. Caco-2 cell iron uptake from meat and casein digests parallels *in vivo* studies: Use of a novel *in vitro* method for rapid estimation of iron bioavailability. *Journal of Nutrition*. 126(1):332-339.

55. Glahn RP, Lai C, Hsu J, Thompson JF, Guo MR, Van Campen DR. 1998. Decreased citrate improves iron availability from infant formula: Application of an *in vitro* digestion Caco-2 cell culture model. *Journal of Nutrition*. 128(2):257-264.

56. Florence AT. 1997. The oral absorption of micro- and nanoparticulates: Neither exceptional nor unusual. *Pharmaceutical Research*. 14(3):259-266.

57. Oberdorster G, Oberdorster E, Oberdorster J. 2005. Nanotoxicology: An emerging discipline evolving from studies of ultrafine particles. *Environmental Health Perspective*. 113(7):823-839.

58. Pontefra RD, Cunningham HM. 1973. Penetration of asbestos through digestive tract of rats. *Nature*. 243(5406):352-353.

59. Kreyling WG, Semmler M, Erbe F, Mayer P, Takenaka S, Schulz H, Oberdorster G, Ziesenis A. 2002. Translocation of ultrafine insoluble iridium particles from lung epithelium to extrapulmonary organs is size dependent but very low. *Journal of Toxicology and Environmental Health, Part A: Current Issues*. 65(20):1513-30.

60. Semmler M, Seitz J, Erbe F, Mayer P, Heyder J, Oberdorster G, Kreyling WG. 2004. Long-term clearance kinetics of inhaled ultrafine insoluble iridium particles from the rat lung, including transient translocation into secondary organs. *Inhalation Toxicology*. 16(6-7):453-9.

61. Yamago S, Tokuyama H, Nakamura E, Kikuchi K, Kananishi S, Sueki K, Nakahara H, Enomoto S, Ambe F. 1995. *In vivo* biological behavior of a water-miscible fullerene: ^{14}C labeling, absorption, distribution, excretion and acute toxicity. *Chemistry & Biology*. 2(6):385-389.

62. Jani PU, McCarthy DE, Florence AT. 1994. Titanium-dioxide (rutile) particle uptake from the rat GI tract and translocation to systemic organs after oral-administration. *International Journal of Pharmaceutics*. 105(2):157-168.

63. Jani P, Halbert GW, Langridge J, Florence AT. 1990. Nanoparticle uptake by the rat gastrointestinal mucosa: Quantitation and particle size dependency. *Journal of Pharmacy and Pharmacology*. 42(12):821-826.

64. Jani P, Halbert GW, Langridge J, Florence AT. 1989. The uptake and translocation of latex nanospheres and microspheres after oral-administration to rats. *Journal of Pharmacy and Pharmacology*. 41(12):809.

65. El-Shabouri MH. 2002. Positively charged nanoparticles for improving the oral bioavailability of cyclosporin-A. *International Journal of Pharmaceutics*. 249(1-2):101-108.

66. Lomer MCE, Thompson RPH, Powell JJ. 2002. Fine and ultrafine particles of the diet: Influence on the mucosal immune response and association with Crohn's disease. *Proceedings of the Nutrition Society*. 61(1):123-130.

67. Powell JJ, Harvey RSJ, Ashwood P, Wolstencroft R, Gershwin ME, Thompson RPH. 2000. Immune potentiation of ultrafine dietary particles in normal subjects and patients with inflammatory bowel disease. *Journal of Autoimmunity*. 14(1):99-105.

68. Shepherd NA, Crocker PR, Smith AP, Levison DA. 1987. Exogenous pigment in Peyers-patches. *Human Pathology*. 18(1):50-54.

69. Powell JJ, Ainley CC, Harvey RSJ, Mason IM, Kendall MD, Sankey EA, Dhillon AP, Thompson RPH. 1996. Characterization of inorganic microparticles in pigment cells of human gut associated lymphoid tissue. *Gut*. 38(3):390-395.

70. Behrens I, Pena AIV, Alonso MJ, Kissel T. 2002. Comparative uptake studies of bioadhesive and non-bioadhesive nanoparticles in human intestinal cell lines and rats: The effect of mucus on particle adsorption and transport. *Pharmaceutical Research*. 19(8):1185-1193.

71. des Rieux A, Ragnarsson EGE, Gullberg E, Preat V, Schneider YJ, Artursson P. 2005. Transport of nanoparticles across an *in vitro* model of the human intestinal follicle associated epithelium. *European Journal of Pharmaceutical Sciences*. 25(4-5):455-465.

72. Chen Z, Meng HA, Xing GM, Chen CY, Zhao YL, Jia GA, Wang TC, Yuan H, Ye C, Zhao F and others. 2006. Acute toxicological effects of copper nanoparticles *in vivo*. *Toxicology Letters*. 163(2):109-120.

73. Gerhart EH, Liukkonen RJ, Carlson RM, Stokes GN, Lukasewycz M, Oyler AR. 1981. Histological effects and bioaccumulation potential of coal particulate-bound phenanthrene in the fathead minnow *pimephales-promelas*. *Environmental Pollution Series A-Ecological and Biological*. 25(3):165-180.

74. Lomer MCE, Hutchinson C, Volkert S, Greenfield SM, Catterall A, Thompson RPH, Powell JJ. 2004. Dietary sources of inorganic microparticles and their intake in healthy subjects and patients with Crohn's disease. *British Journal of Nutrition*. 92(6).

75. Lomer MCE, Grainger SL, Ede R, Catterall AP, Greenfield SM, Cowan RE, Vicary FR, Jenkins AR, Fidler H, Harvey RS and others. 2005. Lack of efficacy of a reduced microparticle diet in a multi-centered trial of patients with active Crohn's disease. *European Journal of Gastroenterology & Hepatology*. 17(3):377-384.

76. Butler M, Boyle J, Powell J, Playford R, Ghosh S. 2007. Dietary microparticles implicated in Crohn’s disease can impair macrophage phagocytic activity and act as adjuvants in the presence of bacterial stimuli. *Inflammation Research*. 56(9):353.

77. Werle M. 2008. Polymeric and low molecular mass efflux pump inhibitors for oral drug delivery. *Journal of Pharmaceutical Sciences*. 97(1):60-70.

78. Prueksaritanont T, Gorham LM, Hochman JH, Tran LO, Vyas KP. 1996. Comparative studies of drug-metabolizing enzymes in dog, monkey, and

human small intestine cells, and in Caco-2 cells. *Drug Metabolism and Disposition*. 24(6):634-642.

79. Rang HP, Dale MM, Ritter JM. 1999. Pharmacology. 4th ed. Edinburgh: Churchill Livingston.

80. Doherty MM, Charman WN. 2002. The mucosa of the small intestine: How clinically relevant as an organ of drug metabolism? *Clinical Pharmacokinetics*. 41(4):235-253.

81. Konig J, Nies AT, Cui YH, Leier I, Keppler D. 1999. Conjugate export pumps of the multidrug resistance protein (MRP) family: Localization, substrate specificity, and MRP2-mediated drug resistance. *Biochimica et Biophysica Acta-Biomembranes*. 1461(2):377-394.

82. Thiebaut F, Tsuruo T, Hamada H, Gottesman MM, Pastan I, Willingham MC. 1987. Cellular localization of the multidrug-resistance gene product p-glycoprotein in normal human tissues. *Proceedings of the National Academy of Sciences of the United States of America*. 84(21):7735-7738.

83. Heyman M, Craindenoyelle AM, Nath SK, Desjeux JF. 1990. Quantification of protein transcytosis in the human colon-carcinoma cell-line Caco-2. *Journal of Cellular Physiology*. 143(2):391-395.

84. Owen RL, Ermak TH. 1990. Structural specializations for antigen uptake and processing in the digestive-tract. *Springer Seminars in Immunopathology*. 12(2-3):139-152.

85. Brown RP, Delp MD, Lindstedt SL, Rhomberg LR, Beliles RP. 1997. Physiological parameter values for physiologically based pharmacokinetic models. *Toxicology and Industrial Health*. 13(4):407-484.

86. Borlak J, Zwadlo C. 2003. Expression of drug-metabolizing enzymes, nuclear transcription factors, and abc transporters in Caco-2 cells. *Xenobiotica*. 33(9):927-943.

87. Baranczykkuzma A, Garren JA, Hidalgo IJ, Borchardt RT. 1991. Substrate-specificity and some properties of phenol sulfotransferase from human intestinal Caco-2 cells. *Life Sciences*. 49(16):1197-1206.

88. Sun DS, Lennernas H, Welage LS, Barnett JL, Landowski CP, Foster D, Fleisher D, Lee K, Amidon GL. 2002. Comparison of human duodenum and Caco-2 gene expression profiles for 12,000 gene sequence tags and correlation with permeability of 26 drugs. *Pharmaceutical Research*. 19(10):1400-1416.

89. Lennernas H, Palm K, Fagerholm U, Artursson P. 1996. Comparison between active and passive drug transport in human intestinal epithelial (Caco-2) cells

in vitro and human jejunum *in vivo*. *International Journal of Pharmaceutics*. 127:103-107.

90. Ekmekcioglu C. 2002. A physiological approach for preparing and conducting intestinal bioavailability studies using experimental systems. *Food Chemistry*. 76(2):225-230.

91. Wikman A, Karlsson J, Carlstedt I, Artursson P. 1993. A drug absorption-model based on the mucus layer producing human intestinal goblet cell-line HT29-H. *Pharmaceutical Research*. 10(6):843-852.

92. Wikman-Larhed A, Artursson P. 1995. Cocultures of human intestinal goblet (HT29-H) and absorptive (Caco-2) cells for studies of drug and peptide absorption. *European Journal of Pharmaceutical Sciences*. 3(3):171-183.

93. Walter E, Janich S, Roessler BJ, Hilfinger JM, Amidon GL. 1996. HT29-MTX/Caco-2 cocultures as an *in vitro* model for the intestinal epithelium: *In vitro in vivo* correlation with permeability data from rats and humans. *Journal of Pharmaceutical Sciences*. 85(10):1070-1076.

94. Hilgendorf C, Spahn-Langguth H, Regardh CG, Lipka E, Amidon GL, Langguth P. 2000. Caco-2 versus Caco-2/HT29-mtx co-cultured cell lines: Permeabilities via diffusion, inside- and outside-directed carrier-mediated transport. *Journal of Pharmaceutical Sciences*. 89(1):63-75.

95. Choi SH, Nishikawa M, Sakoda A, Sakai Y. 2004. Feasibility of a simple double-layered coculture system incorporating metabolic processes of the intestine and liver tissue: Application to the analysis of benzo[a]pyrene toxicity. *Toxicology In Vitro*. 18(3):393-402.

96. Lau YY, Chen YH, Liu TT, Li C, Cui XM, White RE, Cheng KC. 2004. Evaluation of a novel *in vitro* Caco-2 hepatocyte hybrid system for predicting *in vivo* oral bioavailability. *Drug Metabolism and Disposition*. 32(9):937-942.

97. Brand RM, Hannah TL, Mueller C, Cetin Y, Hamel FG. 2000. A novel system to study the impact of epithelial barriers on cellular metabolism. *Annals of Biomedical Engineering*. 28(10):1210-1217.

98. Choi SH, Fukuda O, Sakoda A, Sakai Y. 2004. Enhanced cytochrome p450 capacities of Caco-2 and HepG2 cells in new coculture system under the static and perfused conditions: Evidence for possible organ-to-organ interactions against exogenous stimuli. *Materials Science and Engineering: C*. 24(3):333.

99. Ghanem A, Shuler ML. 2000. Characterization of a perfusion reactor utilizing mammalian cells on microcarrier beads. *Biotechnology Progress*. 16:471-479.

100. Sin A, Chin KC, Jamil MF, Kostov Y, Rao G, Shuler ML. 2004. The design and

fabrication of three-chamber microscale cell culture analog devices with integrated dissolved oxygen sensors. *Biotechnology Progress*. 20:338-345.

101. Viravaidya K, Sin A, Shuler ML. 2004. Development of a microscale cell culture analog to probe naphthalene toxicity. *Biotechnology Progress*. 20(1):316-323.

102. Viravaidya K, Shuler ML. 2004. Incorporation of 3T3-L1 cells to mimic bioaccumulation in a microscale cell culture analog device for toxicity studies. *Biotechnology Progress*. 20(2):590-597.

CHAPTER 2

CHARACTERIZATION OF CACO-2 AND HT29-MTX CO-CULTURES IN AN *IN VITRO* DIGESTION/CELL CULTURE MODEL USED TO PREDICT IRON BIOAVAILABILITY[1]

2.1. Introduction

Iron deficiency is one of the most prevalent nutritional problems in the world [1]. There are many factors that contribute to iron deficiency, but low dietary iron bioavailability is the primary cause [1]. Dietary interventions to help control iron deficiency include consuming a diverse diet that includes meat and green leafy vegetables, supplementation, fortifying staple foods with iron, and biofortification, which is breeding crops that are rich in bioavailable iron [2]. All of these strategies, however, require iron bioavailability validation for numerous factors, compounds, conditions, and potential food interactions. Human studies are lengthy and expensive, and animal response may differ from that of humans [3]. The *in vitro* digestion/Caco-2 cell culture model developed by Glahn et al. offers a rapid, low cost method to screen foods and food combinations for iron bioavailability before more definitive human trials [4].

Iron bioavailability results from the *in vitro* digestion/Caco-2 cell culture model have been well correlated, qualitatively, with human data. The effects of meat and ascorbic acid on iron absorption, both known to enhance iron availability *in vivo*, have been reproduced in this system [4, 5]. Factors that inhibit iron uptake, such as

[1] Portions of this chapter have been published previously.

phytic and tannic acid, have also been replicated [6]. The *in vitro* iron bioavailability of iron supplements (a polysaccharide-iron complex and an $FeSO_4$ preparation) agreed with results from a closely matched human study [7, 8].

Results from quantitative studies comparing *in vivo* human to *in vitro* Caco-2 iron uptake results for semisynthetic meals have shown that human and Caco-2 data generally agree [9-11]. Yun et al. determined that the Caco-2 model can be used to estimate human iron bioavailability from complex meals if the results can be compared as absorption ratios, which are the iron absorption at a given level of promoter or inhibitor divided by the iron absorption without the promoter or inhibitor present [10]. This was the first study to provide an actual conversion factor for transforming Caco-2 cell observations into a prediction for human iron absorption. A study performed by Beiseigel et al. confirmed that absorption ratios from Caco-2 cell data accurately predicted human iron absorption from maize meals extrinsically isotope labeled for nonheme iron, but not for extrinsically labeled great northern and pinto bean meals [11]. Recent work by Jin et al., however, has shown that there is poor equilibration between extrinsic and intrinsic iron in the bean samples, which questions the reliability of extrinsic isotope labeling of plant foods for iron absorption studies [12]. Although human and Caco-2 iron absorption data generally agree and the current Caco-2 to human conversion factor is relatively simple and easy to apply, one missing factor in the Caco-2 model that may alter the conversion factor and improve the correlation between *in vitro* and human data is the presence of a mucus layer.

The mucus layer covering the intestinal epithelium is thought to play a role in iron absorption. Mucus, which is largely composed of heavily glycosylated proteins (mucins), is secreted by goblet cells in the intestinal epithelium. [13]. Some ingested metals remain soluble throughout the 1-8 pH range of the GI tract (Na, Mg, and Ca), but others (Al, Cu, Fe, Mn, and Zn) are susceptible to hydroxy-polymerization, which

is the formation of insoluble metal hydroxides that cannot be absorbed [14]. Hydroxy-polymerization occurs when, in the absence of soluble ligands, acid soluble Al, Cu, Fe, and Zn form hydroxide precipitates as the intestinal lumen pH increases. Work by Conrad et al. has shown that mucins bind iron at an acidic pH when iron is soluble and these mucin-iron complexes prevent iron precipitation as the pH in the small intestine increases to near neutral values [15]. These findings, along with the ability of mucin to accept iron from ascorbate, fructose, and histidine chelates at neutral pH, suggest that mucin presents iron to the intestinal mucosa in an acceptable form for absorption [16]. More recently two main iron transport proteins, divalent metal transporter-1 (DMT-1) and mobilferrin, were found to be concentrated in mucin vesicles near the luminal surface, strengthening the role of mucin in iron uptake [17].

Goblet cells can be mimicked *in vitro* using mucus secreting cell lines such as HT29-MTX. HT29-MTX are a subpopulation of HT29 human colonic adenocarcinoma cells selected for resistance to methotrexate (MTX) [18]. After a slow adaptation to MTX, the HT29-MTX cell population consists exclusively of differentiated, gastric-like mucus secreting, goblet-type cells that retain their differentiated phenotype after reversion to MTX-free medium [19]. Co-cultures of Caco-2 and HT29-MTX represent the two major cell types (absorptive and goblet) found in the small intestinal epithelium. Wilkman-Larhead and Artursson first characterized co-cultures of Caco-2 and goblet-like HT29-H cells for *in vitro* drug and peptide absorption studies [20]. Walter et al. used Caco-2 and HT29-MTX co-cultures to generate human and rat *in vivo-in vitro* drug permeability correlations, and Hilgendorf et al. studied different seeding ratios of Caco-2 and HT29-MTX for *in vitro* drug absorption and intestinal permeability applications [21, 22]. All of these studies showed that when Caco-2 and goblet-like cells are grown together they form monolayers with tight junctions between the two cell populations. This work is the

first to use co-cultures of Caco-2 and HT29-MTX for iron bioavailability studies.

The goal of this study was to incorporate HT29-MTX mucus producing cells into an *in vitro* digestion/cell culture model used to predict iron bioavailability. Ferric chloride ($FeCl_3$), ferric chloride plus ascorbic acid ($FeCl_3$ + AA), horse spleen ferritin (HSF), horse spleen ferritin plus ascorbic acid (HSF + AA), white bean, red bean, soybean, cooked beef, and cooked fish plus ferric chloride (fish + Fe) were subjected to *in vitro* digestion and placed into 15,000 molecular weight cut-off (MWCO) dialysis membrane inserts or 74 μm mesh Netwell® inserts above Caco-2 cells, Caco-2 cells overlaid with porcine mucin (Caco-2 + mucin), HT29-MTX cells, or co-cultures Caco-2 and HT29-MTX cells at varying ratios. Iron bioavailability from the digests was evaluated by cell ferritin formation.

2.2. Materials and Methods

2.2.1. Chemicals, enzymes, and hormones

All chemicals, enzymes, and hormones were purchased from Sigma Chemical Company (St. Louis, MO) unless otherwise stated. All glassware used in sample preparation and analysis was washed, soaked in 10% hydrochloric acid (HCl) and 10% nitric acid overnight, and rinsed with 18 MΩ water to avoid iron contamination.

2.2.2. Cell culture

The human colon carcinoma Caco-2 cell line was obtained from the American Type Culture Collection (Manassas, VA) at passage 17 and used in experiments at passage 30-35. The HT29-MTX cell line was kindly provided by Dr. Thécla Lesuffleur of INSERM U560 in Lille, France at passage 11 and used in experiments at passage 14-19. Caco-2 cells were grown in Dulbecco's Modified Eagle Medium (DMEM, Invitrogen, Grand Island, NY) containing 4.5 g/L glucose, 25 mM HEPES

buffer, and 10% fetal bovine serum (Invitrogen). HT29-MTX and Caco-2 co-cultured with HT29-MTX were grown in DMEM containing 4 mM Glutamax, 4.5 g/L glucose, and 10% heat inactivated fetal bovine serum (Co-culture medium, Invitrogen). The cells were maintained at 37°C in 5% CO_2 and culture medium was changed every 2 days. For experimental studies Caco-2 and HT29-MTX were stained with trypan blue, counted with a hemocytometer, and re-suspended at ratios of 100:0 (Caco-2:HT29-MTX), 90:10, 75:25, 50:50, 25:75, and 0:100. Caco-2, Caco-2 and HT29-MTX, or HT29-MTX were seeded at a density of 50,000 cells/cm^2 onto 6 well plates (Corning Life Sciences, Acton, MA) coated with rat tail Type I collagen (BD Biosciences, San Jose, CA) at 8 μg/cm^2. Experiments were performed 16 days post seeding. On the day before the *in vitro* digestion experiment, DMEM was removed and the monolayers were washed with and cultured overnight in very low iron (<8 μg/L) minimal essential medium (MEM, Invitrogen) supplemented with 10 mM PIPES (piperazine-*N*,*N*'-bis-[2-ethanesulfonic acid]), 4 mg/L hydrocortisone, 5 mg/L insulin, 5 μg/L selenium, 34 μg/L triiodothyronine, 1% antibiotic-antimycotic solution, and 20 μg/L epidermal growth factor at pH 7.0 [4]. Under these conditions, baseline cell ferritin levels were approximately 3 ng ferritin/mg cell protein.

2.2.3. Mucus layer characterization

A method developed by Kerss et al. and Sandzen et al. and modified by Wikman et al. was used to determine mucus layer coverage [23-25]. HT29-MTX and co-cultures of Caco-2 and HT29-MTX were seeded onto polycarbonate, 0.4 μm pore size, Type I collagen coated, 24 mm Transwell® inserts (Corning Life Sciences) at a density of 50,000 cells/cm^2. After 16 days, strips of the monolayer on the polycarbonate membrane were cut using a tool made from two razor blades glued onto each side of a microscope slide. The strips were stained for 1 minute in 0.25%

toluidine blue in PBS and held transversely in co-culture medium with silicone holders placed on a microscope slide. The weakly stained mucus layer was discernable from the more darkly stained cell monolayer.

Periodic acid Schiff (PAS, stains hexose and sialic acid-containing mucosubstances pink) staining was used to visualize the mucus layer thickness. HT29-MTX and co-cultures of Caco-2 and HT29-MTX were seeded onto polycarbonate, 0.4 μm pore size, Type I collagen coated, 24 mm Transwell inserts at a density of 50,000 cells/cm^2. After 16 days, the cells were washed with Dulbecco's Phosphate Buffered Saline (DPBS, Invitrogen), fixed with 6% formaldehyde in 0.27 M $CaCl_2$, pH 4.0 at 4^oC for 1 hour, and washed again with DPBS. HistoGel^{TM} (Richard-Allan Scientific, Kalamazoo, MI) was liquefied by heating to 60^oC and approximately 1 mL was added to the apical and basolateral sides of the polycarbonate membrane. After the HistoGel cooled and solidified, the membranes were removed with a razor blade and embedded in paraffin. Thin sections were cut transversely and stained with PAS.

Co-cultures of Caco-2 and HT29-MTX at varying ratios were seeded onto 6-well plates for histochemical evaluation of HT29-MTX cell location. After 16 days in culture, cells were washed with DPBS, fixed with 6% formaldehyde in 0.27 M $CaCl_2$, pH 4.0 at 4^oC for 1 hour, and washed again with DPBS. Cells were stained with alcian blue (pH 2.5) to visualize acid mucosubstances firmly attached to HT29-MTX cells.

2.2.4. Sample preparation

All samples were prepared in 50 mL conical centrifuge tubes and adjusted to contain a final concentration of 50 μM Fe ($FeCl_3$, $FeCl_3$ + AA, HSF, HSF + AA, and fish + Fe) with a 1:20 molar ratio of Fe:AA for the + AA samples, 1.0 g of food (white bean, red bean, and soybean), and/or 0.5 g of food (beef and fish + Fe) in 15 mL of digest. All samples containing $FeCl_3$ were prepared by adding 42 μL of a 1000 μg

Fe/mL in 2% HCl stock solution (High Purity Standards, Charleston, SC) to each 50 mL tube. A 100 μL aliquot of a freshly prepared 100 mM AA solution (~1:20 Fe:AA molar ratio) was added to the $FeCl_3$ + AA samples and allowed to react for 15 minutes at room temperature before further manipulations were made. $FeCl_3$ stock solution was added to 0.5 g fish to make the fish + Fe samples. A 2 μL aliquot of HSF stock solution (91 mg ferritin/mL) was used for each HSF and HSF + AA sample; 100 uL of 100 mM AA solution was added to the HSF + AA samples and allowed to react for 15 minutes before further manipulation. All food samples were obtained from a local grocery store. White bean (Goya Great Northern Beans, 70.71 μg Fe/g), red bean (Goya Red Kidney Beans, 53.59 μg Fe/g), beef (81.17 μg Fe/g), and fish (haddock, 0.12 μg Fe/g) food samples were cooked, autoclaved, lyophilized, ground, and stored at -20^{o}C until use. Soybeans (Arrowhead Mills Soybeans, 64.01 μg Fe/g) were ground and used in experiments uncooked.

2.2.5. Mucin preparation

Mucin preparation and characterization was previously described in detail [26]. Porcine stomach mucin was prepared at a concentration of 25 mg/mL in 140 mM NaCl, 5 mM KCl, pH 2.0; mixed with chelating resin to remove iron (Chelex-100, Bio-Rad Laboratories, Hercules, CA); poured through a glass column (ID = 1.5 cm, length = 45 cm) to remove the resin; and stored at -20^{o}C. The iron concentration in the resin-treated mucin was 1.4 mg/L. On the day of the *in vitro* digestion experiment the mucin was thawed and added to MEM for a final concentration of 5 mg/mL mucin. A 1 mL aliquot of the MEM + mucin solution was added to designated monolayers immediately before the intestinal digestion.

2.2.6. In vitro digestion/cell culture technique

A detailed *in vitro* digestion method has been described elsewhere [4]. Briefly,

the gastric digestion phase was initiated by adding 10 mL of 140 mM NaCl, 5 mL KCl, pH 2 solution to each sample and re-adjusting each sample to pH 2 with 1 M HCl. An aliquot of 0.5 mL very low iron porcine pepsin solution (25 mg/mL, 800-2500 units/mg protein) in 0.1 M HCl was added to each tube and the samples were rocked at 55 oscillations/min on a rocking platform (Laboratory Instrument Model RP-50, Rockville, MD) for 1 hour at 37°C. After the 1 hour gastric incubation, the pH of the samples was raised to 5.5-6.0 with 1 M $NaHCO_3$ and 2.5 mL of very low iron porcine pancreatin/bile solution (2 mg/mL pancreatin, activity 4 × USP specifications; 11 mg/mL bile, glycine and taurine conjugates of hyodeoxycholic and other bile salts) was added. The pH was then adjusted to 7.0 with 1 M $NaHCO_3$ and the volume of each tube brought to 15 mL by weight with 140 mM NaCl, 5 mM KCl, pH 6.7. After this point, the samples were referred to as digests.

Immediately before the intestinal digestion period, the MEM was removed from each culture well and replaced with a fresh 1.0 mL aliquot of MEM (or MEM containing 5 mg/mL mucin for Caco-2 + mucin treatments). Transwell insert rings fitted with 15,000 MWCO dialysis membrane and sterilized with 0.5 M HCl were also inserted into each well, creating a two-chamber system. The intestinal digestion period was initiated by adding a 1.5 mL aliquot of digest into the modified Transwell insert. The plates were then incubated at 37°C on a rocking shaker at 6 oscillations/min for 2 hours. The intestinal digestion was terminated by removing the insert ring and digest. The solution in the bottom chamber was allowed to remain on the cell monolayers and an additional 1 mL of MEM was added to each well. The cell culture plate was returned to the incubator and the cells were harvested after an additional 22 hours. Cells were harvested by removing the MEM; washing the monolayers twice with 2 mL 130 mM NaCl, 5 mM, and 5 mM PIPES, pH 7.0; adding 2 mL of 18 MΩ water to each well; and sonicating the cells (Elma Transsonic Digital sonicator, Lab-Line

Instruments) for 15 minutes at 4°C. After sonication the cell solutions were aspirated and stored at –20°C.

2.2.7. Removal of mucus layer

To study the effects of the mucus layer on iron absorption in HT29-MTX cells, the mucus layer was removed using a protocol described by Behrens et al. [27]. Immediately before the intestinal digestion, MEM was removed from HT29-MTX cells cultured for 16 days and replaced with 2.0 mL of 10 mM N-acetylcysteine in DPBS. The plates were then incubated at 37°C under agitation (135 rpm, Labnet International, Edison, NJ) for 1 hour. Subsequently, the cells were washed twice with DPBS and 1.0 mL of MEM was added to each well. Mucus removal was verified by alcian blue staining after the washing procedure.

2.2.8. Assays

Cell protein was measured using a Bio-Rad DC protein assay kit, which is a commercial semimicro adaptation of the Lowry assay (Bio-Rad Laboratories), on samples that had been solubilized in 0.5 M NaOH. A one stage, two site immunoradiometric assay was used to measure cell ferritin content (FER-IRON II Serum Ferritin Assay, RAMCO Laboratories, Stafford, TX). A 10 μL sample of the cell solutions was used for each ferritin measurement and gamma radiation was counted in an automatic gamma counter (Packard Auto-Gamma Model 5530, PerkinElmer Life and Analytical Sciences, Wellesley, MA). The iron content of the food samples and porcine mucin was evaluated using an inductively coupled argon plasma emission spectrometer (ICAP Model 61E Trace Analyzer, Thermo Jarrell Ash Corporation, Franklin, MA).

2.2.9. Statistical analysis

Results are expressed as mean ± standard error. Data was analyzed with the GraphPad Prism version 4.00 for Windows (GraphPad Software, San Diego, CA). A one-way ANOVA with Tukey's post test was used to compare differences between means and data was transformed when necessary to obtain equal sample variances. Differences between means were considered significant at $p < 0.05$.

2.3. Results

2.3.1. Mucus layer visualization and characterization

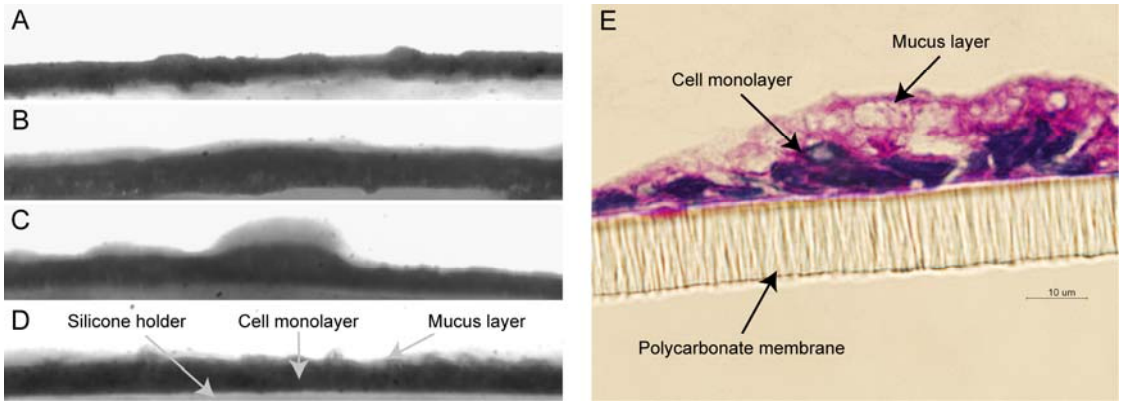

Figure 2.1. (A) Caco-2, (B) 90:10, (C) 75:25, and (D) HT29-MTX viable cells after 16 days in culture, ratios are Caco-2:HT29-MTX. Toluidine blue stained the cell monolayer dark and weakly stained the mucus layer. These images show that the mucus layer completely covered the cell monolayer, even in co-cultures with low ratios of HT29-MTX cells. (E) Co-culture of 90% Caco-2 and 10% HT29-MTX grown for 16 days on a Transwell insert and stained with periodic acid Schiff (PAS, stains acidic mucosubstances pink). This figure shows that the mucus layer thickness was irregular, but at the lowest ratio of HT29-MTX cells used (90:10 Caco-2:HT29-MTX) the mucus was approximately 2-10 μm thick. Similar results were found for other Caco-2:HT29-MTX seeding ratios. Scale bar = 10 μm.

HT29-MTX and co-cultures of Caco-2 and HT29-MTX cells grown for 16 days on a permeable membrane developed a mucus layer that completely covered the monolayer and was approximately 2-10 μm thick (Figure 2.1). The porcine gastric

mucin did not form a visible coating. The mucus layer over HT29-MTX cells was more firmly attached than the layer over Caco-2 cells and could withstand the multiple washing steps involved in histochemical preparation. Figure 2.2 shows that at lower HT29-MTX ratios there are clusters of HT29-MTX cells surrounded by Caco-2 cells and at higher HT29-MTX ratios there are clusters of Caco-2 cells surrounded by HT29-MTX cells, but that, overall, the number of HT29-MTX cells in the 16 day-old cultures increased with increasing initial HT29-MTX seeding ratios.

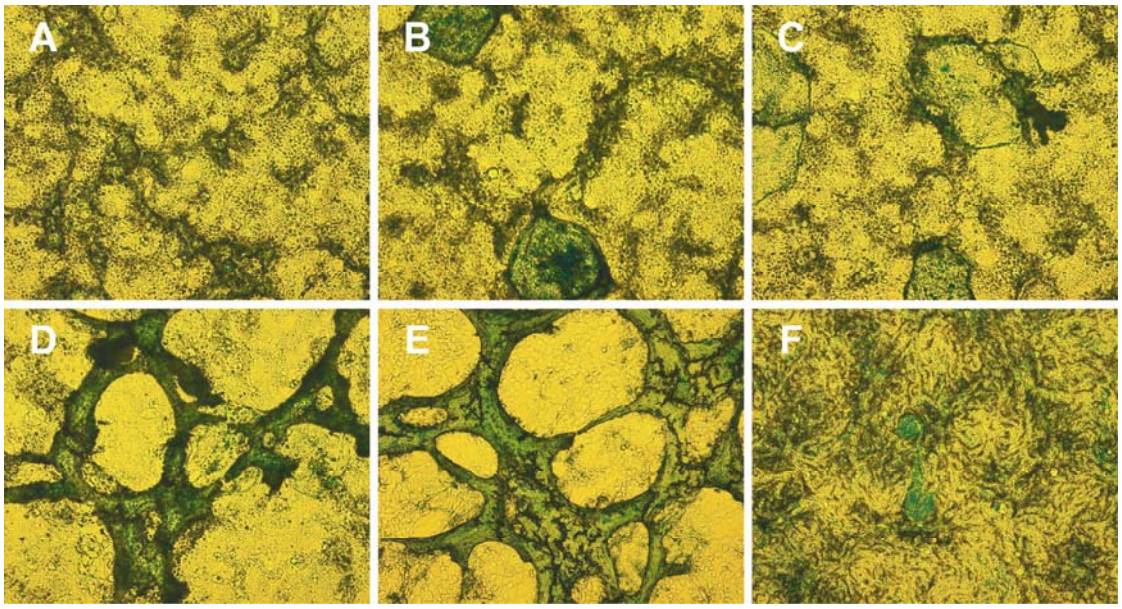

Figure 2.2. Co-cultures of Caco-2 and HT29-MTX stained with alcian blue (pH 2.5, stains acid mucosubstances blue) after 16 days in culture, ratios are Caco-2:HT29-MTX. The mucus stained more intensely above HT29-MTX cells, and this figure shows that the number of HT29-MTX cells after 16 days in culture increased as the initial seeding ratio of HT29-MTX cells increased. (A) Caco-2 (100:0), (B) 90:10, (C) 75:25, (D) 50:50, (E) 25:75, (F) HT29-MTX (0:100).

2.3.2. Cell protein levels and ferritin formation after direct contact with digest

Experiments were performed to determine if the mucus layer generated by the HT29-MTX cells could replace the 15,000 MWCO dialysis membranes, which are used in the *in vitro* digestion experiments to protect cell monolayers from the digestive

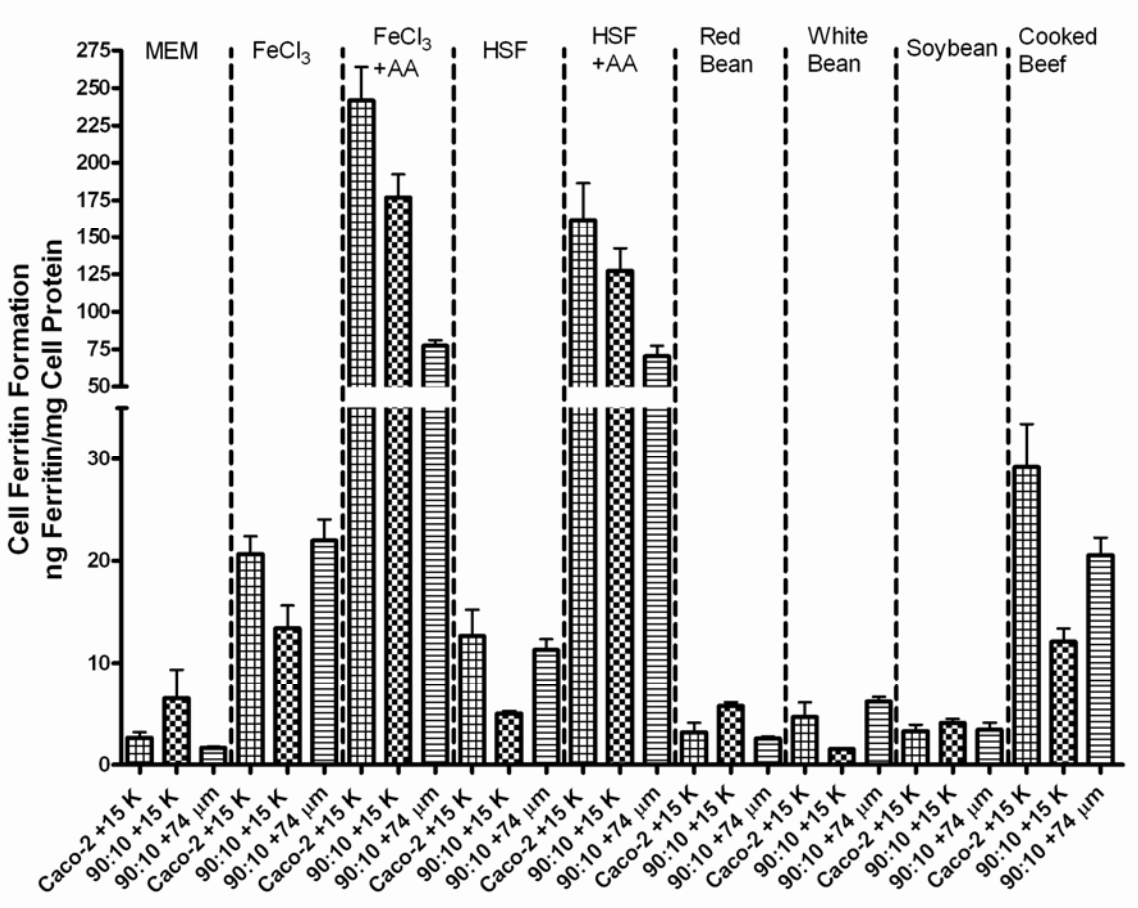

Figure 2.3. Cell ferritin formation of Caco-2 and 90:10 (Caco-2:HT29-MTX) cultures for 15,000 MWCO dialysis membrane inserts and 74 µm Netwell mesh inserts. Digests with $FeCl_3$ and horse spleen ferritin contained 50 µM iron and ascorbic acid, when present, was at a 1:20 (iron:ascorbic acid) molar ratio. Values are mean ± SEM, n = 4.

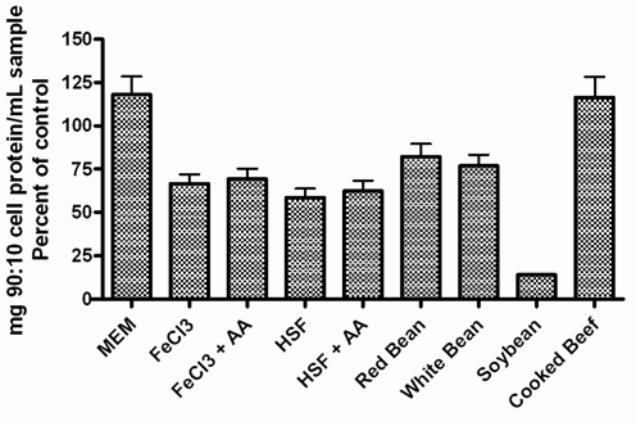

Figure 2.4. 90:10 (Caco-2:HT29-MTX) +74 µm mesh insert cell protein shown as a percent of 90:10 +15,000 MWCO dialysis membrane insert control.

enzymes. Netwell inserts with a 74 μm mesh were used in these experiments to screen out large food particles while still allowing the digest to come in contact with the cell monolayer. Figure 2.3 shows the results of an *in vitro* digestion experiment where the digest was placed into 15,000 MWCO dialysis membrane inserts or 74 μm Netwell mesh inserts. The addition of 10% HT29-MTX cells to the monolayer decreased the ferritin formation for the 15,000 MWCO and 74 μm mesh inserts when compared with the Caco-2 +15,000 MWCO membrane control. For the $FeCl_3$, HSF, white bean, and cooked beef treatments it appears that the co-cultures with 74 μm mesh inserts are more sensitive to iron in the digests because the cells formed more ferritin than the co-cultures with a 15,000 MWCO insert. Figure 2.4, however, shows that the co-culture cell protein is lower (50% - 75% of the control) when the 74 μm mesh inserts are used. The cell protein is lowest for the treatments without food to act as a buffer ($FeCl_3$, $FeCl_3$ + AA, HSF, and HSF + AA) and for the uncooked soybeans. The cell protein levels are also higher than the control for the cooked beef digest. This is most likely due to animal protein from the cooked beef sample that remained on the monolayer after the washing steps. These low cell protein levels indicate substantial cell loss and damage, which invalidate the ferritin formation results.

Increasing the ratio of HT29-MTX cells in the monolayers and diluting the digests with culture medium were both attempted to remedy the cell death and damage caused by contact with the digestive enzymes in the experimental digests. Two treatments ($FeCl_3$ and $FeCl_3$ + AA) with highly bioavailable iron that were shown in previous experiments to damage cells were used. Digests were diluted with MEM after 2 hours of contact with the cell monolayer. Figure 2.5 shows the results of these co-culture dilution experiments. These results show that increasing the amount of culture medium in the culture well does not alter the baseline ferritin formation (MEM only

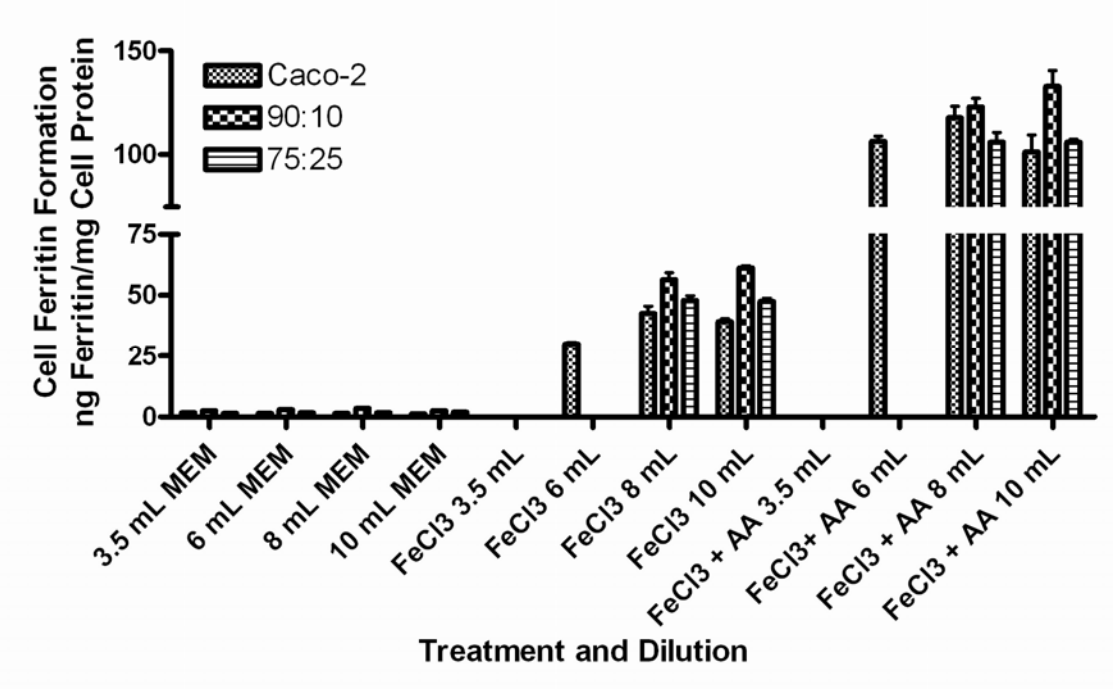

Figure 2.5. Cell ferritin formation of Caco-2, 90:10, and 75:25 (Caco-2:HT29-MTX) cultures with 74 μm Netwell mesh inserts and digest dilution with MEM. Dilution by a factor of ~4 or ~5.5 resulted in cell survival after 24 hours. Dilution factor is the total fluid in each culture well, which includes 1.5 mL digest and MEM. Treatments without bars had no viable cells. Digests with $FeCl_3$ and horse spleen ferritin contained 50 μM iron and ascorbic acid, when present, was at a 1:20 (iron:ascorbic acid) molar ratio. Values are mean ± SEM, n = 4.

treatments). The results also show that increasing the ratio of HT29-MTX cells does not increase resistance to the digestive enzymes, but diluting the digest by a factor of ~4 or ~5.5 (8 mL or 10 mL total fluid in the well, respectively) results in cell survival after 24 hours.

Figure 2.6 is the results from an experiment where Caco-2 and co-cultures of Caco-2 and HT29-MTX (90:10 ratio) were exposed to digests in 15,000 MWCO membrane or 74 μm mesh inserts. The digests in wells with 74 μm mesh inserts were diluted by a factor of ~5.5 with MEM (total fluid in well was brought up to 10 mL with MEM) after two hours in contact with the cell monolayers. These results show that direct contact with the digest decreases the cell ferritin formation for Caco-2 and 90:10 cultures; this decrease was most dramatic for Caco-2 cultures in contact with

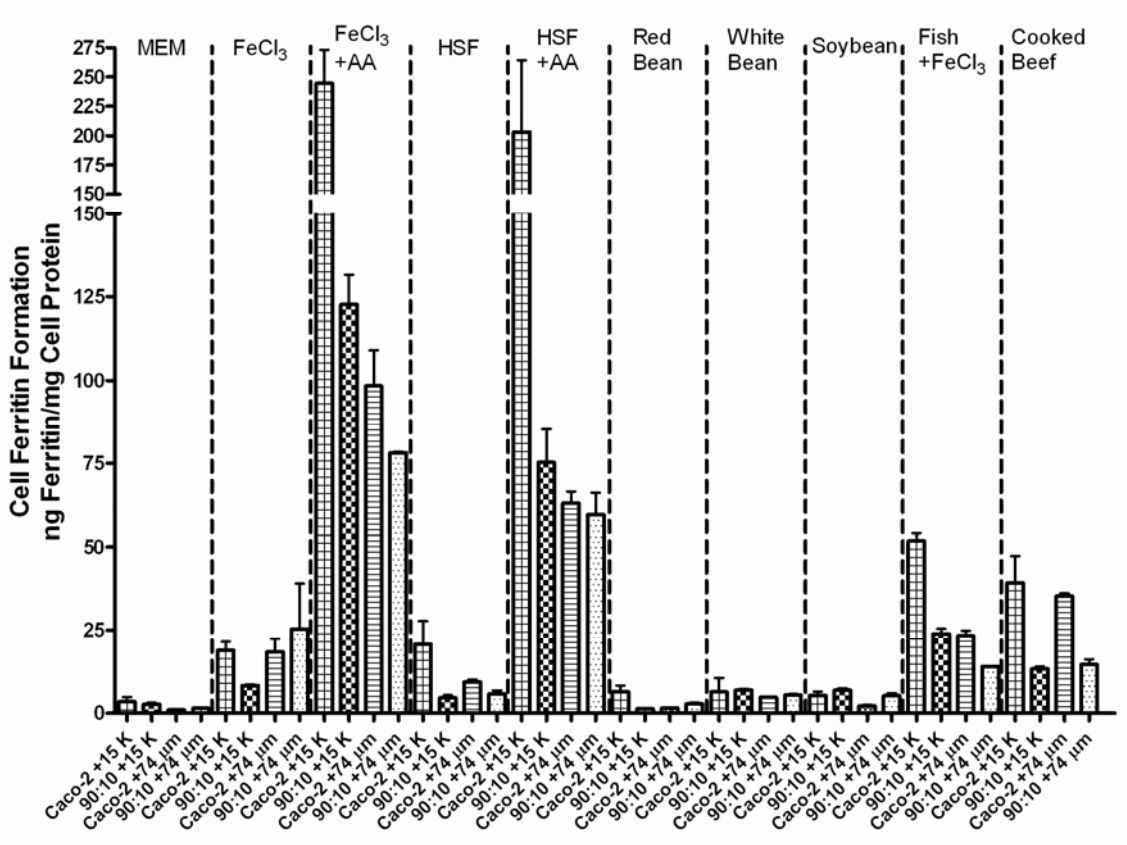

Figure 2.6. Cell ferritin formation of Caco-2 and 90:10 (Caco-2:HT29-MTX) cultures with 15,000 MWCO membrane or 74 μm mesh inserts. Digests in cultures with 74 μm mesh inserts were diluted by a factor of ~5.5 with MEM (10 mL total fluid in each well) after 2 hours in contact with the cell monolayer. Digests with $FeCl_3$ and horse spleen ferritin contained 50 μM iron and ascorbic acid, when present, was at a 1:20 (iron:ascorbic acid) molar ratio. Values are mean ± SEM, n = 3.

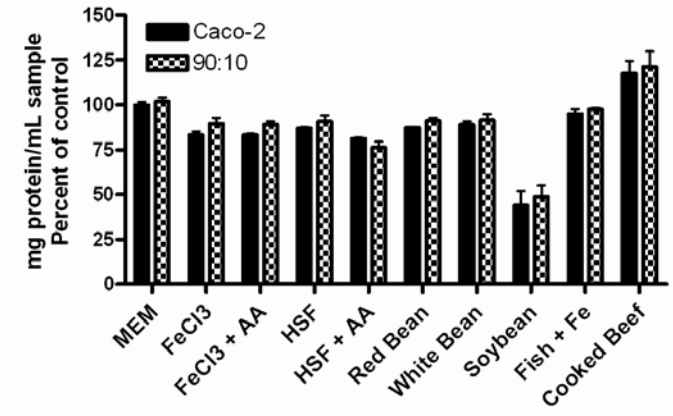

Figure 2.7. Caco-2 and 90:10 (Caco-2:HT29-MTX) +74 μm mesh insert, factor of ~5.5 digest dilution (10 mL total fluid in each well) cell protein shown as a percent of +15,000 MWCO dialysis membrane insert control.

highly available iron digests. Figure 2.7 shows the Caco-2 and 90:10 protein levels after direct contact with the digests. These results show that, excluding the uncooked soybean sample, diluting the digests allowed the cells to better withstand the digestive enzymes for a variety of different food samples. For the cooked beef and fish samples, however, cell protein was most likely overestimated due to interaction of sample animal protein with the cell protein assay.

2.3.3. Cell ferritin formation for varying ratios of Caco-2 to HT29-MTX cells

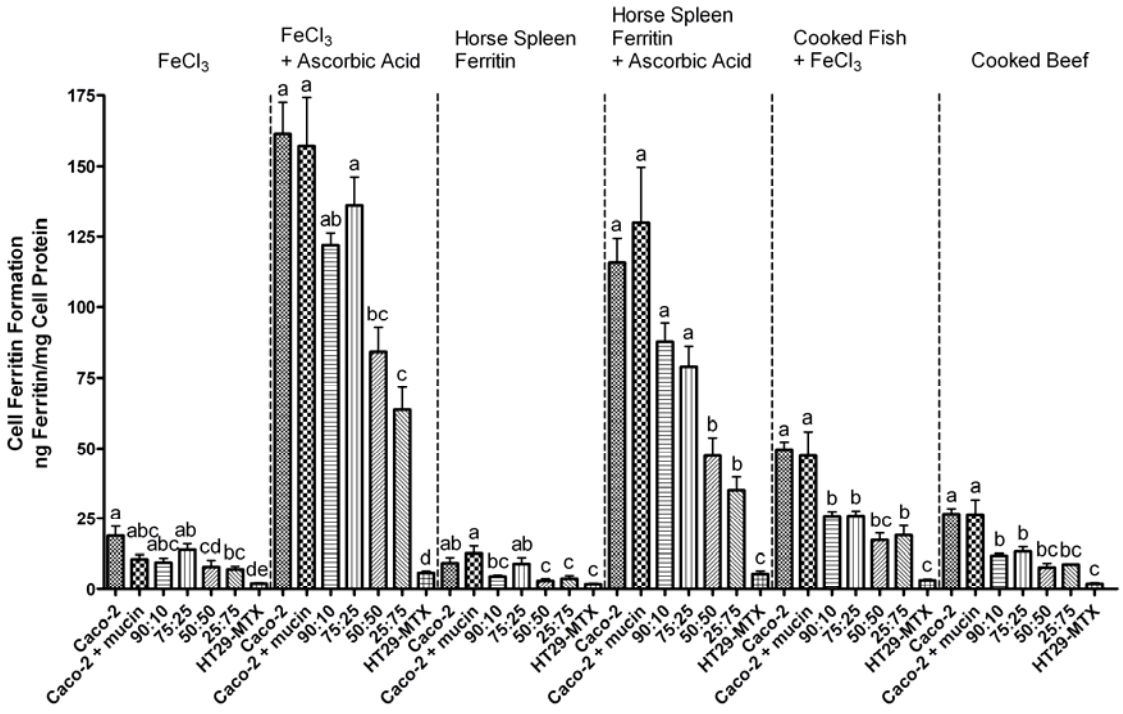

Figure 2.8. Cell ferritin formation in response to high available iron digests in 15,000 MWCO membrane inserts. Caco-2, Caco-2 overlaid with porcine mucin, co-cultures of Caco-2 and HT29-MTX (ratios are Caco-2:HT29-MTX), and HT29-MTX were used in experiments. Digests with $FeCl_3$ and horse spleen ferritin contained 50 μM iron and ascorbic acid, when present, was at a 1:20 (iron:ascorbic acid) molar ratio. Values are mean ± SEM, n = 9. Bars with no letters in common are significantly different ($p < 0.05$).

Table 2.1. Average cell ferritin formation (ng ferritin/mg cell protein) for similar forms of highly available iron as a percent of Caco-2 control (Caco-2 cells without porcine mucin). Ratios are Caco-2:HT29-MTX, n = 9.

	$FeCl_3$ + Ascorbic Acid	Horse Spleen Ferritin + Ascorbic Acid	Cooked Fish + $FeCl_3$	Cooked Beef
Caco-2 + mucin	97%	113%	96%	99%
90:10	75%	76%	52%	45%
75:25	84%	68%	52%	50%
50:50	52%	41%	35%	29%
25:75	40%	31%	38%	33%
HT29-MTX	4%	5%	6%	7%

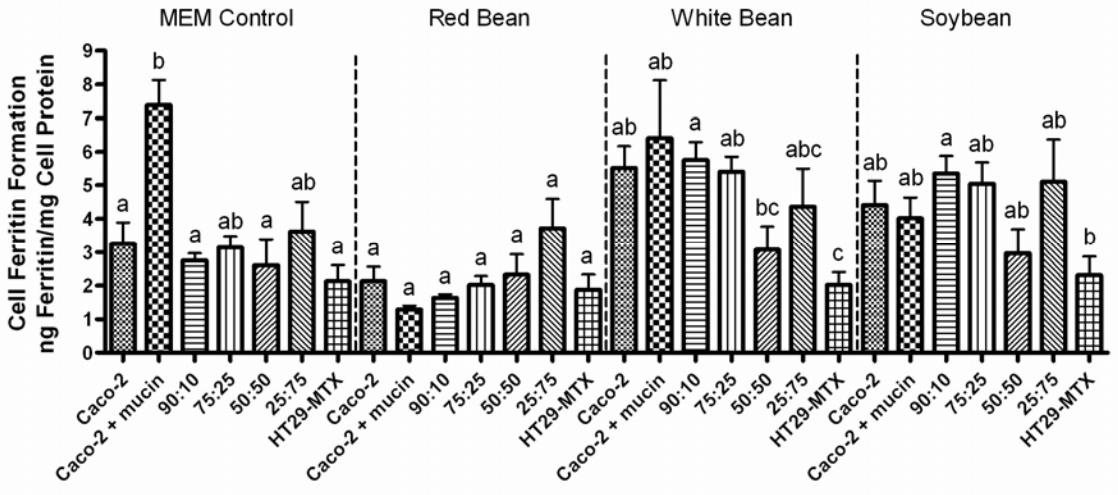

Figure 2.9. Cell ferritin formation in response to low available iron digests. Caco-2, Caco-2 overlaid with porcine mucin, co-cultures of Caco-2 and HT29-MTX (ratios are Caco-2:HT29-MTX), and HT29-MTX were used in experiments. Values are mean ± SEM, n = 9. Bars with no letters in common are significantly different ($p < 0.05$).

For experiments where all cultures were exposed to digests in 15,000 MWCO membranes, the addition of HT29-MTX mucus producing cells generally reduced the amount of ferritin formed, and as the ratio of HT29-MTX cells increased the ferritin formation in the cultures decreased. The decrease in ferritin formation due to added HT29-MTX cells was most significant for digests with highly available iron ($FeCl_3$, $FeCl_3$ + AA, HSF, HSF + AA, cooked fish + $FeCl_3$, cooked beef, Figure 2.8). Caco-2

cells and co-cultures presented iron in similar forms (heme iron, iron plus promoter) responded in a very consistent, reproducible manner (Table 2.1). Digests with less bioavailable iron (MEM control, red bean, white bean, and soybean) showed fewer statistically significant differences in ferritin formation between different cell preparations (Figure 2.9). The porcine mucin preparation used in this study had an original iron content of 274 mg iron/L, which after treatment with a chelating resin was reduced to 1.4 mg/L. The remaining iron in the mucin is most likely responsible for the significantly larger ferritin formation in Caco-2 + mucin cultures exposed to only MEM (Figure 2.9).

2.3.4. Effects of mucus layer removal and culture medium

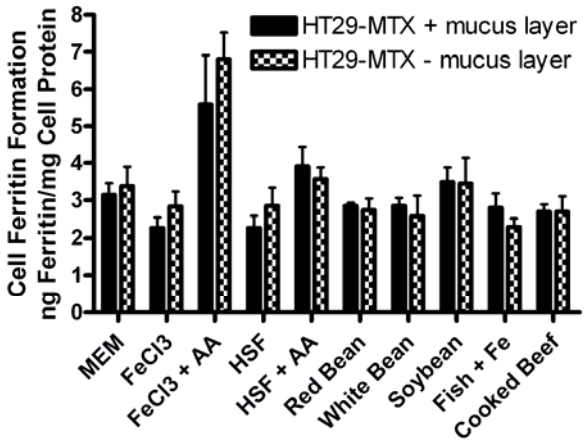

Figure 2.10. HT29-MTX cell ferritin formation with and without a mucus layer. Digests with $FeCl_3$ and horse spleen ferritin (HSF) contained 50 μM iron and ascorbic acid (AA), when present, was at a 1:20 (iron:ascorbic acid) molar ratio. Values are mean ± SEM, n = 3, $p < 0.05$.

Iron bioavailability experiments were performed with HT29-MTX cells with a mucus layer and with the mucus layer removed (Figure 2.10). These results show that removing the mucus layer over the HT29-MTX cells did not increase the ferritin formation by the cells. HT29-MTX protein levels were unchanged after mucus

removal, which indicated that there was little cell death and detachment due to the mucus removal process. Experiments were also performed with Caco-2 cells only in DMEM or in co-culture medium to determine the effects of culture medium on iron bioavailability (Figure 2.11). On day 15 in culture, cells grown in DMEM or in co-culture medium were rinsed once in MEM and cultured overnight in MEM. There was no statistically significant difference in ferritin formation between Caco-2 cells grown for 15 days in DMEM or co-culture medium.

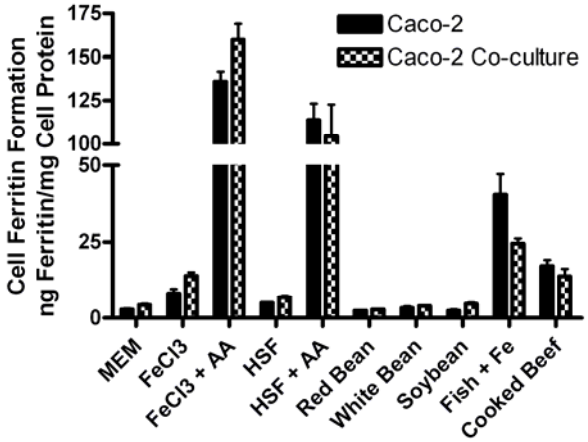

Figure 2.11. Caco-2 cell ferritin formation in DMEM and co-culture medium. DMEM contained 4.5 g/L glucose, 25 mM HEPES buffer, and 10% fetal bovine serum. Co-culture medium was DMEM containing 4 mM Glutamax, 4.5 g/L glucose, and 10% heat inactivated fetal bovine serum. Digests with $FeCl_3$, and horse spleen ferritin (HSF) contained 50 μM iron and ascorbic acid (AA), when present, was at a 1:20 (iron:ascorbic acid) molar ratio. Values are mean ± SEM, n = 3, $p < 0.05$.

2.4. Discussion

Iron is primarily available from food in two forms: nonheme iron from foods like vegetables or cereals, and heme iron in the form of hemoglobin or myoglobin from animal sources [28]. There are currently heme, ferrous, and ferric iron absorption pathways that have been identified in the intestinal epithelium [29]. Heme iron is more efficiently absorbed than inorganic iron from the diet because heme iron is soluble at

the pH of the small intestine, and a recently discovered importer, HCP1, mediates dietary heme iron uptake [29, 30]. Most inorganic, nonheme iron in the diet is present as the Fe^{3+} form. Ferric iron precipitates in solutions with pH 3 or higher, and must be bound by dietary components or intestinal mucins to stay in solution when it enters the less acidic duodenum [29]. The ferrireductase duodenal cytochrome B (Dcytb) reduces ferric iron to its ferrous form, which allows iron to be transported into intestinal epithelial cells by the divalent metal transporter DMT1 [28]. In the IMP, or integrin-mobleferrin pathway, ferric iron is transported across the apical surface of intestinal cells by β3-integrin and mobilferrin before cytosolic reduction by parraferritin [31, 32].

In the small intestine, goblet cells secrete mucus that forms a coating over the epithelial layer. There is a loosely adherent layer and a layer that is firmly attached to the mucosa. The thickness of the loosely and firmly adherent mucus has been measured in rats from stomach to colon; in the human duodenum, where most iron absorption takes place, the firmly adherent mucus layer is approximately 15 μM thick [33, 34]. The main functions of mucus include protecting the epithelium from mechanical damage, acidic gastric secretions, and digestive enzymes [35]. Mucus binds pathogenic viruses and bacteria to help prevent infection and aids in the digestion process by immobilizing enzymes near the epithelium surface, allowing for better nutrient hydrolysis and absorption [35]. The mucus also forms a semi-permeable barrier that allows ions and small molecules (MW < 1000) to pass, but is impermeable to larger molecules (MW > 17,000) [36]. All of these attributes illustrate that mucus plays an essential role in human nutrition and health. Additionally, the concentration of mobilferrin and DMT1 found in mucin and the ability of mucin to stabilize soluble iron as the luminal pH rises and to accept iron from chelates also indicate that mucus influences iron bioavailability.

Staining of the co-cultured Caco-2 and HT29-MTX monolayers showed that the mucus layer formed is about 2/3 of the thickness (2-10 μm) of the duodenal firmly adherent mucus layer in humans (15 μm), and that the mucus layer is continuous over the Caco-2 and HT29-MTX cells even at lower ratios of HT29-MTX cells (Figure 2.1). The mucus layer was more firmly adherent over the HT29-MTX cells and could withstand multiple washing steps. Since the acid mucosubstances stained with alcian blue stained more intensely above HT29-MTX cells, Figure 2.2 shows that as the initial seeding ratio of HT29-MTX cells increased there was a higher ratio of HT29-MTX cells present after 16 days in culture. Visual examinations of the cell monolayers over the 16 days in culture suggest that there is no observable change in the cell ratios.

Experiments characterizing the *in vitro* digestion/co-culture culture model without 15,000 MWCO dialysis membrane inserts were performed in an effort to make model conditions closer to those *in vivo*. The 15,000 MWCO dialysis membranes are used to protect the cell monolayers from digestive enzymes in samples, but also add an artificial barrier to iron absorption. Figure 2.3 shows that the 90:10 monolayers exposed directly to digest were more sensitive than 90:10 monolayers with a 15,000 MWCO membrane for $FeCl_3$, HSF, white bean, and cooked beef samples, but the 90:10 + 74 μm insert cell protein loss (Figure 2.4) prevents these results from being reliable.

Methods tested to reduce cell protein loss after a 24 hour exposure to digest included increasing the proportion of HT29-MTX cells and diluting digests with MEM by a factor of approximately 3, 4, or 5.5 after 2 hours in contact with the monolayer (Figure 2.5). Increasing the proportion of HT29-MTX cells did not protect the monolayers from damage, but dilution by a factor of 4 or 5.5 did improve cell viability. Digests were diluted by a factor of 5.5 for Caco-2 and 90:10 monolayers exposed directly to a range of food samples (Figure 2.6). The digest dilution prevented

major cell loss (Figure 2.7), but significantly decreased the ferritin formation by both Caco-2 and 90:10 cultures. The ferritin formation by Caco-2 and 90:10 cultures exposed directly to digest was statistically the same for nearly all samples, therefore the decrease in ferritin formation was most likely due to cell damage and not interaction of the sample with the mucus layer. Studies after this point were performed with 15,000 MWCO membrane inserts to determine if the mucus layer formed by HT29-MTX cells was interacting with samples without the confounding factor of cell damage caused by direct contact with digestive enzymes.

The results of experiments with Caco-2, Caco-2 + mucin, Caco-2 and HT29-MTX co-cultures, and HT29-MTX with 15,000 MWCO membrane inserts show that including goblet-like cells in the *in vitro* digestion model has significant effects on iron bioavailability predictions. In the presence of high bioavailable iron digests, co-cultures of Caco-2 and HT29-MTX had significantly lower cell ferritin formation (Figure 2.8). The high available iron digests presented iron to the cells as ferrous iron with and without a promoter ($FeCl_3$ and $FeCl_3$ + AA), as a whole ferritin molecule with and without promoter (HSF and HSF + AA), as heme iron (cooked beef), and as a low iron meat supplemented with iron to display the meat factor effect (cooked fish + Fe). There are three possibilities for why the addition of goblet-like cells and a mucus layer to this model decreases ferritin formation. First, the mucus layer in co-cultures could act as a barrier to and reduce the speed of iron absorption. Experiments with HT29-MTX cells with and without a mucus layer (Figure 2.10), however, showed that removing the mucus layer over the cells does not increase the cell ferritin formation; indicating that the more substantial mucus layer present as the HT29-MTX cell ratio increases is not interacting with the digests. Second, in conditions where iron is easily absorbed it is possible that the HT29-MTX cells themselves and not interactions between the digests and the mucus layer causes a decrease in cell ferritin

formation. The HT29-MTX cells, in a characteristic that is true to the goblet cells they are mimicking, absorb less iron and produce less ferritin than the absorptive cell analog Caco-2 cells, and the decrease in ferritin formation would be due to Caco-2 cell dilution. The third possibility is that a combination of the mucus layer and goblet cells influences cell ferritin formation.

In the human small intestine, the ratio of goblet cells ranges from 10% the small intestine to 24% in the distal colon [37]. At ratios of 90:10 and 75:25 (Caco-2:HT29-MTX), the co-culture ferritin formation was generally lower than the Caco-2 cultures, but this difference was statistically significant only for the cooked fish +Fe and cooked beef digests. These results suggest that at the 90:10 and 75:25 ratios there is a Caco-2 cell dilution effect that results in decreased ferritin formation, but the model still remains responsive to changes in iron bioavailability.

In digests with low available iron there was very little difference in cell ferritin formation between Caco-2 cells and co-cultures (Figure 2.9). The low available iron digests were the MEM control and iron presented in mostly ferric form from plant sources (red bean, white bean, and uncooked soybean). The minor differences between Caco-2 and co-cultures in low iron bioavailability conditions could mean that the cells present absorb all available iron or that the mucus layer in the co-cultures aids in iron absorption and helps to compensate for the lack of Caco-2 cells. Experiments in the future studying the effects of co-cultures in the presence of iron absorption inhibitors such as tannic acid could help to determine if the mucus layer aids in iron absorption from low available iron digests.

Experiments by Jin et al. showed that the application of porcine mucin to Caco-2 monolayers before placing digests in an 8 μm pore size, polycarbonate Transwell insert above the monolayers significantly increased iron bioavailability from digests containing heme and large molecules such as ferritin, but decreased the

iron bioavailability from white beans [26]. The experiments performed for this study were slightly different in that a 15,000 MWCO dialysis membrane was used for Caco-2 + mucin treatments instead of an 8 μm pore size, polycarbonate membrane. This difference could explain the fact that in this work the porcine mucin did not increase ferritin formation for heme iron or large molecule digests or significantly decrease iron bioavailability in white beans. As noted by Jin, the mucin conditions are difficult to reproduce and this may have also been a factor in the discrepancy between the two studies [26]. The use of reconstituted porcine mucin for this study was only for comparison purposes, as this product bears little resemblance to the natural product of goblet cells [38]. In general, the co-cultures outperformed the mucin analog by maintaining their original seeding ratios and forming ferritin from digests in a fairly consistent manner from experiment to experiment. The different ratios of Caco-2 to HT29-MTX also responded consistently to similar forms of iron such as heme iron or iron with a promoter (Table 2.1).

In conclusion, co-cultures of Caco-2 and HT29-MTX represent the two major cell types found in the human intestinal epithelium. HT29-MTX cells form a more physiologically realistic mucus layer that may interact with food digests and influence iron bioavailability predictions. In preliminary studies, increasing ratios of HT29-MTX cells decreased the amount of ferritin formation in high available iron digests such as those containing ferrous iron, heme iron, and whole ferritin molecules. For low available iron digests, which present iron to the cells in mostly ferric form, increasing the ratio of HT29-MTX cells had no effect on ferritin formation. The physiologically realistic ratios of 90:10 and 75:25 (Caco-2:HT29-MTX) offer the best compromise between model response and the presence of a mucus layer. These ratios are recommended for future work with the *in vitro* digestion/cell culture model, as the addition of goblet-type cells may give more accurate iron bioavailability predictions

and further enhance this rapid, low cost tool to assess iron bioavailability from different foods and food combinations.

REFERENCES

1. WHO, UNICEF, UNU. Iron deficiency anemia: Assessment, prevention, and control. A guide for programme managers; 2001; Geneva. World Health Organization. WHO/NHD/01.3.

2. Trowbridge F, Martorell R. 2002. Summary and recommendations. *Journal of Nutrition*. 132(4):875S-879S.

3. Reddy MB, Cook JD. 1991. Assessment of dietary determinants of nonheme-iron absorption in humans and rats. *American Journal of Clinical Nutrition*. 54(4):723-728.

4. Glahn RP, Lee OA, Yeung A, Goldman MI, Miller DD. 1998. Caco-2 cell ferritin formation predicts nonradiolabeled food iron availability in an *in vitro* digestion Caco-2 cell culture model. *Journal of Nutrition*. 128(9):1555-1561.

5. Glahn RP, Lee OA, Miller DD. 1999. *In vitro* digestion/Caco-2 cell culture model to determine optimal ascorbic acid to Fe ratio in rice cereal. *Journal of Food Science*. 64(5):925-928.

6. Glahn RP, Wortley GM, South PK, Miller DD. 2002. Inhibition of iron uptake by phytic acid, tannic acid, and $ZnCl_2$: Studies using an *in vitro* digestion/Caco-2 cell model. *Journal of Agricultural and Food Chemistry*. 50(2):390-395.

7. Glahn RP, Rassier M, Goldman MI, Lee OA, Cha J. 2000. A comparison of iron availability from commercial iron preparations using an *in vitro* digestion/Caco-2 cell culture model. *Journal of Nutritional Biochemistry*. 11(2):62-68.

8. Tinawi M, Martin KJ, Bastani B. 1996. Oral iron absorption test in patients on CAPD: Comparison of ferrous sulfate and a polysaccharide ferric complex. *Nephron*. 74(2):291-294.

9. Au AP, Reddy MB. 2000. Caco-2 cells can be used to assess human iron bioavailability from a semipurified meal. *Journal of Nutrition*. 130(5):1329-1334.

10. Yun SM, Habicht JP, Miller DD, Glahn RP. 2004. An *in vitro* digestion/Caco-2 cell culture system accurately predicts the effects of ascorbic acid and polyphenolic compounds on iron bioavailability in humans. *Journal of Nutrition*. 134(10):2717-2721.

11. Beiseigel JM, Hunt JR, Glahn RP, Welch RM, Menkir A, Maziya-Dixon BB. 2007. Iron bioavailability from maize and beans: A comparison of human measurements with Caco-2 cell and algorithm predictions. *American Journal*

of Clinical Nutrition. 86(2):388-96.

12. Jin F, Rutzke M, Welch RM, Glahn RP. 2007. Is extrinsic isotope labeling of plant foods reliable for studies of iron absorption? *Journal of the Federation of American Societies for Experimental Biology*. 21(6):A1115.

13. Powell JJ, Whitehead MW, Lee S, Thompson RPH. 1994. Mechanisms of gastrointestinal absorption - dietary minerals and the influence of beverage ingestion. *Food Chemistry*. 51(4):381-388.

14. Powell JJ, Jugdaohsingh R, Thompson RPH. 1999. The regulation of mineral absorption in the gastrointestinal tract. *Proceedings of the Nutrition Society*. 58(1):147-153.

15. Conrad ME, Umbreit JN, Moore EG. 1993. Regulation of iron-absorption - proteins involved in duodenal mucosal uptake and transport. *Journal of the American College of Nutrition*. 12(6):720-728.

16. Conrad ME, Umbreit JN, Moore EG. 1994. Iron absorption and cellular uptake of iron. *Advances in Experimental Medicine and Biology*. 356:69-79.

17. Simovich M, Hainsworth LN, Fields PA, Umbreit JN, Conrad ME. 2003. Localization of the iron transport proteins mobilferrin and DMT-1 in the duodenum: The surprising role of mucin. *American Journal of Hematology*. 74(1):32-45.

18. Lesuffleur T, Barbat A, Dussaulx E, Zweibaum A. 1990. Growth adaptation to methotrexate of HT-29 human colon-carcinoma cells is associated with their ability to differentiate into columnar absorptive and mucus-secreting cells. *Cancer Research*. 50(19):6334-6343.

19. Dahiya R, Lesuffleur T, Kwak KS, Byrd JC, Barbat A, Zweibaum A, Kim YS. 1992. Expression and characterization of mucins associated with the resistance to methotrexate of human colonic adenocarcinoma cell line HT29. *Cancer Research*. 52(17):4655-62.

20. Wikman-Larhed A, Artursson P. 1995. Cocultures of human intestinal goblet (HT29-H) and absorptive (Caco-2) cells for studies of drug and peptide absorption. *European Journal of Pharmaceutical Sciences*. 3(3):171-183.

21. Walter E, Janich S, Roessler BJ, Hilfinger JM, Amidon GL. 1996. HT29-MTX/Caco-2 cocultures as an *in vitro* model for the intestinal epithelium: *In vitro in vivo* correlation with permeability data from rats and humans. *Journal of Pharmaceutical Sciences*. 85(10):1070-1076.

22. Hilgendorf C, Spahn-Langguth H, Regardh CG, Lipka E, Amidon GL, Langguth P. 2000. Caco-2 versus Caco-2/HT29-MTX co-cultured cell lines:

Permeabilities via diffusion, inside- and outside-directed carrier-mediated transport. *Journal of Pharmaceutical Sciences*. 89(1):63-75.

23. Kerss S, Allen A, Garner A. 1982. A simple method for measuring thickness of the mucus gel layer adherent to rat, frog and human gastric-mucosa - influence of feeding, prostaglandin, n-acetylcysteine and other agents. *Clinical Science*. 63(2):187-195.

24. Sandzen B, Blom H, Dahlgren S. 1988. Gastric mucus gel layer thickness measured by direct light-microscopy - an experimental study in the rat. *Scandinavian Journal of Gastroenterology*. 23(10):1160-1164.

25. Wikman A, Karlsson J, Carlstedt I, Artursson P. 1993. A drug absorption model based on the mucus layer producing human intestinal goblet cell-line HT29-H. *Pharmaceutical Research*. 10(6):843-852.

26. Jin FX, Welch R, Glahn R. 2006. Moving toward a more physiological model: Application of mucin to refine the *in vitro* digestion/Caco-2 cell culture system. *Journal of Agricultural and Food Chemistry*. 54(23):8962-8967.

27. Behrens I, Pena AIV, Alonso MJ, Kissel T. 2002. Comparative uptake studies of bioadhesive and non-bioadhesive nanoparticles in human intestinal cell lines and rats: The effect of mucus on particle adsorption and transport. *Pharmaceutical Research*. 19(8):1185-1193.

28. Andrews NC, Schmidt PJ. 2007. Iron homeostasis. *Annual Review of Physiology*. 69:69-85.

29. Conrad ME, Umbreit JN. 2002. Pathways of iron absorption. *Blood Cells Molecules and Diseases*. 29(3):336-355.

30. Shayeghi M, Latunde-Dada GO, Oakhill JS, Laftah AH, Takeuchi K, Halliday N, Khan Y, Warley A, McCann FE, Hider RC and others. 2005. Identification of an intestinal heme transporter. *Cell*. 122(5):789-801.

31. Conrad ME, Umbreit JN, Moore EG, Hainsworth LN, Porubcin M, Simovich MJ, Nakada MT, Dolan K, Garrick MD. 2000. Separate pathways for cellular uptake of ferric and ferrous iron. *American Journal of Physiology-Gastrointestinal and Liver Physiology*. 279(4):G767-G774.

32. Umbreit JN, Conrad ME, Hainsworth LN, Simovich M. 2002. The ferrireductase paraferritin contains divalent metal transporter as well as mobilferrin. *American Journal of Physiology-Gastrointestinal and Liver Physiology*. 282(3):G534-G539.

33. Atuma C, Strugala V, Allen A, Holm L. 2001. The adherent gastrointestinal mucus gel layer: Thickness and physical state *in vivo*. *American Journal of*

Physiology-Gastrointestinal and Liver Physiology. 280(5):G922-G929.

34. Newton JL, Jordan N, Pearson J, Williams GV, Allen A, James OFW. 2000. The adherent gastric antral and duodenal mucus gel layer thins with advancing age in subjects infected with helicobacter pylori. *Gerontology*. 46(3):153-157.

35. Montagne L, Piel C, Lalles JP. 2004. Effect of diet on mucin kinetics and composition: Nutrition and health implications. *Nutrition Reviews*. 62(3):105-114.

36. Allen A, Carroll NJH. 1985. Adherent and soluble mucus in the stomach and duodenum. *Digestive Diseases and Sciences*. 30(11):S55-S62.

37. Forstner JF, Forstner GG. 1994. Gastrointestinal mucus. Johnson LR, editor. New York: Raven Press.

38. Kocevar-Nared J, Kristl J, Smid-Korbar J. 1997. Comparative rheological investigation of crude gastric mucin and natural gastric mucus. *Biomaterials*. 18(9):677-681.

CHAPTER 3

AN *IN VITRO* INTESTINAL EPITHELIUM MODEL REVEALS INTERACTIONS BETWEEN NANOPARTICLE ABSORPTION AND IRON UPTAKE AND TRANSPORT

3.1. Introduction

Oral delivery is the preferred route of pharmaceutical administration due to the comparatively low medical costs and relatively high patient comfort, compliance and convenience [1]. The oral delivery of peptide (greater than three or four residues) and protein therapeutics, however, is difficult due to the harsh gastric and intestinal environments. There have been many studies that focused on improving the bioavailability of peptide and protein therapeutics, and the encapsulation of peptides or proteins within polymeric nanoparticles is one strategy that has resulted in some success [2].

There are several advantages to the use of polymeric nanoparticles for drug delivery including the ability to manipulate the polymer's physiochemical characteristics, drug release profile, and biological behavior [3]. Polymeric nanoparticle carriers are also more stable than other colloidal carriers in the gastrointestinal tract, and their size to surface area ratio favors absorption through the intestinal epithelium when compared with larger carriers [2]. Many potential peptide and protein therapeutics, such as insulin, would be administered at least daily, and very little is know about the chronic effects of nanoparticle ingestion.

While we are primarily concerned with emerging classes of engineered nanoparticles, many traditional particles enter the body through the intestines. It is

estimated that the average person in a developed country consumes 10^{12}-10^{14} manmade fine (0.1-1 μm diameter) to ultrafine (<100 nm diameter) particles per day [4]. The sources of these dietary particles are mainly TiO_2, silicates, and aluminosilicates. These micro and nanoparticles have negatively charged surfaces, are able to bind biomolecules in the gut lumen, absorb across the GI tract, and accumulate at the base of Peyer's Patches (i.e. concentrations of M cells) [4]. The ingestion of these particles has been hypothesized to promote the development of Crohn's disease, which is characterized by transmural inflammation of the GI tract that first appears over Peyer's patches [4]. The link is uncertain as there was no difference in microparticle consumption found between healthy patients and those with Crohn's disease, and limiting the amount of microparticles in the diet of Crohn's disease patients resulted in no improvement in their symptoms [5, 6]. A recent study, however, showed that dietary microparticles that interact with macrophages may increase the antigenic response toward bacterial antigens in the GI tract [7]. Interestingly, patients with Crohn's disease are also prone to iron deficiency, suggesting a possible link between nanoparticles and iron transport [8].

The goal of this work is to investigate the effects of oral nanoparticle exposure on the absorption of iron, an essential nutrient that is transported across the intestinal epithelium via complex, highly regulated, protein-assisted vesicular and nonvesicular mechanisms [9]. A physiologically realistic *in vitro* model of the intestinal epithelium was used to better understand if oral exposure to nanoparticles affects the normal function of the intestinal epithelium. Such a model of the intestinal epithelium requires at least three cell types: absorptive enterocytes, mucus-producing goblet cells, and M cells that are responsible for particle transport. Caco-2 and HT29-MTX cells were used to mimic the absorptive enterocyte and mucus-secreting goblet cells, respectively. After a growth period of two weeks, Caco-2 cells differentiate into a

polarized, enterocyte-like epithelial barrier; express microvilli and tight junctions; and are capable of paracellular, transcellular, active, and transcytotic transport [10, 11]. Caco-2 cells also express ferrireductase duodenal cytochrome b (Dcytb), the apical iron transporter divalent metal transporter 1 (DMT1), ferritin, the basolateral iron transporter ferroportin 1 (FPN1), the ferroxidase hephaestin (Heph), and transferrin; which are all of the major iron uptake, storage, transport, and carrier proteins [12, 13]. HT29-MTX cells are a subpopulation of HT29 human colonic adenocarcinoma cells selected for resistance to methotrexate (MTX) that consist exclusively of differentiated, mucus-secreting, goblet-like cells that retain their differentiated phenotype after reversion to MTX-free medium [14]. Cultures of Caco-2, HT29-MTX, and Raji mimicked the absorptive, goblet, and M cells present in the intestinal epithelium. The co-culture of Caco-2 cells with the Raji B cell lymphoma cell line has been shown to induce the transformation of Caco-2 epithelial cells into cells with an M cell-like morphology, including up-regulated Sialyl Lewis A antigen, β1 integrin localization on the apical pole of the cells and increased particle transport [15, 16].

The interaction of 50 nm and 200 nm carboxylated nanoparticles with Caco-2/HT29-MTX and +M cell (Caco-2/HT29-MTX/Raji B) monolayers was evaluated by examining the amount of particles transported by the cells. The effect of nanoparticles on normal cell function was assessed by studying the uptake and transport of iron after exposure to different concentrations of 200 nm or 50 nm carboxylated, non-ionized, or aminated particles. Overall, these results show that the charge, concentration, and transport mechanism of the nanoparticles can have an effect on the normal physiological functions of intestinal epithelial cells.

3.2. Materials and methods

3.2.1. Materials

Dulbecco's Modified Eagle Medium (DMEM); RPMI 1640 medium; Minimal Essential Medium (MEM); fetal bovine serum; heat inactivated fetal bovine serum; goat serum; trypsin-EDTA (0.25%); phosphate buffered saline (PBS); CellTracker™ CM-DiI cell membrane stain; Alexa Fluor® 488 goat anti-mouse IgG1; ProLong® Gold antifade reagent; and FluoSpheres® amine-modified, 200 nm, polystyrene, yellow-green particles were obtained from Invitrogen (Carlsbad, CA). The monoclonal antibody to CD29 (integrin β1 subunit) was from BioGenex (San Ramon, CA). Transwell® polycarbonate inserts (0.33 cm^2, 0.4 μm pore size) and solid black, 96 well assay plates were purchased from Corning Life Sciences (Corning, NY). Inserts were coated with 8 $\mu g/cm^2$ of Type I collagen from Becton Dickinson (Bedford, MA). Fluoresbrite® yellow-green, polystyrene, carboxylated and non-ionized 50 nm and 200 nm particles were acquired from Polysciences, Inc. (Warrington, Pennsylvania). Blue fluorescent, aminated, 50 nm particles were obtained from Sigma Aldrich (St. Louis, MO). $^{59}FeCl_3$ was purchased from PerkinElmer (Wellesley, MA), and $FeCl_3$ in 2% HCl stock solution was bought from High Purity Standards (Charleston, SC). Ferritin content of the cells was determined with a FER-IRON II one-stage, two-site immunoradiometric ferritin assay from RAMCO Laboratories (Houston, TX) and total cell protein concentration was determined with a Bio-Rad DC Protein Assay (Hercules, CA). All other chemicals, enzymes, and hormones were purchased from Sigma Aldrich. All glassware used in sample preparation and analysis was washed, soaked in 10% hydrochloric acid and 10% nitric acid overnight, and rinsed with 18 MΩ water to avoid iron contamination. All reagents were prepared in 18 MΩ water.

3.2.2. Cell culture

The human colon carcinoma Caco-2 cell line and human Burkitt's lymphoma Raji B cell line were obtained from the American Type Culture Collection (Manassas, VA). The HT29-MTX cell line was kindly provided by Dr. Thécla Lesuffleur of INSERM U560 in Lille, France [14]. Caco-2 cells were received at passage 17 and used in experiments at passages 30-35. HT29-MTX cells were received at passage 11 and used at passages 14-19. Caco-2 and HT29-MTX were grown in DMEM containing 4 mM Glutamax, 4.5 g/L glucose, and 10% heat inactivated fetal bovine serum. Raji cells were maintained in RPMI 1640 Medium with 2 mM L-glutamine, 4.5 g/L glucose, 10 mM 4-(2-hydroxyethyl)piperazine-1-ethanesulfonic acid (HEPES), 1.0 mM sodium pyruvate, and 10% fetal bovine serum. Nanoparticle and iron uptake and transport experiments were performed in serum free, very low iron (<8 μg Fe/L) MEM containing 10 mM piperazine-N,N'-bis-[2-ethanesulfonic acid] (PIPES), 4 mg/L hydrocortisone, 5 mg/L insulin, 5 μg/L selenium, 34 μg/L triiodothyronine, 20 μg/L epidermal growth factor, and 1% antibiotic-antimycotic solution [17]. The cells were maintained at 37°C in 5% CO_2 and culture medium was changed every 2 days. For experimental studies, Caco-2 and HT29-MTX were seeded at a density of 100,000 cells/cm^2 at a ratio of 3:1 Caco-2:HT29-MTX onto Transwell inserts. On day 15 of Caco-2/HT29-MTX culture, $1x10^6$ Raji cells were re-suspended in 50:50 DMEM:RPMI 1640 and added to the basolateral chamber of the Caco-2/HT29-MTX culture wells. The tri-cultures were maintained for 2 days with 100 μL of culture medium replaced every day in the basolateral chamber. Caco-2/HT29-MTX monolayers were used as controls and were cultured as above except for the addition of Raji cells.

3.2.3. TER measurements

Transepithelial resistance (TER) of the cell monolayers was measured every three days after seeding and every day following the addition of Raji cells to assess the confluency of the monolayers and tight junction functionality. Measurements were also made after nanoparticle transport experiments to reassess tight junction functionality after exposure to nanoparticles. TER measurements were made using the Millicell ERS from Millipore (Billerica, MA) with the Endohm-6 chamber from World Precision Instruments (Sarasota, FL). The chamber was sterilized prior to use with 70% ethanol for 15 min. After the chamber was equilibrated with 2 mL of PBS for 2 hours at room temperature, the Millicell ERS voltage was adjusted to a zero reading and the PBS was replaced with 600 μL of fresh measurement medium. The measurement medium for TER consisted of serum free DMEM. The culture plates were removed from the incubator 5 minutes prior to measurements to allow the culture medium to come to room temperature. Three measurements at different insert positions were taken per sample. Monolayers with TER values between 200 and 300 Ω/cm^2 were used in nanoparticle and iron uptake and transport experiments.

3.2.4. Nanoparticle uptake, transport and dose

Nanoparticle uptake and transport studies were performed 17 days post seeding. Cells were rinsed once with MEM and then 600 μL of MEM was placed into the basolateral chamber of the Transwells and 100 μL of MEM containing varying concentrations of aminated, non-ionized, or carboxylated 50 nm or 200 nm particles was placed into the apical chamber. Sodium azide was removed from 200 nm aminated particles via dialysis with a 15,000 molecular weight cut-off membrane. Cells were incubated at 37^{o}C and 5% CO_2 on a rocking shaker (Laboratory Instrument Model RP-50, Rockville, MD) at 6 oscillations/minute. A 100 μL sample was taken

from the basolateral chamber of each well at 15, 30, 45, 60, 120, 180, and 240 minutes and replaced with 100 μL MEM. Samples were placed into solid black, 96 well plates and read on a SpectraMax Gemini EM fluorescence microplate reader from Molecular Devices (Sunnyvale, CA). The number of particles transported through the cell monolayers was determined with a standard curve prepared using dilutions of MEM containing 50 nm or 200 nm particles.

Identical 200 nm and 50 nm particle transport experiments were performed at 4^{o}C to determine if the particle transport mechanisms were energy dependent. On day 17 post-seeding, cells were rinsed with MEM, 600 μL MEM was placed into the basolateral chamber, and 100 μL MEM with $2x10^{10}$ 50 nm or $1.25x10^{9}$ 200 nm particles was placed into the apical chamber. Cells were incubated at 4^{o}C on a rocking shaker at 6 oscillations/minute, and a 100 μL sample was taken from the basolateral chamber of each well after 45 minutes. Samples were placed into solid black, 96 well plates and read on a fluorescence microplate reader, and a standard curve was used to determine the number of particles transported through the cell monolayers.

3.2.5. ^{59}Fe uptake and transport

For iron uptake and transport experiments, ^{59}Fe was presented to the cells at a concentration of 10 μM iron as Fe(II)-ascorbate in MEM. The radiolabeled iron experimental medium was prepared immediately before use by combining $^{59}FeCl_3$ (iron-59 in 0.5 M hydrochloric acid), $FeCl_3$ (1000 μg Fe/L $FeCl_3$ standard in 2% HCl) and 100 μL of 100 mM ascorbic acid to provide ~7 kBq/mL, an iron concentration of 10 μM, and an Fe:ascorbic acid molar ratio of 1:20. After allowing the Fe(II)-ascorbate solution to sit at room temperature and pH 2 for 15 minutes, 167 μL of 1.5 M NaCl and 5 mL MEM were added. Immediately after the nanoparticle uptake and transport experiments, 100 μL of the radiolabeled iron transport medium was added to

the apical chamber. Cells were incubated at 37^{o}C and 5% CO_2 on a rocking shaker at 6 oscillations/minute for 120 minutes. Iron uptake and transport was terminated by transferring the apical and basolateral culture medium to scintillation vials for quantification of ^{59}Fe with an automatic gamma counter (Packard Auto-Gamma Model 5530, PerkinElmer Life and Analytical Sciences, Wellesley, MA). Cells were immediately washed twice with 200 μL in the apical chamber and 600 μL in the basolateral chamber of stop solution (130 mM NaCl, 5 mM KCl, 5 mM PIPES, pH 6.7). Removal solution (130 mM NaCl, 5 mM KCl, 5 mM PIPES, 5 mM bathophenanthrolinedisulfonic acid, 5 mM sodium dithionite) was then added to the monolayers. The removal solution has been shown to remove surface bound iron without damaging the cell membrane [18]. After 10 minutes, the removal solution was aspirated and the cells were washed twice with stop solution. Cells were lysed by adding 200 uL of water to the apical chamber and sonicating (Elma Transsonic Digital sonicator, Laboratory-Line Instruments Inc., Melrose, IL) for 15 minutes at 4^{o}C. The Transwell membrane was removed with a razor blade and placed into a scintillation vial with the corresponding aqueous cell lysate for ^{59}Fe quantification. The cell membranes and lysate were stored at -20^{o}C before ferritin and protein assays. Cell protein was measured in samples that had been solubilized in 0.5 M NaOH. A 10 μL sample of the sonicated cell monolayer, harvested in 200 μL of water, was used for each ferritin measurement.

3.2.6. In vitro digestion

Nanoparticle transport experiments were also performed after subjecting the nanoparticles to an *in vitro* digestion and using the chyme mimic as the nanoparticle transport solution. The *in vitro* digestion/Caco-2 cell culture model was developed by Glahn et al. for studying iron bioavailability from food [17]. The food of interest is

cooked and freeze dried before it is subjected to an hour long pepsin digestion at 37^{o}C and pH 2. The pepsin is then deactivated by raising the pH to 5.5-6.5 with sodium bicarbonate, a pancreatin-bile solution is added to the mixture, the pH is readjusted to 7.0, and the chyme mimic is placed in an insert over a Caco-2 monolayer. In the *in vitro* digestion/nanoparticle transport experiments 50 nm carboxylated particles were digested at a concentration of $2x10^{11}$ particles/mL in a blank digest (no food added) or a digest with 0.067 gram/mL of freeze dried nishiki rice (2.7 μg Fe/mL). An aliquot of 100 μL of the chyme mimic was placed directly onto the Caco-2/HT29-MTX or +M cell monolayers. All other details of the nanoparticle transport experiment were identical to those described above and controls were blank or rice digests with no nanoparticles.

3.2.7. Fluorescent evaluation of nanoparticle interaction with the cell monolayer

After carboxylated, 50 nm and 200 nm nanoparticle transport experiments, monolayers were washed once with PBS and then incubated with 1 μM CellTracker CM-DiI cell membrane stain in PBS for 20 minutes at 37^{o}C and for an additional 15 minutes at 4^{o}C. Cells were then washed with PBS, fixed with 2% paraformaldehyde for 20 minutes at 4^{o}C, and washed again with PBS. The membranes were removed with a razor blade and mounted on glass slides. After curing for 24 hours at room temperature in the dark, the slides were examined with a Leica TCS SP2 laser scanning spectral confocal microscope (Exton, PA).

3.2.8. Localization of β1 integrin

Cell monolayers cultured for 15 days and then with Raji cells for an additional 2 days were stained for β1 integrin. Controls were grown without Raji cells. Monolayers were washed twice with PBS, fixed in 2% paraformaldehyde for 20 minutes at 4^{o}C, and washed twice again with PBS. Cells were permeabilized with

0.1% Triton X-100 in PBS for 5 minutes at room temperature and then blocked with 5% bovine serum albumin and 1% goat serum in PBS for 1 hour, shaking at 100 rpm (Labnet International, Edison, NJ). The monolayers were then incubated for 2 hours at 37^{o}C with a 1:50 dilution of an anti-CD29 (β1-subunit) monoclonal antibody in PBS. The inserts were washed twice with PBS before being incubated for 1 hour with a 1:2000 dilution of Alexa Fluor 488 goat anti-mouse IgG1. The monolayers were then washed twice with PBS, removed with a razor blade, and mounted on glass slides. After curing for 24 hours at room temperature in the dark, the slides were examined with a Leica TCS SP2 laser scanning spectral confocal microscope.

3.2.9. Zeta potential

Zeta potential of particles was measured by dynamic light scattering with a Malvern Zetasizer Nano-ZS (Malvern Instruments Inc, Southborough, MA) at 25^{o}C. The zeta potential of 50 nm and 200 nm particles was measured in 18 MΩ water, MEM, and blank digest and each nanoparticle dispersion was measured three times.

3.2.10. Transmission electron microscopy

A 5 μL aliquot of MEM containing 2x10^{11} 50 nm particles/mL or 1.25x10^{10} 200 nm particles/mL was placed onto a copper grid coated with ~40 nm of formvar. Grids were analyzed with a FEI Tecnai T12 Spirit Twin Transmission Elecron Microscope.

3.2.11. Statistics

All measurements of nanoparticle transport and iron uptake and transport were made at least 6 times for each treatment. Cellular ferritin and total cell protein assays were also replicated at least 6 times. Results are expressed as mean ± standard error. Data was analyzed with the GraphPad Prism version 4.00 for Windows (GraphPad

Software, San Diego, CA). A one-way ANOVA with Tukey's post test was used to compare differences between means and data was transformed when necessary to obtain equal sample variances. Differences between means were considered significant at $p < 0.05$.

3.3. Results

3.3.1. Nanoparticle dose

Efforts were made to formulate *in vitro* doses of nanoparticles that were relevant to potential real-life exposure. It is known that the average person in an industrialized nation consumes 10^{12}-10^{14} manmade fine (0.1-1 mm diameter) to ultrafine (<100 nm diameter) particles per day [4]. The total surface area of the small intestine is $2x10^6$ cm^2, meaning that 10^{14} particles is a dose of 10^7 particles/cm^2 [19]. If 10^{12} or 10^{14} particles are ingested, the dose to the duodenum is approximately 10^9 or 10^{11} particles/cm^2, respectively. The duodenum is the first section of the small intestine, the site where most iron absorption occurs, and has approximately 900 cm^2 of absorbing surface area [20, 21]. If 0.02 mg/kg of 50 nm polystyrene particles were administered to a 70 kg human as a pharmaceutical, the dose to the small intestine would be 10^7 particles/cm^2 assuming that the particles are monodisperse and have a density of 1.053 g/cm^3 [22]. A 2 mg/kg and 200 mg/kg oral administration would translate to a 10^9 and 10^{11} particles/cm^2 dose to the small intestine, respectively.

The dose of 50 nm particles to the cell cultures used in this study, assuming that the presence of microvilli increases the surface area by 20 times [19], was 10^7, 10^9, and 10^{11} particles/cm^2 for the low ($2x10^9$ particles/mL), mid ($2x10^{11}$ particles/mL), and high ($2x10^{13}$ particles/mL) experimental concentrations used. The 200 nm particle dosages ($1.25x10^8$ particles/mL, $1.25x10^{10}$ particles/mL, and $1.25x10^{12}$ particles/mL) were determined by calculating the total surface area of

particles in the 50 nm particle dose and normalizing the 200 nm particle dose by surface area.

3.3.2. Cell monolayer and nanoparticle characterization

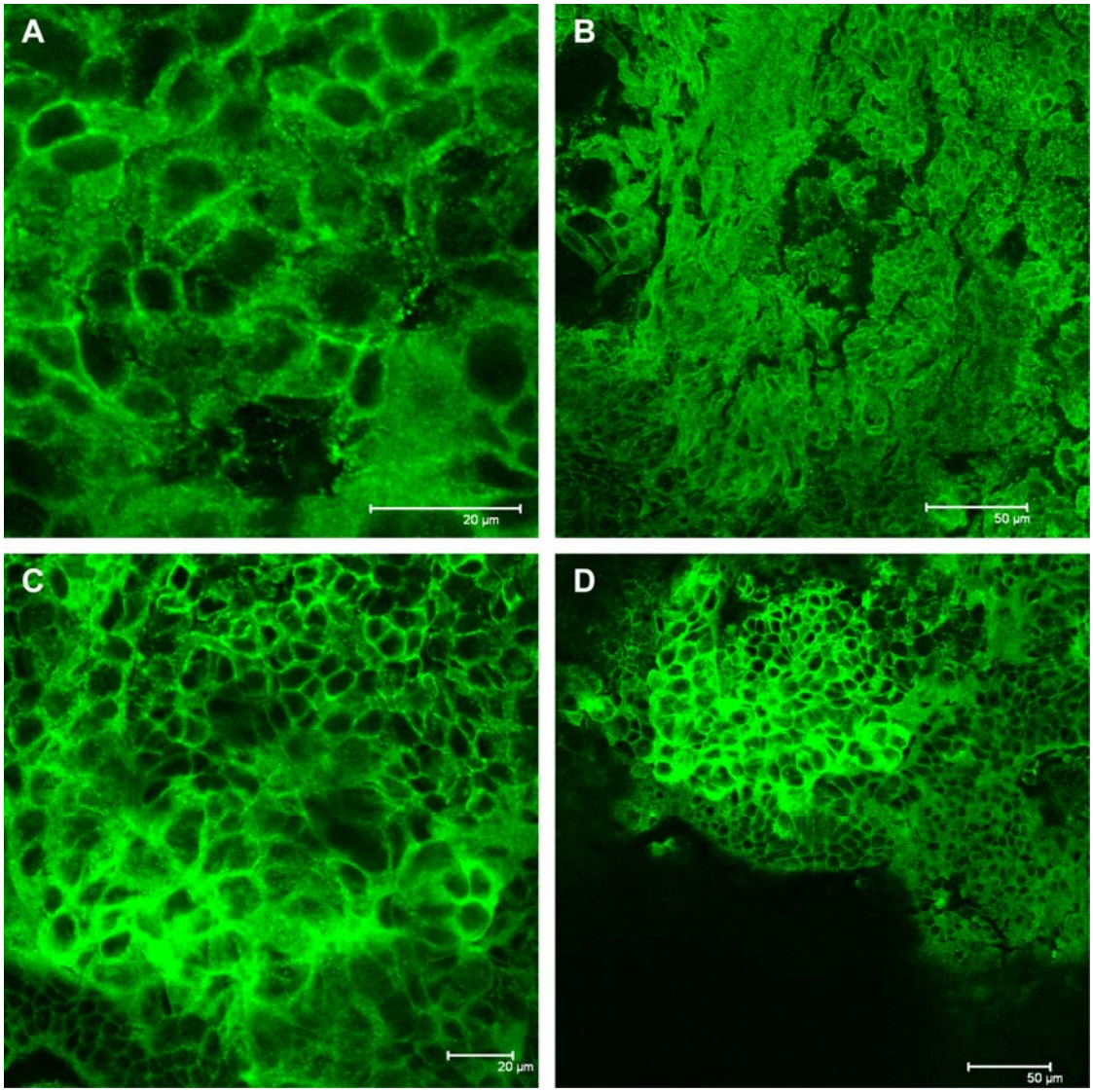

Figure 3.1. Confocal images of monolayers stained for β1-integrin. The Caco-2/HT29-MTX monolayer shows greater β1-integrin expression on the basolateral side of the membrane (A and B), while the +M cells monolayer exhibits apical expression (C and D). Scale bars are 20 μm (A and C) or 50 μm (B and D).

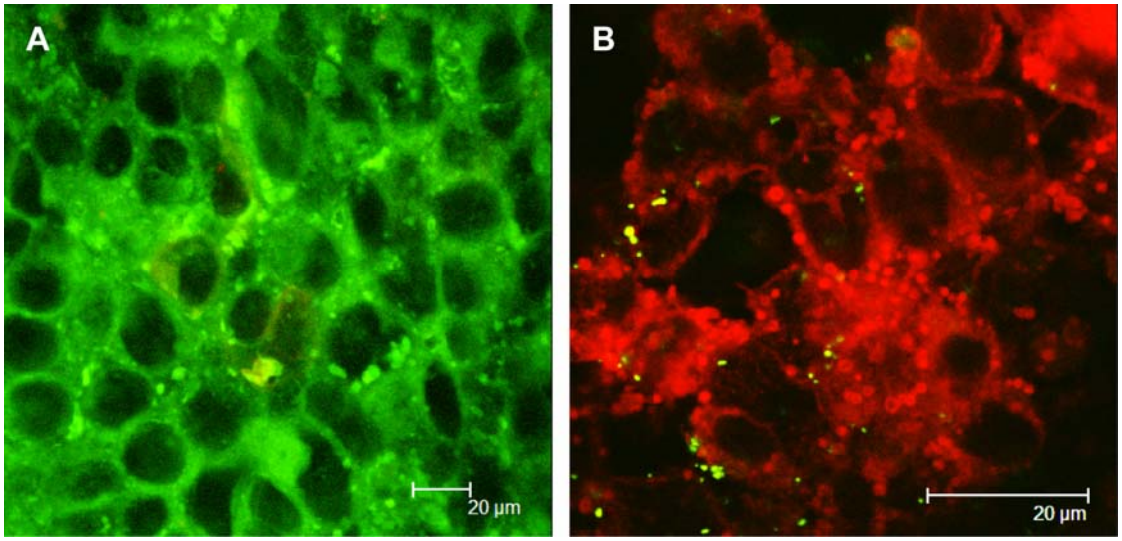

Figure 3.2. (A) + M cells monolayer stained with CellTracker™ CM-DiI cell membrane stain after 4 hours of exposure to 50 nm particles. The green particles and red cell membranes overlay, showing that the hydrophobic 50 nm polystyrene particles primarily diffuse through hydrophobic cell membranes. (B) +M cells monolayer stained with CM-DiI stain after 4 hours of exposure to 200 nm particles. The green particles and red cell membranes, in general, do not overlap and a greater number of vesicles can be seen. Scale bars are 20 µm.

Figure 3.1 shows the basolateral side of Caco-2/HT29-MTX monolayers (Figure 3.1A and 3.1B) and apical side of +M cells monolayers (Figure 3.1C and 3.1D) after staining for β1-integrins. β1-integrins are located at the apical pole of differentiated M cells, while mostly basolateral expression is seen in Caco-2/HT29-MTX cultures [23].

Figure 3.2A shows +M cells monolayers after a 4 hour exposure to $2x10^{10}$ 50 nm, carboxylated, yellow-green nanoparticles. Figure 3.2B shows +M cells monolayers after a 4 hour exposure to $1.25x10^{9}$ 200 nm, carboxylated, yellow-green nanoparticles. The 50 nm particles are localized to the cell membrane, while the 200 nm particles appear to be independent of the cell membrane or potentially within cell vesicles.

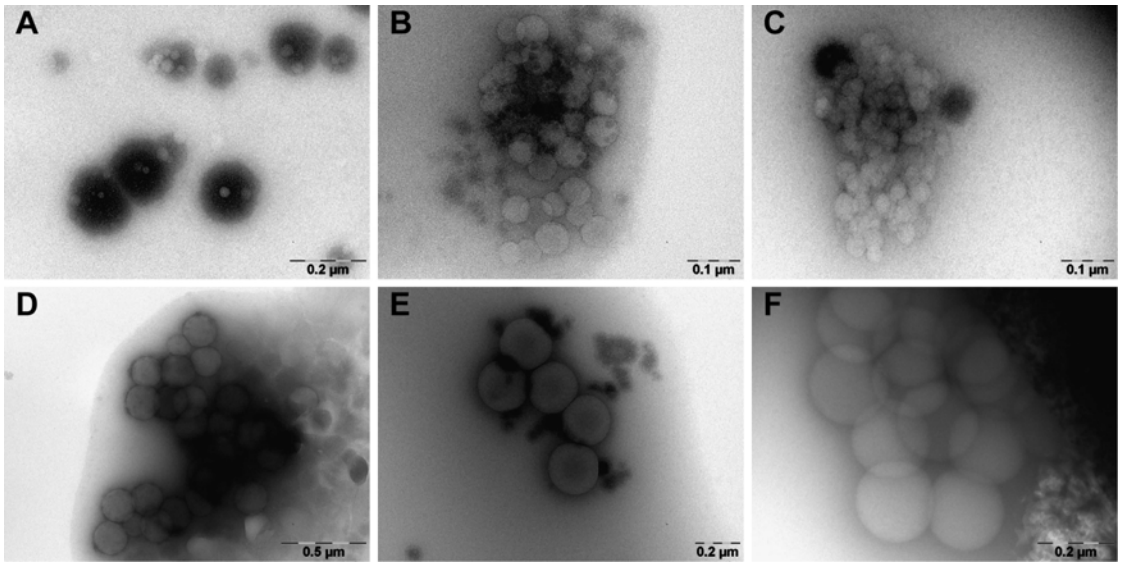

Figure 3.3. Transmission electron microscopy images of 50 nm and 200 nm particles in MEM. (A) 50 nm carboxylated, (B) 50 nm non-ionized, (C) 50 nm aminated, (D) 200 nm carboxylated, (E) 200 nm non-ionized, (F) 200 nm aminated.

Table 3.1. Zeta potential of particles in water, MEM, and blank digest.

ζ (mV)	18 MΩ water	MEM	Blank digest
Carboxylated 50 nm particles	-60.0 ± 5.9	-12.2 ± 0.7	-37.8 ± 1.8
Carboxylated 200 nm particles	-60.2 ± 5.1	-17.3 ± 0.4	-29.1 ± 1.0
Non-ionized 50 nm particles	-39.5 ± 2.9	-16.4 ± 0.8	
Non-ionized 200 nm particles	-43.9 ± 1.9	-17.3 ± 0.3	
Aminated 50 nm particles	27.1 ± 2.1	-6.2 ± 0.3	
Aminated 200 nm particles	10.5 ± 1.8	-9.2 ± 0.2	

The physical state of the nanoparticles in MEM was investigated using Transmission Electron Microscopy (TEM). Carboxylated nanoparticles appeared to aggregate the least, while aminated particles showed the most aggregation (Figure 3.3). The zeta potential of 50 nm and 200 nm carboxylated, non-ionized, and aminated nanoparticles in water and MEM and 50 nm carboxylated nanoparticles in blank digest is shown in Table 3.1. The increased zeta potential of carboxylated and non-ionized

particles in MEM and decreased zeta potential of aminated particles in MEM when compared with the zeta potential in water suggests that the particles were binding medium proteins. These medium proteins (small black dots) can be seen on the particle surfaces in Figure 3.3.

3.3.3. Nanoparticle transport

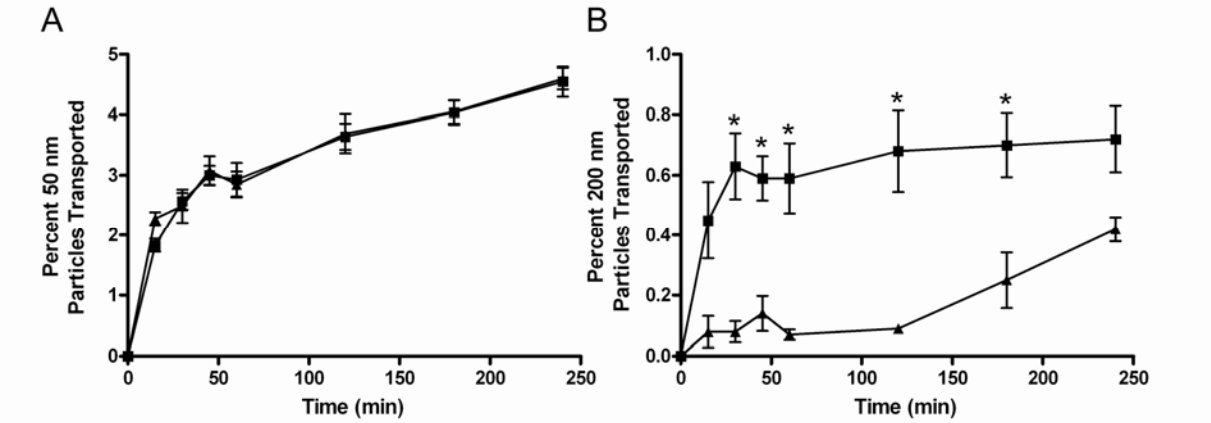

Figure 3.4. Results from 50 nm and 200 nm carboxylated particle transport experiments. (A) Caco-2/HT29-MTX cultures (▲) transported 4.55% and +M cells cultures (■) transported 4.60% of 50 nm particles after 4 hours. (B) Caco-2/HT29-MTX cultures (▲) transported 0.42% and +M cells cultures (■) transported 0.72% of 200 nm particles after 4 hours Error bars are ±SEM. Mean particle transport differences between Caco-2/HT29-MTX and +M cells cultures that are significant according to a one-way ANOVA with Tukey's post test are indicated with a * ($p < 0.05$, $n = 9$).

Figure 3.4A shows the results from the 37°C 50 nm, carboxylated particle transport experiment. After 4 hours Caco-2/HT29-MTX monolayers transported 4.55% of $2x10^{10}$ particles and +M cells monolayers transported 4.60% of the nanoparticles. Figure 3.4B shows results from the 37°C 200 nm particle transport experiments. Caco-2/HT29-MTX monolayers transported 0.42% of $1.25x10^{9}$ 200 nm particles, and +M cell monolayers transported a significantly greater 0.72% of the particles. The results of the *in vitro* digestion/nanoparticle transport experiments are shown in Figure 3.5. Caco-2/HT29-MTX monolayers transported 9.13% of $2x10^{10}$ 50

nm particles in blank digest and 8.96% of $2x10^{10}$ 50 nm particles in rice digest. +M cells monolayers transported 8.96% of the particles in blank digest and 8.88% of the particles in rice digest.

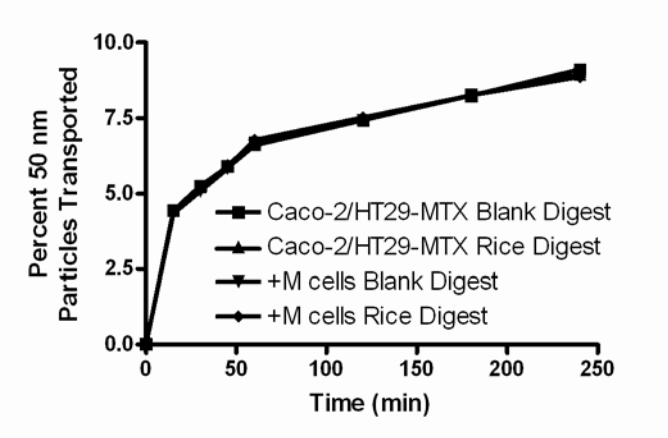

Figure 3.5. Results from digested nanoparticle transport experiments. Caco-2/HT29-MTX cultures transported 9.13% of the 50 nm carboxylated particles in blank digest and 8.96% of particles in rice digest. +M cells cultures transported 8.96% of particles in blank digest and 8.88% of particles in rice digest (n = 3).

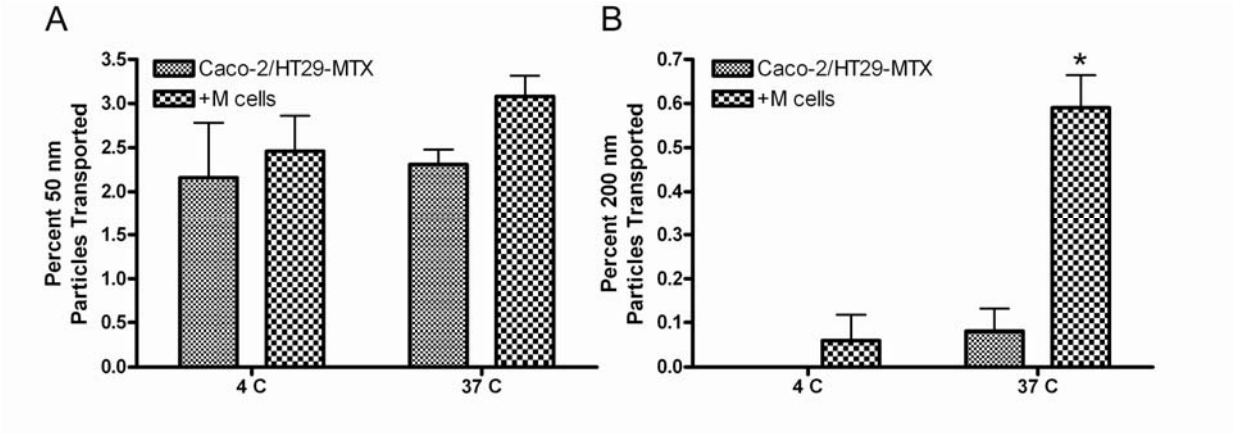

Figure 3.6. Results from 4°C 50 nm and 200 nm particle transport experiments. Error bars show ±SEM. Mean particle transport differences between Caco-2/HT29-MTX monolayers at 4°C and 37°C and +M cells monolayers at 4°C and 37°C that are significant according to a one-way ANOVA with Tukey's post test are indicated with a * ($p < 0.05$, n = 3).

Caco-2/HT29-MTX and +M cells monolayers were exposed to $2x10^{10}$ 50 nm particles or $1.25x10^{9}$ 200 nm particles at 4°C or 37°C. After 45 minutes Caco-2/HT29-MTX cells transported 2.16% of the 50 nm particles at 4°C and 2.31% at 37°C. +M

cells monolayers exposed to 50 nm particles transported 2.46% at 4°C and 3.08% at 37°C (Figure 3.6A). The Caco-2/HT29-MTX cells transported no 200 nm particles at 4°C and 0.08% at 37°C after 45 minutes. +M cells monolayers transported 0.06% of the 200 nm particles at 4°C after 45 minutes and 0.59% at 37°C (Figure 3.6B).

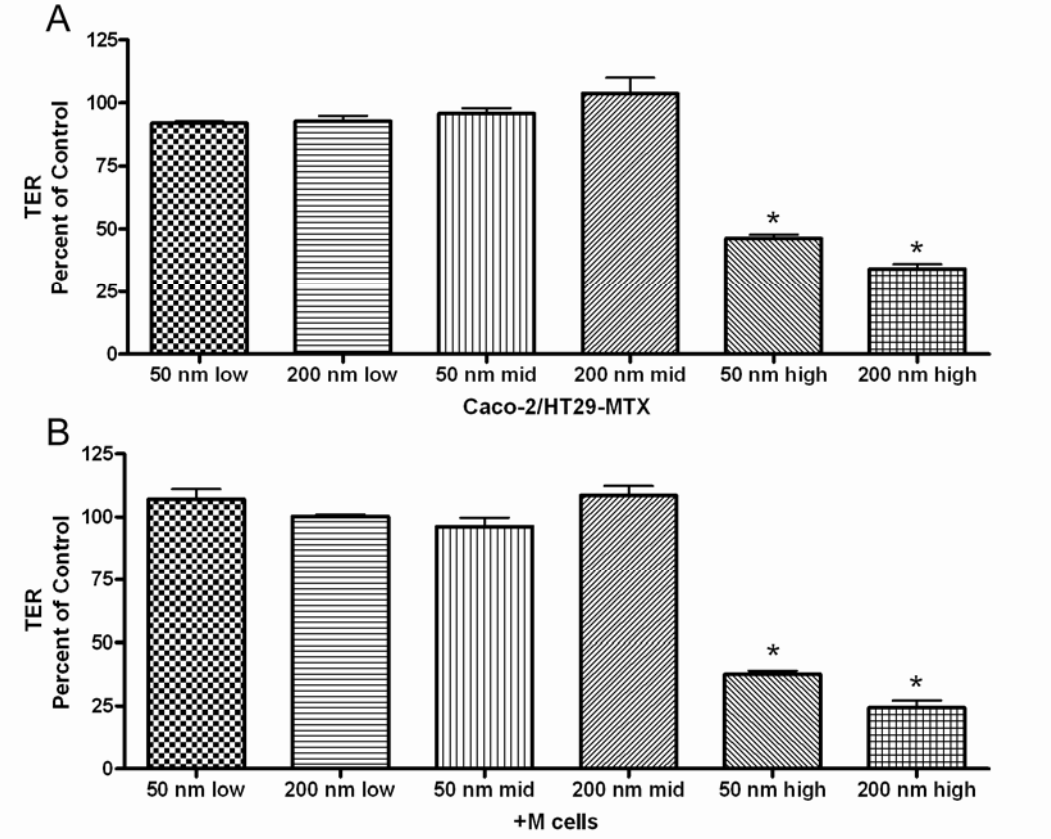

Figure 3.7. TER percent of control for Caco-2/HT29-MTX (A) and +M cells (B) monolayers after a 4 hour exposure to low, mid, or high concentrations of 50 nm or 200 nm carboxylated particles. Controls were Caco-2/HT29-MTX or +M cells monolayers that were not exposed to nanoparticles. Error bars show ±SEM. Differences in TER between +nanoparticle and control monolayers that are significant according to a one-way ANOVA with Tukey's post test are indicated with a * ($p < 0.05$, $n = 9$).

After exposure to low ($2x10^9$ 50 nm particles/mL or $1.25x10^8$ 200 nm particles/mL) or mid ($2x10^{11}$ 50 nm particles/mL or $1.25x10^{10}$ 200 nm particles/mL) concentrations of carboxylated particles in MEM, the TER of the cell monolayers remained intact. For high carboxylated particle concentrations ($2x10^{13}$ 50 nm

particles/mL or $1.25x10^{12}$ 200 nm particles/mL) however, there was a significant decrease in the TER of both Caco-2/HT20-MTX and +M cells monolayers (Figure 3.7). Exposure to mid-level concentrations of non-ionized particles did not affect the Caco-2/HT29-MTX or +M cells monolayer integrity, but aminated particles significantly decreased the TER of Caco-2/HT29-MTX monolayers (Figure 3.8).

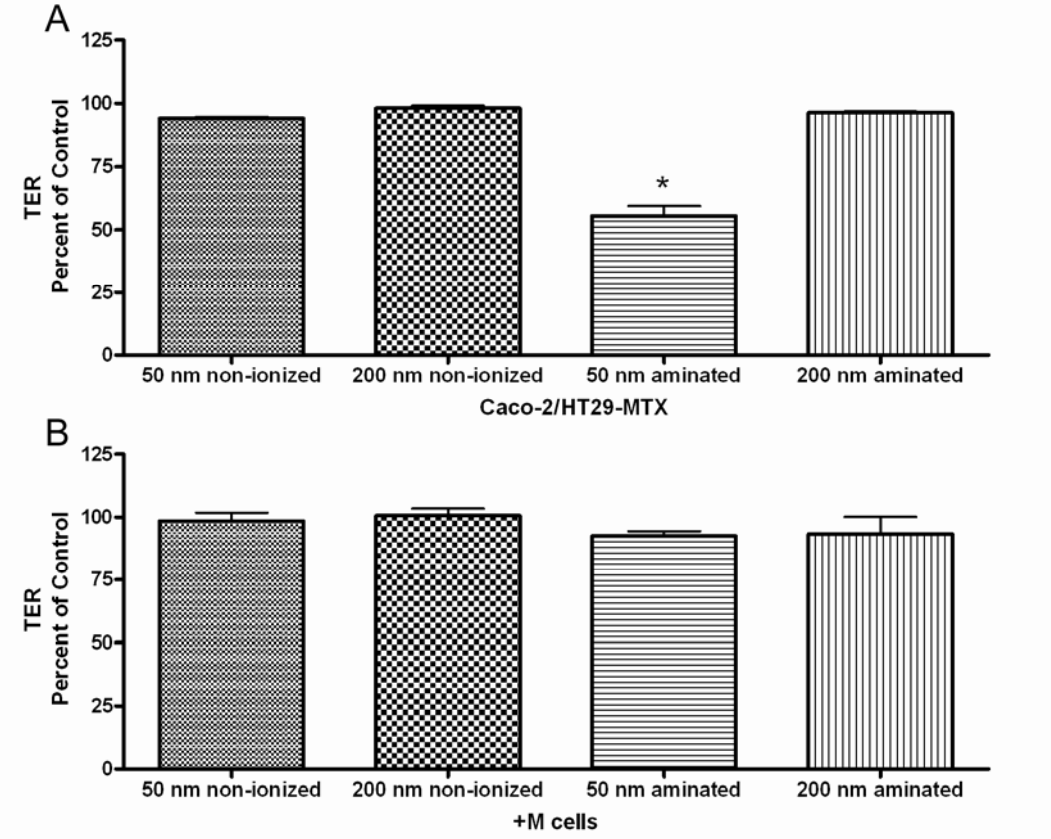

Figure 3.8. TER percent of control for Caco-2/HT29-MTX (A) and +M cells (B) monolayers after a 4 hour exposure to a mid concentration of non-ionized or aminated 50 nm or 200 nm particles. Controls were Caco-2/HT29-MTX or +M cells monolayers that were not exposed to nanoparticles. Error bars show ±SEM. Differences in TER between +nanoparticle and control monolayers that are significant according to a one-way ANOVA with Tukey's post test are indicated with a * ($p < 0.05$, $n = 6$).

3.3.4. Iron uptake and transport after nanoparticle exposure

The results for the iron uptake and transport after a 4 hour exposure to low ($2x10^9$ 50 nm particles/mL or $1.25x10^8$ 200 nm particles/mL), mid ($2x10^{11}$ 50 nm

particles/mL or $1.25x10^{10}$ 200 nm particles/mL) or high ($2x10^{13}$ 50 nm particles/mL or $1.25x10^{12}$ 200 nm particles/mL) concentrations of nanoparticles are shown in Figure 3.9. Iron uptake is quantified by the amount of ^{59}Fe in the cell monolayers and iron transport is the amount of ^{59}Fe that crosses the model epithelium. Controls were corresponding Caco-2/HT29-MTX or +M cells wells that were not exposed to 50 nm or 200 nm particles. Low concentrations of particles had no effect on iron uptake or transport for the Caco-2/HT29-MTX or +M cells monolayers. At mid-level concentrations of particles, iron uptake was not affected for Caco-2/HT29-MTX or +M cell monolayers, but the presence of 50 nm particles in the culture medium resulted in a significant decrease in iron transport for Caco-2/HT29-MTX monolayers. Exposure to mid-level concentrations of 200 nm particles resulted in a significant decrease in iron transport in +M cell monolayers. High 50 nm concentrations significantly increased Caco-2/HT29-MTX and +M cells iron uptake and transport. High 200 nm concentration significantly decreased +M cells iron uptake, and significantly increased iron transport in Caco-2/HT29-MTX and +M cells monolayers.

The effects of nanoparticle charge on iron uptake and transport are shown in Figure 3.10. Mid-level ($2x10^{11}$ 50 nm particles/mL or $1.25x10^{10}$ 200 nm particles/mL) concentrations of particles were used in these experiments. Non-ionized particles had no effect on iron uptake or transport for Caco-2/HT29-MTX or +M cells monolayers. The 50 nm aminated particles significantly increased Caco-2/HT29-MTX and +M cells monolayer iron uptake and Caco-2/HT29-MTX iron transport, while the 200 nm particles did not have any effect on iron uptake and transport.

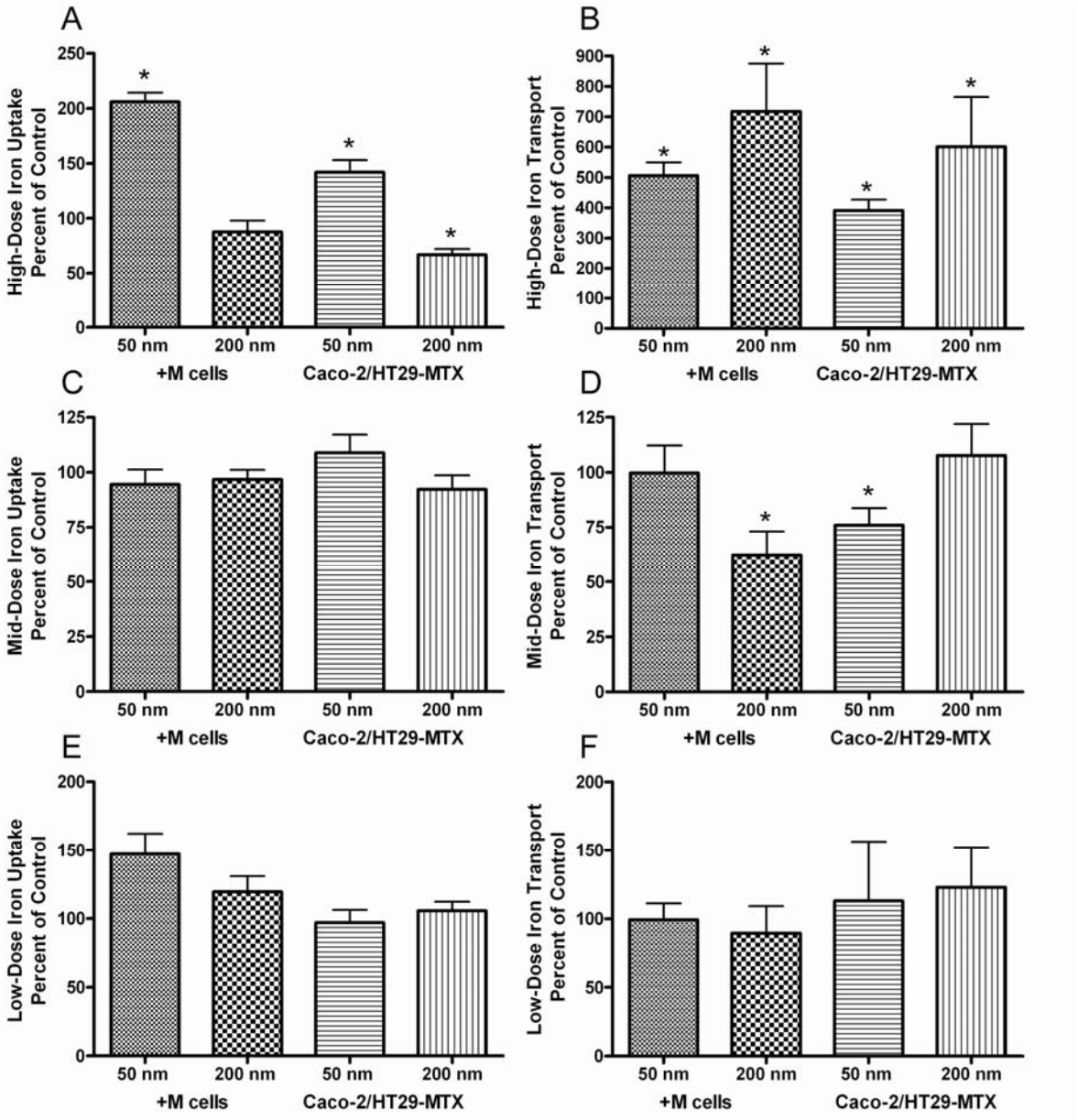

Figure 3.9. Iron uptake after exposure to high (A), mid (C), or low (E) and iron transport after exposure to high (B), mid (D), or low (F) concentrations of 50 nm or 200 nm carboxylated particles. Controls were Caco-2/HT29-MTX or +M cells monolayers that were not exposed to nanoparticles. Error bars show ±SEM. Differences in iron uptake or transport between +nanoparticle and control monolayers that are significant according to a one-way ANOVA with Tukey's post test are indicated with a * ($p < 0.05$, n = 6 for high and low concentrations, n = 9 for mid concentrations).

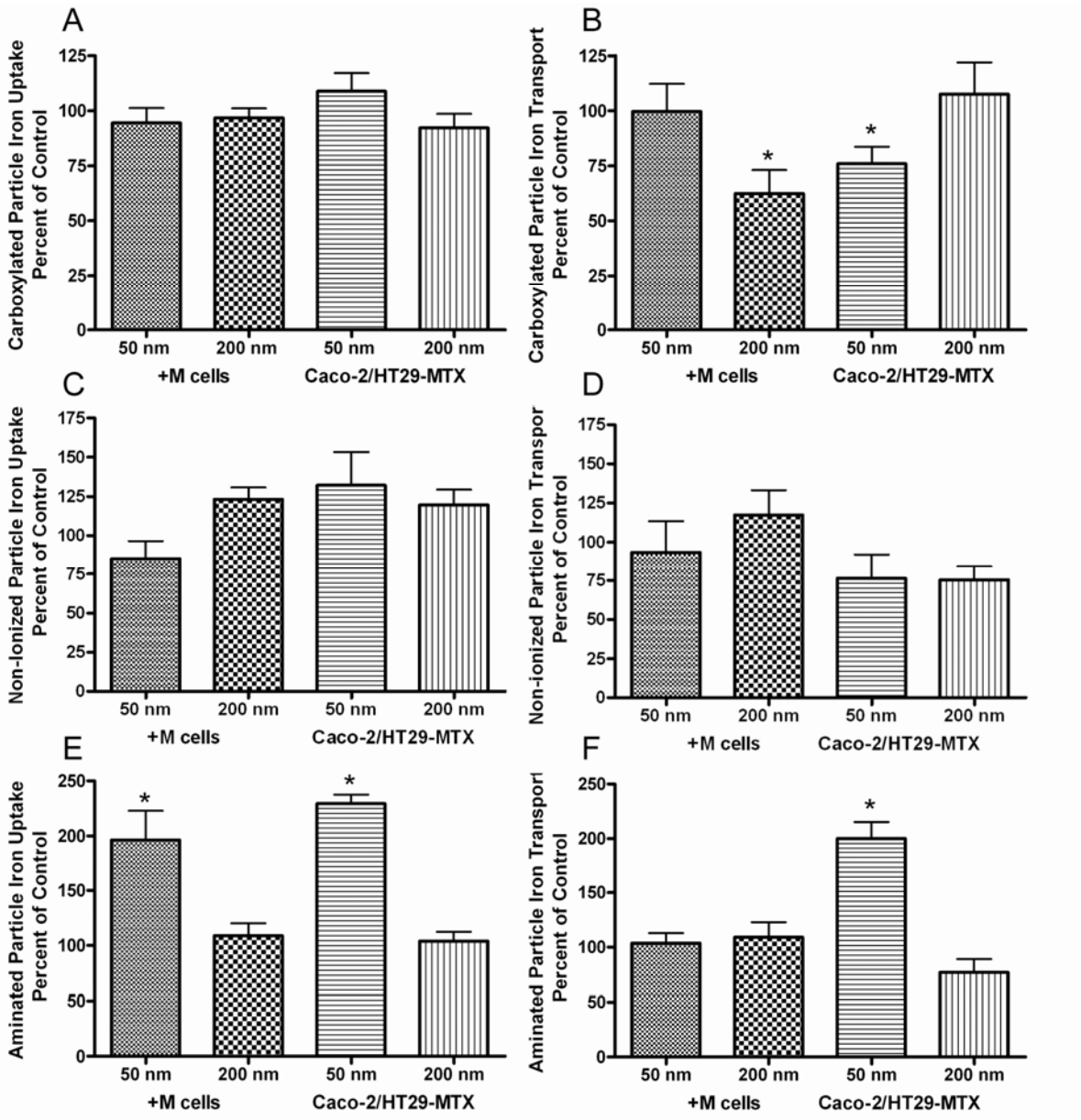

Figure 3.10. Iron uptake after exposure to carboxylated (A), non-ionized (C), or aminated (E) and iron transport after exposure to carboxylated (B), non-ionized (D), or aminated (F) 50 nm or 200 nm particles at a mid concentration. Controls were Caco-2/HT29-MTX or +M cells monolayers that were not exposed to nanoparticles. Error bars show ±SEM. Differences in iron uptake or transport between +nanoparticle and control monolayers that are significant according to a one-way ANOVA with Tukey's post test are indicated with a * ($p < 0.05$, $n = 6$ for aminated and non-ionized, $n = 9$ for carboxylated).

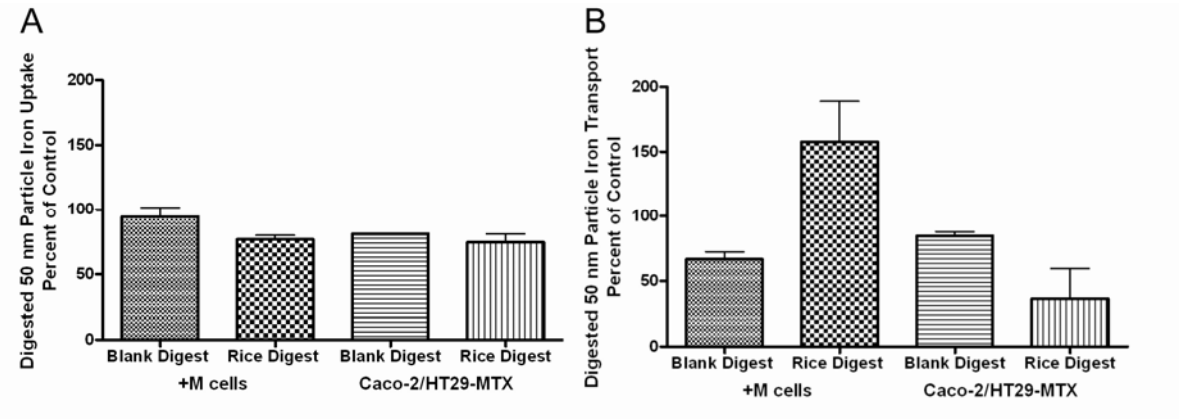

Figure 3.11. Iron uptake (A) and transport (B) for Caco-2/HT29-MTX and +M cells monolayers after exposure to mid concentrations of digested, 50 nm, carboxylated particles.

The results for the iron transport and uptake experiments in blank and rice digest are shown in Figure 3.11. Exposure to 200 nm and 50 nm particles in blank and rice digest did not result in a significant difference in iron uptake or transport for Caco-2/HT29-MTX or +M cells monolayers.

Ferritin levels were analyzed in all samples to exclude preexisting differences in iron status as a cause for differences in iron transport or uptake. Ferritin levels between all +nanoparticle and control cultures were not significantly different ($p < 0.05$).

3.4. Discussion

Previous rat *in vivo* studies on orally administered nanoparticles have found differences in particle uptake and distribution that were most likely due to particle size, shape, surface chemistry and hydrophobicity [24, 25]. Ultrafine ^{192}Iridium and C_{60} fullerene nanoparticles were not significantly absorbed through the rat GI tract [26-28]. Within 48 hours 98% of the water-soluble, ^{14}C-labeled C_{60} fullerenes orally delivered to rats were eliminated in feces; while in the same study 90% of the intravenously administered fullerenes were retained for at least a week, with >70% found in the liver [28]. TiO_2 particles in the 150-500 nm range, however, were

absorbed into the blood stream and found in the liver, spleen, lung, and peritoneal tissue [29]. Pontefract et al. found 0.2-2 μm long asbestos fibers in the air and city drinking water [25]. After finding a 23.55 μm long fiber in a rat's blood stream, Pontefract et al. concluded that smaller fibers pass through the intestinal wall by pinocytosis, while larger fibers pierce the epithelium like a needle [25]. The uptake of orally delivered polystyrene nanoparticles showed a size and surface charge dependent trend. In experiments with non-ionized particles 6.6% of 50 nm particles, 5.8% of 100 nm particles, 0.8% of 1 μm particles, and 0% of 3 μm particles were taken up into the liver, spleen, blood, and bone marrow [30]. Carboxylated polystyrene particles were less well absorbed than non-ionized particles of the same size [31].

A recent study by Chen et al. found copper nanoparticles, but not copper microparticles, to be toxic to mice after oral exposure [32]. Nano and ionic copper particles (25 nm diameter) were class 3 or moderately toxic, and micro-copper particles (17 μm diameter) were class 5 or practically nontoxic on the Hodge and Sterner Scale. The kidney, liver, and spleen were found to be target organs of the copper nanoparticles. Gerhart et al. observed that chronic administration of 125 μm coal particles to fat-head minnows (*Pimephales-promelas*) resulted in increased mucus secretion from goblet cells, which is consistent with the idea that mucus secretion is a mechanism for protecting the intestinal lumen from abrasion [33].

There have been several *in vitro* studies that explored polystyrene nanoparticle uptake and transport through intestinal epithelial models. Behrens et al. studied the effects of a mucus layer on particle transport in Caco-2 and MTX-E12 intestinal cell models [34]. The Caco-2 cells were a model of absorptive enterocytes and the MTX-E12 cell line represented mucus-secreting goblet cells. It was found that the presence of mucus decreased the association of non-ionized, 200 nm polystyrene nanoparticles

with cell cultures by 60%, suggesting that mucus provides a barrier for hydrophobic particle absorption.

des Rieux et al. used an *in vitro* model of Caco-2 monolayers containing M cells to study polystyrene nanoparticle transport [23]. Size and charge were both shown to influence the transport of nanoparticles through monolayers with M cells; the number of 200 nm polystyrene particles transported was significantly higher than the number of 500 nm polystyrene particles transported and cationic groups on the surface of 200 nm polystyrene particles enhanced transport through monolayers with M cells. A later study by des Rieux at al. further characterized the *in vitro* M cell model [35]. In an inverted *in vitro* M cell model (Raji cells were cultured on top of Caco-2 monolayers instead of in the bottom Transwell chamber) it was found that between 15 and 30% of the Caco-2 cells differentiated into M cells. The inverted M cell model transported significantly more 200 nm carboxylated polystyrene particles than the traditional M cell model, and it was determined that the transport of particles occurred by non-specific absorptive endocytosis through a non-clatherin dependent route that was most likely macropinocytosis.

In this study it was shown that there was Caco-2 cell differentiation into cells with an M cell-like morphology as evidenced by increased β1-integrin expression on the apical side of +M cell monolayers. There was no quantitation of the number of M cells in each monolayer, but, in a separate study by des Rieux et al., an inverted *in vitro* M cell model was found to have between 15 and 30% differentiated cells [35]. In the study performed by des Rieux the inverted model transported significantly more 200 nm carboxylated polystyrene particles than the traditionally cultured M cell model, meaning that the traditionally cultured model had fewer differentiated M cells. In the work described in this paper the cells were cultured traditionally and the Caco-2 cells were diluted by HT29-MTX mucus producing cells, most likely resulting in less

than 15% differentiated M cells in the monolayer. Fewer differentiated M cells may be an advantage, however, as the human small intestinal epithelial membrane is composed of less than 10% M cells [36]. This is also the first example to date of an *in vitro* intestinal epithelial model that contains a tri-culture of absorptive, goblet, and M cells.

The transport of 50 nm carboxylated particles through the cell monolayers is predominately a paracellular, non-energy dependent process. This can be observed in the confocal images (Figure 3.2A), where the 50 nm particles were localized to the cell membrane, and by the presence of 50 nm particle transport at 4^{o}C (Figure 3.6A). The +M cells monolayers did not transport a significantly larger number of 50 nm particles, and this is because paracellular transport would not take advantage of the increased transcytosis activity characterized by M cells. +M cell monolayers did transport a significantly greater percent of 200 nm particles when compared with Caco-2/HT29-MTX monolayers, and the M cells most likely transported the particles via macropinocytosis [35]. The confocal images showing 200 nm particles independent of the cell membrane (Figure 3.2B), and the decrease in 200 nm particle transport at 4^{o}C (Figure 3.6B) further indicate that the 200 nm particles are primarily transported via energy-dependent mechanisms as opposed to passive transport through the cell membrane.

Nanoparticles were subjected to a physiologically realistic *in vitro* digestion method and the chyme mimic containing nanoparticles was used for nanoparticle transport and iron uptake and transport studies. The chyme mimic was used for transport and uptake studies to create *in vitro* intestinal epithelial model conditions that better mimic those in the upper small intestine *in vivo*. When the particles were digested before the nanoparticle transport studies, the Caco-2/HT29-MTX and +M cells monolayers transported a great deal more 50 nm particles (~5% in MEM and

~9% after digestion, Figure 3.5). Exposure to digested nanoparticles had no effect of iron uptake or transport, however (Figure 3.11). It has been shown that fewer carboxylated polystyrene particles are absorbed when compared with non-ionized particles [31]. The zeta potential of nanoparticles in blank digest was more negative than in MEM (Table 3.1), therefore the increased particle transport in blank and rice digest was most likely due to cell monolayer damage and weakening of tight junctions by digestive enzymes present in the digest. No further studies were performed with digested nanoparticles because the cell monolayer damage could confound nanoparticle transport and iron uptake and transport studies.

At mid dosages, the presence of 50 nm carboxylated particles resulted in a significant decrease in iron transport for Caco-2/HT29-MTX monolayers (Figure 3.9). Exposure to 200 nm carboxylated particles in culture medium resulted in a significant decrease in iron transport in +M cell monolayers (Figure 3.9). The proteins associated with iron absorption across the apical side of the brush border and exit through the basolateral side of the enterocyte are well characterized, but the mechanism by which iron passes through the cell is poorly understood. Experiments have suggested that there is both vesicular and nonvesicular intracellular iron transport, and that vesicular transport may account for as much as 50% of the transepithelial iron transport [9]. M cells are characterized by increased vesicle transport, and therefore it is likely that iron transport in +M cell cultures is primarily vesicular, or that vesicular iron transport compensates for any nonvesicular iron transport interference in +M cell monolayers exposed to 50 nm particles. Caco-2/HT29-MTX cultures most likely transport iron primarily through nonvesicular mechanisms. Therefore, these iron transport results are consistent with the hypothesis that 50 nm particles are primarily passively transported and interfere with membrane protein associated iron transport while 200 nm particles are transported via vesicles and interfere with vesicular iron transport. The TER and

iron uptake were not affected by the presence of mid level concentrations of nanoparticles for Caco-2/HT29-MTX or +M cell monolayers (Figures 3.7 and 3.9). TER is a measurement of tight junction functionality and iron uptake would be affected if there was damage to the apical cell membrane, therefore the mid dosage of carboxylated nanoparticles did not damage tight junctions or the apical cell membrane.

Low doses of carboxylated 50 nm and 200 nm particles did not have an effect on the TER, iron uptake, or iron transport of Caco-2/HT29-MTX or +M cells monolayers (Figures 3.7 and 3.9). High dosages of carboxylated nanoparticles significantly decreased the TER of Caco-2/HT29-MTX and +M cells monolayers, indicating that the high concentration of carboxylated nanoparticles affected tight junctions (Figure 3.7). The significant increase in iron uptake for Caco-2/HT29-MTX and +M cells monolayers exposed to high concentrations of 50 nm particles suggests apical cell membrane damage from particle exposure (Figure 3.9). The high dose of 200 nm particles did not affect the iron uptake of Caco-2/HT29-MTX monolayers, but did significantly decrease the iron uptake for +M cells monolayers, most likely by overwhelming the cellular vesicular transport pathways normally used for iron transport (Figure 3.9). Iron transport was significantly increased by 50 nm and 200 nm particles in both Caco-2/HT29-MTX and +M cells monolayers. The significant decrease in TER for the cell monolayers exposed to high carboxylated nanoparticle concentrations indicates that the increase in iron transport was due to an increase in paracellular transport because of weakened tight junctions.

Mid doses of non-ionized particles and 200 nm aminated particles had no effect on monolayer TER, iron uptake, or iron transport (Figures 3.8 and 3.10). Mid doses of aminated 50 nm particles significantly decreased the TER, increased the iron uptake, and increased the iron transport of Caco-2/HT29-MTX monolayers, indicating damage to the apical cell membrane and tight junctions of the cell monolayer. The +M

cells monolayers also took up significantly more iron after exposure to 50 nm aminated particles, which indicates apical membrane damage, but TER and iron transport were not affected. Positively charged polymeric nanoparticles have been shown to increase the bioavailability of poorly absorbed compounds when compared with neutral or negatively charged particles [37]. This behavior has been attributed to mucoadhesion mediated by electrostatic interaction between the positively charged polymeric particles and the negatively charged mucin on the epithelial surface [37]. The results found in this paper, however, suggest that the positive charge may also disrupt the apical cell membrane and tight junction integrity.

The intestinal epithelial layer represents the initial gate that nanoparticles must enter to have an acute or chronic toxic effect in the body. The polystyrene particles used in these experiments are generally considered non-toxic, but their interaction with a normal physiological process suggests a potential mechanism for a chronic, harmful, but subtle response. This model provides a new tool to assess nanoparticle toxicity following ingestion, new metrics for measuring sublethal effects, and new data on the relationship between physicochemical properties of nanoparticles and their ability to disrupt cellular behavior. Similar disruptions in nutrient absorption could be possible with other inorganic elements such as calcium, copper, and zinc that require passive or active transport systems to be absorbed through the intestinal epithelium. Fat-soluble vitamins such as vitamins A, D, E, and K are absorbed only after micellization by pancreatic lipase [38]. The micelles, due to their small size and hydrophilic surface, are able to gain proximity to the brush border and facilitate the diffusion of their contents into the phospholipid membrane of the epithelial layer. Hydrophobic, charged nanoparticles could potentially disrupt the formation of micelles, micelle interactions with the epithelial layer, and nutrient diffusion through the phospholipids layer.

In conclusion, this work has used a physiologically realistic, cell culture model of the intestinal epithelium to study the sublethal effects of oral nanoparticle exposure. Iron, which is an essential nutrient that is transported across the intestinal epithelium via complex, highly regulated, protein-assisted vesicular and nonvesicular mechanisms, was chosen as a model compound. These preliminary results suggest that polystyrene nanoparticle size, concentration, and charge can influence iron uptake and transport at doses that represent potential human exposure.

REFERENCES

1. Lee HJ. 2002. Protein drug oral delivery: The recent progress. *Archives of Pharmaceutical Research*. 25(5):572-584.

2. des Rieux A, Fievez V, Garinot M, Schneider YJ, Preat V. 2006. Nanoparticles as potential oral delivery systems of proteins and vaccines: A mechanistic approach. *Journal of Controlled Release*. 116(1):1-27.

3. Galindo-Rodriguez SA, Allemann E, Fessi H, Doelker E. 2005. Polymeric nanoparticles for oral delivery of drugs and vaccines: A critical evaluation of *in vivo* studies. *Critical Reviews in Therapeutic Drug Carrier Systems*. 22(5):419-463.

4. Lomer MCE, Thompson RPH, Powell JJ. 2002. Fine and ultrafine particles of the diet: Influence on the mucosal immune response and association with Crohn's disease. *Proceedings of the Nutrition Society*. 61(1):123-130.

5. Lomer MCE, Hutchinson C, Volkert S, Greenfield SM, Catterall A, Thompson RPH, Powell JJ. 2004. Dietary sources of inorganic microparticles and their intake in healthy subjects and patients with Crohn's disease. *British Journal of Nutrition*. 92(6).

6. Lomer MCE, Grainger SL, Ede R, Catterall AP, Greenfield SM, Cowan RE, Vicary FR, Jenkins AR, Fidler H, Harvey RS and others. 2005. Lack of efficacy of a reduced microparticle diet in a multi-centered trial of patients with active Crohn's disease. *European Journal of Gastroenterology & Hepatology*. 17(3):377-384.

7. Butler M, Boyle J, Powell J, Playford R, Ghosh S. 2007. Dietary microparticles implicated in Crohn’s disease can impair macrophage phagocytic activity and act as adjuvants in the presence of bacterial stimuli. *Inflammation Research*. 56(9):353.

8. Lomer MCE, Kodjabashia K, Hutchinson C, Greenfield SM, Thompson RPH, Powell JJ. 2004. Intake of dietary iron is low in patients with Crohn's disease: A case-control study. *British Journal of Nutrition*. 91(1):141-148.

9. Ma Y, Yeh M, Yeh K-Y, Glass J. 2006. Iron imports. V. Transport of iron through the intestinal epithelium. *American Journal of Physiology-Gastrointestinal and Liver Physiology*. 290(3):G417-G422.

10. Artursson P, Karlsson J. 1991. Correlation between oral drug absorption in humans and apparent drug permeability coefficients in human intestinal epithelial Caco-2 cells. *Biochemical and Biophysical Research Communications*. 175(3):880-885.

11. Artursson P, Palm K, Luthman K. 2001. Caco-2 monolayers in experimental and theoretical predictions of drug transport. *Advanced Drug Delivery Reviews*. 46(1-3):27-43.

12. Han OH, Wessling-Resnick M. 2002. Copper repletion enhances apical iron uptake and transepithelial iron transport by Caco-2 cells. *American Journal of Physiology-Gastrointestinal and Liver Physiology*. 282(3):G527-G533.

13. Halleux C, Schneider Y-J. 1991. Iron absorption by intestinal epithelial cells: 1. Caco-2 cells cultivated in serum-free medium, on polyethyleneterephthalate micropourous membranes, as an *in vitro* model. *In Vitro Cell Developmental Biology*. 27A:293-302.

14. Lesuffleur T, Barbat A, Dussaulx E, Zweibaum A. 1990. Growth adaptation to methotrexate of HT-29 human colon-carcinoma cells is associated with their ability to differentiate into columnar absorptive and mucus-secreting cells. *Cancer Research*. 50(19):6334-6343.

15. Kerneis S, Bogdanova A, Kraehenbuhl JP, Pringault E. 1997. Conversion by Peyer's patch lymphocytes of human enterocytes into M cells that transport bacteria. *Science*. 277(5328):949-952.

16. Gullberg E, Leonard M, Karlsson J, Hopkins AM, Brayden D, Baird AW, Artursson P. 2000. Expression of specific markers and particle transport in a new human intestinal M-cell model. *Biochemical and Biophysical Research Communications*. 279(3):808-813.

17. Glahn RP, Lee OA, Yeung A, Goldman MI, Miller DD. 1998. Caco-2 cell ferritin formation predicts nonradiolabeled food iron availability in an *in vitro* digestion/Caco-2 cell culture model. *Journal of Nutrition*. 128(9):1555-61.

18. Glahn RP, Gangloff MB, Vancampen DR, Miller DD, Wien EM, Norvell WA. 1995. Bathophenanthrolene disulfonic acid and sodium dithionite effectively remove surface-bound iron from Caco-2 cell monolayers. *Journal of Nutrition*. 125(7):1833-1840.

19. DeSesso JM, Jacobson CF. 2001. Anatomical and physiological parameters affecting gastrointestinal absorption in humans and rats. *Food and Chemical Toxicology*. 39(3):209-228.

20. Muir A, Hopfer U. 1985. Regional specificity of iron uptake by small intestinal brush-border membranes from normal and iron-deficient mice. *American Journal of Physiology*. 248(3):G376-G379.

21. Kararli TT. 1995. Comparison of the gastrointestinal anatomy, physiology, and biochemistry of humans and commonly used laboratory animals. *Biopharmaceutics and Drug Disposition*. 16:351-380.

22. Sharp DG, Beard JW. 1950. Size and density of polystyrene particles measured by ultracentrifugation. *Journal of Biological Chemistry*. 185(1):247-253.

23. des Rieux A, Ragnarsson EGE, Gullberg E, Preat V, Schneider YJ, Artursson P. 2005. Transport of nanoparticles across an *in vitro* model of the human intestinal follicle associated epithelium. *European Journal of Pharmaceutical Sciences*. 25(4-5):455-465.

24. Oberdorster G, Oberdorster E, Oberdorster J. 2005. Nanotoxicology: An emerging discipline evolving from studies of ultrafine particles. *Environmental Health Perspective*. 113(7):823-839.

25. Pontefra RD, Cunningham HM. 1973. Penetration of asbestos through digestive tract of rats. *Nature*. 243(5406):352-353.

26. Kreyling WG, Semmler M, Erbe F, Mayer P, Takenaka S, Schulz H, Oberdorster G, Ziesenis A. 2002. Translocation of ultrafine insoluble iridium particles from lung epithelium to extrapulmonary organs is size dependent but very low. *Journal of Toxicology and Environmental Health, Part A: Current Issues*. 65(20):1513-30.

27. Semmler M, Seitz J, Erbe F, Mayer P, Heyder J, Oberdorster G, Kreyling WG. 2004. Long-term clearance kinetics of inhaled ultrafine insoluble iridium particles from the rat lung, including transient translocation into secondary organs. *Inhalation Toxicology*.16(6-7):453-459.

28. Yamago S, Tokuyama H, Nakamura E, Kikuchi K, Kananishi S, Sueki K, Nakahara H, Enomoto S, Ambe F. 1995. *In vivo* biological behavior or a water-miscible fullerene: ^{14}C labeling, absorption, distribution, excretion and acute toxicity. *Chemistry & Biology*. 2(6):385-389.

29. Jani PU, McCarthy DE, Florence AT. 1994. Titanium-dioxide (rutile) particle uptake from the rat GI tract and translocation to systemic organs after oral-administration. *International Journal of Pharmaceutics*. 105(2):157-168.

30. Jani P, Halbert GW, Langridge J, Florence AT. 1990. Nanoparticle uptake by the rat gastrointestinal mucosa: Quantitation and particle size dependency. *Journal of Pharmacy and Pharmacology*. 42(12).

31. Jani P, Halbert GW, Langridge J, Florence AT. 1989. The uptake and translocation of latex nanospheres and microspheres after oral-administration to rats. *Journal of Pharmacy and Pharmacology*. 41(12):809.

32. Chen Z, Meng HA, Xing GM, Chen CY, Zhao YL, Jia GA, Wang TC, Yuan H, Ye C, Zhao F and others. 2006. Acute toxicological effects of copper nanoparticles *in vivo*. *Toxicology Letters*. 163(2):109-120.

33. Gerhart EH, Liukkonen RJ, Carlson RM, Stokes GN, Lukasewycz M, Oyler AR. 1981. Histological effects and bioaccumulation potential of coal particulate-bound phenanthrene in the fathead minnow *pimephales-promelas*. *Environmental Pollution Series A-Ecological and Biological*. 25(3):165-180.

34. Behrens I, Pena AIV, Alonso MJ, Kissel T. 2002. Comparative uptake studies of bioadhesive and non-bioadhesive nanoparticles in human intestinal cell lines and rats: The effect of mucus on particle adsorption and transport. *Pharmaceutical Research*. 19(8):1185-1193.

35. des Rieux A, Fievez V, Theate I, Mast J, Preat V, Schneider YJ. 2007. An improved *in vitro* model of human intestinal follicle-associated epithelium to study nanoparticle transport by M cells. *European Journal of Pharmaceutical Sciences*. 30(5):380-391.

36. Owen RL, Ermak TH. 1990. Structural specializations for antigen uptake and processing in the digestive-tract. *Springer Seminars in Immunopathology*. 12(2-3):139-152.

37. El-Shabouri MH. 2002. Positively charged nanoparticles for improving the oral bioavailability of cyclosporin-A. *International Journal of Pharmaceutics*. 249(1-2):101-108.

38. Basu TK, Donaldson D. 2003. Intestinal absorption in health and disease: Micronutrients. *Best Practice & Research Clinical Gastroenterology*. 17(6):957-79.

CHAPTER 4

DEVELOPMENT OF A GASTROINTESTINAL TRACT MICROSCALE CELL CULTURE ANALOG TO PREDICT DRUG TRANSPORT

4.1. Introduction

The cost of developing a new drug was recently estimated to be 1.9 billion dollars [1]. With the majority of drug candidates failing in expensive phase III clinical trials, there is a significant economic need for a method that accurately assesses the ADMET (absorption, distribution, metabolism, elimination, and toxicity) of drug candidates early in the development process [2]. *In vitro* cell cultures and animal models are the two most common methods used to determine toxicological and pharmacological profiles of potential drugs, but both methods have disadvantages. The largest problem with single cell type, monolayer cell cultures is that the effects of drug metabolites and systemic changes caused by the compound of interest cannot be studied [3]. Animal experiments can take months to complete, cost millions of dollars, and the majority of drugs shown to be safe in animals fail in human clinical trials [3].

This work describes an *in vitro* system that may be able to better predict animal or human response to oral drug exposure. A cell culture analog (CCA) can be defined as a physical representation of a physiologically based pharmacokinetic (PBPK) model. A PBPK mathematical model describes an organism as a set of interconnected compartments that is based on vasculature structure, and is designed to describe the time-dependent distribution of a chemical or drug in various tissues [4]. The CCA devices consist of channels and chambers arranged and sized to mimic the residence time and flow distribution of the corresponding PBPK model. In addition,

where the PBPK model mathematically specifies an organ or tissue compartment, the CCA has an actual chamber holding a cell type that mimics the organ or tissue. Re-circulating culture medium represents the circulatory system. The goal of a CCA is to create an *in vitro* system that can replicate some of the cell-cell interactions (i.e. interactions through soluble proteins and metabolites) in humans or animals not easily studied *in vivo* or *in silico* and to apply these observations to toxicology studies.

A three-chamber (lung, liver, and other tissues) microscale cell culture analog (μCCA) has been developed using tools from the semiconductor industry [5]. The μCCA consists of etched cell compartments connected by channels on a 2.5 cm x 2.5 cm silicon chip, with culture medium re-circulated through the chip using a peristaltic pump. A four-chamber (lung, liver, fat, and other tissues) μCCA was used to demonstrate the effects of naphthalene on various tissues [6]. Two chambers (lung and liver) contained living cells; the other tissue and fat compartments had no cells, but mimicked the distribution of fluid in rapidly and slowly perfused tissues. Naphthalene added to the circulating culture medium was converted to reactive metabolites in the liver compartment. When these metabolites circulated to the lung compartment the concentration of glutathione, a protective compound, was reduced in the lung cells, resulting in lung cell death. In control experiments without liver cells, however, there was no lung cell death. Later experiments using adipocyte-like cells in the fat chamber showed how fat could modify the response [7]. These experiments show that the system can re-create the known effects of a toxic chemical. The microscale size of the device allows for near *in vivo* organ residence times, fluid to tissue ratios, and cellular shear stress values. The small size also decreases manufacturing costs, reagent amounts, and space needed.

In the proof of concept, four-chamber chip, test chemicals were added directly to the circulating culture medium, which mimics intravenous administration of a

compound. The purpose of this work is to connect an independent gastrointestinal (GI) tract μCCA to a multichamber "body" chip μCCA, which may provide a superior *in vitro* method for testing the ADMET of orally administered pharmaceuticals. The GI tract μCCA consists of two chambers mounted on top of each other and separated by a microporous membrane, on which intestinal epithelial cells are cultured. The top or apical chamber represents the intestinal lumen, and the bottom or basolateral chamber represents the capillary network surrounding the intestinal tract. The separate GI tract unit will be referred to as the GI tract μCCA, the silicon "body" chip will be referred to as the chip μCCA, and the connected GI tract and chip μCCAs will be referred to as the μCCA system.

Acetaminophen (APAP) was chosen as a model drug for this work. APAP toxicity is closely linked to GI and liver cell metabolism of the drug. Therapeutic doses are primarily metabolized by phase II conjugation with sulfate and glucuronide [8]. Approximately 5-10% of a therapeutic APAP dose is oxidized by cytochrome P450 (CYP) 1A2, 2E1, or 3A4 to N-acetyl-*p*-benzoquinone (NAPQI), a toxic, electrophilic metabolite [9, 10]. NAPQI is detoxified by conjugation with glutathione via glutathione-S-transferase and excreted in urine or bile [11]. Large doses of APAP that overwhelm the sulfation and glucuronidation pathways or the induction of CYP enzymes with drugs such as ethanol can result in high levels of NAPQI [8]. High levels of NAPQI cause glutathione depletion and eventual NAPQI accumulation; NAPQI electrophilically attacks proteins in nearby cells and causes cell death [12]. Figure 4.1 illustrates the acetaminophen metabolism pathways.

In these proof of concept experiments, APAP was used to test the hypothesis that drug passes through the intestinal epithelial monolayer in the GI tract μCCA, circulates to the liver and other cell type compartments on the chip μCCA, and causes glutathione depletion and cell death. In the first generation μCCA system experiments,

a four-compartment model was used where lung, liver, and other tissues compartments were etched into the silicon chip μCCAs and the GI tract μCCAs were separate devices fabricated from plexiglass. Three of the chambers (lung, liver, and GI) contained cells, while the other tissues compartment mimicked the distribution of fluid in slowly perfused tissues. The GI tract and chip μCCAs were later revised, and in the second generation μCCA system experiments a five-compartment model was used. Liver, kidney, fat and bone marrow compartments were etched into silicon chip μCCAs, and the GI tract μCCAs were separate devices fabricated from plexiglass. Two of the chambers (liver and GI) contained cells, while the other compartments mimicked the distribution of fluid in well perfused or poorly perfused tissues.

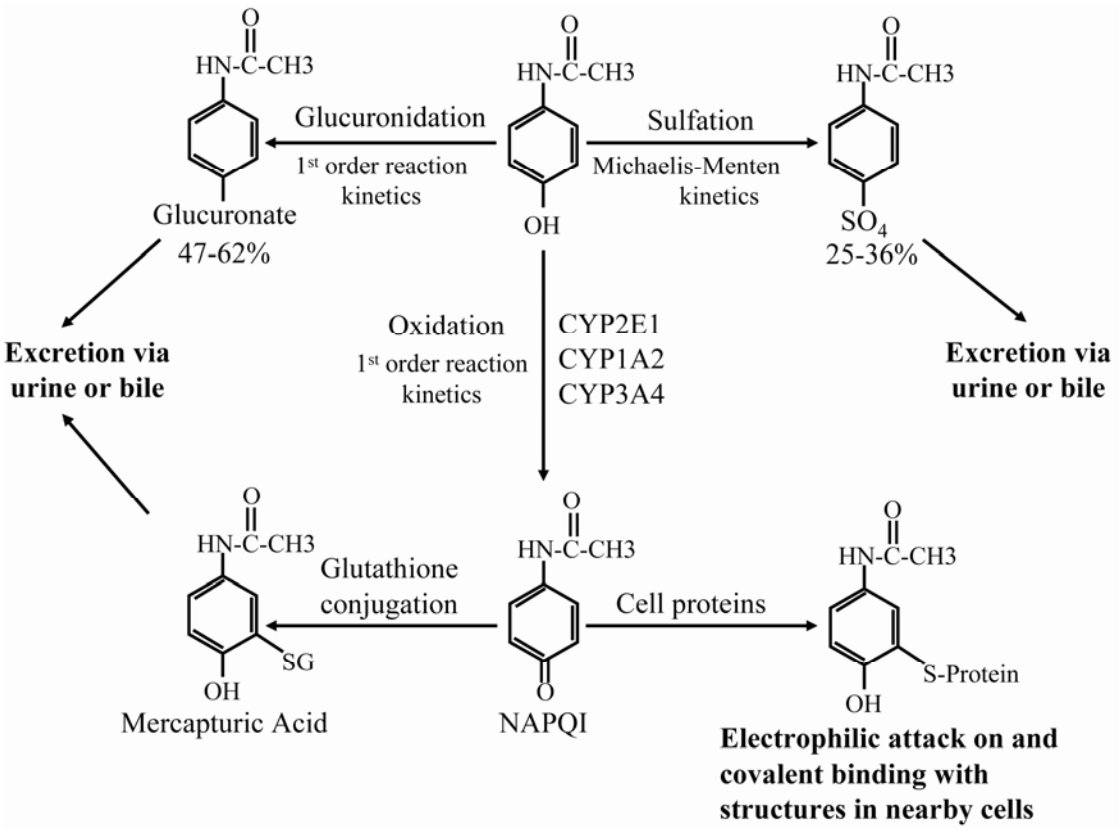

Figure 4.1. Common pathways of acetaminophen metabolism [8, 13].

4.2. Materials and methods

4.2.1. Materials

Dulbecco's Modified Eagle Medium (DMEM), Minimum Essential Medium (MEM), Dulbecco's Modified Eagle Medium:Nutrient Mix F-12 (DMEM/F12, 1:1), fetal bovine serum (FBS), heat inactivated FBS, trypsin-EDTA (0.25%), phosphate buffered saline (PBS), calcein, and monochlorobimane (MCB) were obtained from Invitrogen (Grand Island, NY). Polycarbonate, 0.4 μm pore size membranes were obtained from Whatman Inc. (Florham Park, New Jersey). Polycarbonate, 0.4 mm pore size, 12 mm diameter Snapwell^{TM} inserts and clear, 96-well and 6-well assay plates were purchased from Corning Life Sciences (Corning, NY). Membranes were coated with Type I collagen from Becton Dickinson (Bedford, MA). Human plasma fibronectin was acquired from Millipore (Billerica, MA). β-glucuronidase/arylsufatase was purchased from Roche Applied Science (Indianapolis, IN). Silicone wafers were purchased from Silicon Quest (Santa Clara, CA). P20 primer and Shipley 1813 and 1027 photoresist were purchased from Shipley Company (Marlborough, MA). MIF 300 developer was obtained from Claricut (Somerville, NY). Unless otherwise stated, all other chemicals were purchased from Sigma Aldrich (St. Louis, MO).

4.2.2. Cell culture

The Caco-2 (human colon carcinoma), HepG2/C3A (human hepatocellular carcinoma) and L2 (rat lung) cell lines were obtained from the American Type Culture Collection (Manassas, VA). The HT29-MTX cell line was kindly provided by Dr. Thécla Lesuffleur of INSERM U560 in Lille, France at passage 11 and used in experiments at passage 14-19 [14]. Caco-2 cells were received at passage 17 and used in experiments at passage 30-35. Caco-2 and HT29-MTX were grown in DMEM containing 4 mM Glutamax, 4.5 g/L glucose, and 10% heat inactivated FBS.

HepG2/C3A cells were received at an unknown passage and used in experiments at passage n+10-n+20. HepG2/C3A cells were maintained in MEM with 1.0 mM sodium pyruvate and 10% FBS. L2 cells were cultured in DMEM/F12 with 10% FBS.

4.2.3. TER measurements

Transepithelial resistance (TER) of the cell monolayers in Snapwell inserts was measured every three days after seeding to assess the confluency of the monolayers and tight junction functionality. TER measurements were made using the Millicell ERS from Millipore (Billerica, MA) with the Endohm-24 SNAP chamber from World Precision Instruments (Sarasota, FL). The chamber was sterilized prior to use with 70% ethanol for 15 minutes. After the chamber was equilibrated with 2 mL of PBS for 2 hours at room temperature, the Millicell ERS voltage was adjusted to a zero reading and the PBS was replaced with 600 μL of serum free DMEM. Culture plates were removed from the incubator 5 minutes prior to measurements to allow the culture medium to come to room temperature. Three measurements at different membrane insert positions were taken per sample. Membranes with TER values between 200 and 300 Ω/cm^2 were used in second generation μCCA APAP toxicity experiments.

4.2.4. Cytochrome P450 1A and 2E1 measurement

CYP1A activity was measured using the method described by Donato et al. [15]. HepG2/C3A cells were seeded at 250,000 cells/cm^2 in clear 96 well plates coated with 8 μg/cm2 fibronectin and grown for 48 hours. Caco-2 cells were seeded at 100,000 cells/cm^2 in clear 96 well plates coated with 8 μg/cm^2 Type I collagen and grown for 16 days. Cells were then washed twice with PBS and 100 μL of assay medium, which consisted of phenol red-free DMEM/F12 containing 8 μM ethoxyresorufin and 10 μM dicumerol, was added to each well. After a 1 hour

incubation at 37°C and 5% CO_2, 75 μL of assay medium was taken from each well and transferred to a separate 96 well plate; subsequently 15 Fisherman units of β-glucuronidase and 120 Roy units of arylsulfatase in 25 μL in 0.1 M sodium acetate buffer (pH 4.5) were added to each well containing 75 μL assay medium. The 96 well plates were then incubated at 37°C for 2 hours, 200 μL of ethanol was added to each well, and the plates were centrifuged at 3000 rpm for 10 minutes. The amount of resorufin formed and released into the culture medium was quantified at 530 nm excitation and 590 nm emission by a SpectraMax Gemini EM fluorescence microplate reader from Molecular Devices (Sunnyvale, CA). A standard curve for resorufin was prepared in phenol red free DMEM/F12 and processed in the same manner as samples.

CYP2E1 activity was assessed using the methods described by Donato et al. and Dicker et al. [16, 17]. HepG2/C3A cells were seeded at 250,000 cells/cm^2 in clear 96 well plates coated with 8 μg/cm^2 fibronectin and grown for 48 hours. Caco-2 cells were seeded at 100,000 cells/cm^2 in clear 96 well plates coated with 8 μg/cm^2 Type I collagen and grown for 16 days. Cells were then washed twice with PBS and 100 μL of assay medium, which consisted of phenol red-free DMEM/F12 containing 500 μM p-nitrophenol, was added to each well. After a 1 hour incubation at 37°C and 5% CO_2, 75 μL of assay medium was taken from each well and transferred to a separate 96 well plate. 15 Fisherman units of β-glucuronidase and 120 Roy units of arylsulfatase in 25 μL in 0.1 M sodium acetate buffer (pH 4.5) were added to each well containing 75 μL assay medium. The 96 well plates were incubated at 37°C for 2 hours and then 10 μL of 10 M NaOH was added to each well. The amount of p-nitrophenol hydroxylation to p-nitrocatechol was quantified by measuring the sample absorbance at 546 nm with a VersaMax™ microplate reader (Molecular Devices). A standard curve for p-nitrocatechol was prepared in phenol red free DMEM/F12 and processed in the same manner as samples.

Following the CYP1A and CYP2E1 assays the total cell protein was measured using the Bradford method described by Kautzky et al. [18, 19]. The remaining 25 μL of assay medium was removed from the cells and the monolayers were washed twice with PBS. The cells were then lysed by adding 50 μL of 0.1 M NaOH to each well and incubating for 15 minutes at 37^{o}C. After lysing the cells, 200 μL of Bradford reagent was added to each well and absorbance was read at 595 nm with a microplate reader. Dilutions of 0 to 1 mg/mL bovine serum albumin (BSA) dissolved in 0.1 M NaOH were used as protein standards.

4.2.5. μCCA fabrication

4.2.5.1. First generation μCCA fabrication

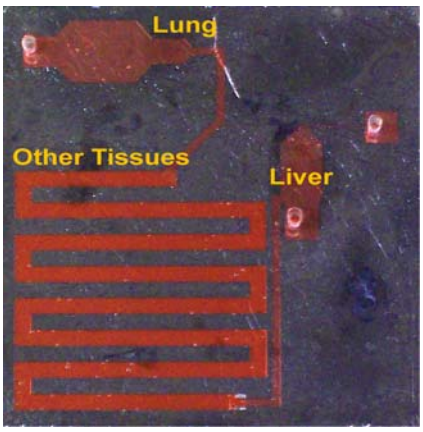

Figure 4.2. A photograph of the first generation chip μCCA. The dimensions of the chambers are as follows (w x l x d): lung (2 mm x 1.6 mm x 40 μm), liver (2 mm x 6 mm x 40 μm), and other tissues (1 mm x 123 mm x 100 μm). The channels connecting compartments were 100 μm deep. The chip was designed so 85% and 15% of the medium leaving the lung compartment goes to the other tissues and liver chambers, respectively, while 100% of medium leaving the basolateral GI tract μCCA chamber goes to the liver.

The chip was fabricated at the Cornell Nanofabrication Facility (CNF) using standard photolithography and etching techniques that have been described previously [5]. The chip pattern was first designed on CAD (Cadence, Fishkill, NY). The pattern was then converted onto a chrome-coated glass mask via the 3600F optical pattern

generator (D.W. Mann/GCA Corp., USA). Two masks were required for the two layers of fabrication, a 40 μm etch and a 100 μm etch.

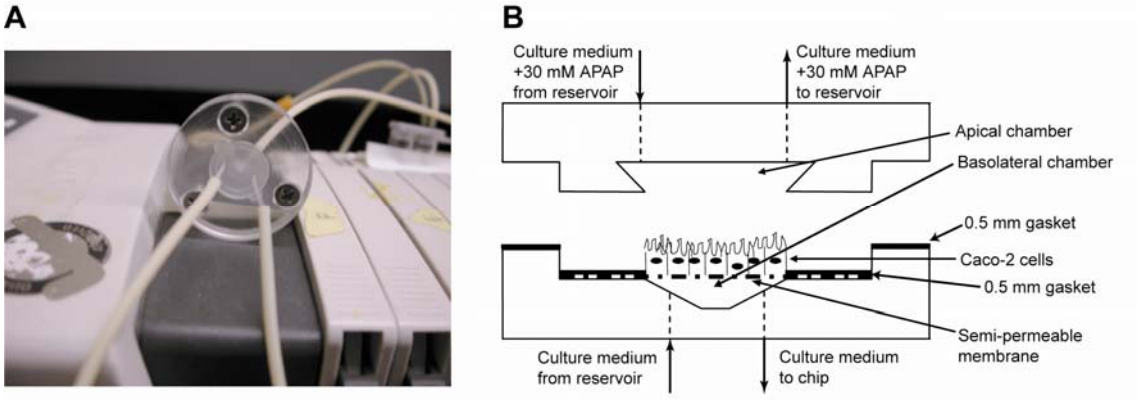

Figure 4.3. (A) Photograph of the apical side of the first generation GI tract μCCA. (B) A side-view schematic of the GI tract μCCA. The dimensions of the apical and basolateral chambers are as follows (diameter of the top of the chamber x height x diameter of the bottom of the chamber): apical chamber (8 mm x 0.8 mm x 2.8 mm) and basolateral chamber (2.8 mm x 0.8 mm x 0.8 mm). The total area of Caco-2 cells exposed to flow was 6.2 mm^2.

A 4.00 inch diameter, 525 μm thick, <100>, silicon wafer was primed with P20 primer at 3000 rpm for 30 seconds. Next, the wafer was coated with 1.3 μm of Shipley 1813 photoresist at 3000 rpm. The first mask pattern was transferred to the wafer with UV light (405 nm) for 2.5 seconds using an AB-M HTG 3HR Contact Proximity Aligner (San Jose, CA). The wafer was then developed for 1 minute in MIF 300 developer, rinsed in DI water, and dried. A deep reactive ion etch (DRIE) process with the UNAXIS 770 plasma etcher (Unaxis USA Inc., St. Petersburg, FL) was used to etch the wafer at a rate of approximately 2 μm/min to a depth of 40 μm.

For the second layer of fabrication the wafer was once again primed with P20 primer before Shipley 1075 photoresist was spun on the wafer at 2000 rpm for 30 seconds. The second mask pattern was transferred to the wafer with UV light for 30 seconds using the HTG contact aligner. The wafer was again developed and etched with the UNAXIS 770 to a depth of 100 μm. Finally, the wafer was stripped using a heated resist bath and the individual chips (7 per wafer) were separated by scoring

with a diamond blade and breaking the wafer. Figure 4.2 is a photograph of the chip μCCA used for these experiments.

The first generation GI tract μCCA was fabricated from ½" thick plexiglass (McMaster-Carr, New Brunswick, NJ) by Glenn Swann (School of Chemical and Biomolecular Engineering, Cornell University). A photograph and side-view schematic of the first generation GI tract μCCA are shown in Figure 4.3. The plastic was etched so that the top piece contained a chamber that was 8 mm at the top (surface where the fluid inlet and outlet are located), 0.8 mm high, and 2.8 mm at the bottom (the surface that comes in contact with the cell monolayer). The bottom piece had an etched chamber that was 0.8 mm at the bottom (surface where the fluid inlet and outlet are located), 0.8 mm high, and 2.8 mm at the top (the surface that comes in contact with the cell monolayer). The top and bottom pieces had two-step inlet and outlet channels drilled with a diameter of 740 μm (drill size number 69, Small Parts Inc., Miami Lakes, FL) for the top half of the channel and 610 μm (drill size number 73, Small Parts) for the bottom half of the channel.

4.2.5.2. Second generation μCCA fabrication

The chip pattern was first designed on CAD (Cadence), and the pattern was converted onto a chrome-coated glass mask via the 3600F optical pattern generator (D.W. Mann/GCA Corp.). Two masks were required for the two layers of fabrication, a 30 μm etch and a 100 μm etch.

In a furnace tube, silicon dioxide layers (93 nm thick) were grown on silicon <100> wafers at 1100^{o}C under 8 L/min O_2 flow and 0.24 L/min HCl flow. The wafers were covered with Shipley 1813 photoresist at a spin speed of 3000 rpm resulting in a 1.3 μm-thick layer of photoresist. The pattern was transferred to the resist via a 4 second UV light (405nm) exposure on an HTG contact aligner contact and subsequent

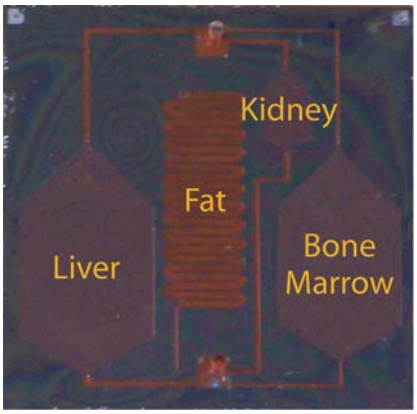

Figure 4.4. Photograph of the second generation chip μCCA. The dimensions of the chambers are as follows (w x l x d): liver (8.5 mm x 8.25 mm x 30 μm), fat (0.5 mm x 115 mm x 100 μm), kidney (3.1 mm x 3.1 mm x 30 μm), and bone marrow (7.5 mm x 7.5 mm x 30 μm). The channels connecting compartments were 100 μm deep. The chip was designed so 41% of the flow went to the liver chamber, 35% went to the kidney chamber, 17% went to the bone marrow chamber, and 7% went to the fat chamber. The other poorly and well perfused tissues were represented by the external debubbler, which was a 200 μL well.

development for 2 minutes. Residual resist was removed using oxygen plasma for 30 seconds and the silicon dioxide layer was etched using a CHF_3/O_2 plasma for 15 minutes at 40 mTorr, 50 sccm CHF_3, 2 sccm O_2, and 40% RF power. The channels were then etched with a DRIE process with the UNAXIS 770 until the depth measured 30 μm. The resist and oxide were removed using resist remover 1165 and Buffered Oxide Etch 6:1 for 5 minutes, respectively. New silicon dioxide layers were grown using dry oxidation as described above. The wafers were then coated with Shipley STR 1045 photoresist at 1000 rpm and baked at 95^{o}C, ramped up stepwise from 25^{o}C in 8 minutes. The resist thickness was relatively non-uniform owing to the already etched channels, but in general measured between 10-12 μm. The second mask pattern was transferred to the wafer with UV light for 20 seconds using the HTG contact aligner ad developed for 6 minutes. Residual resist was removed using the same parameters described above. The second set of channels was etched using the DRIE process until the etch depth measured 100 μm. The resist was stripped with 1165 and

the channel depth checked again. If needed, the channels were etched for one or two more cycles to obtain an exact etch depth. The oxide layer served as an additional masking layer, since the resist is non-uniform and measurement of the etch depth with resist may vary on the position of measurement. Figure 4.4 shows a photograph of the second generation chip μCCA.

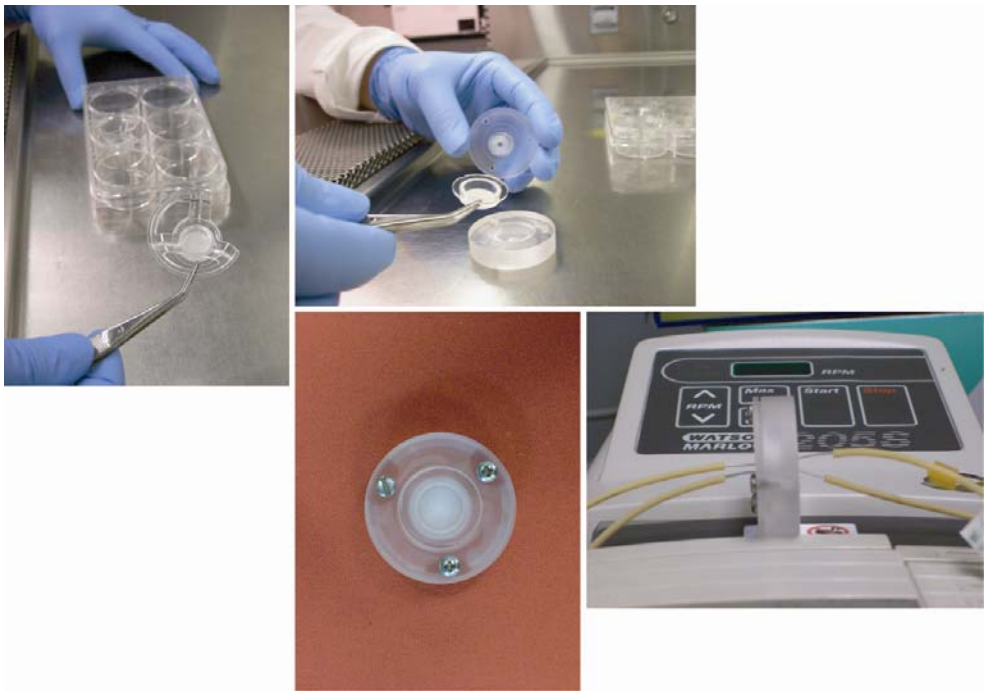

Figure 4.5. Second generation GI tract μCCA device and assembly. The dimensions of the apical and basolateral chambers are as follows (diameter of the top of the chamber x height x diameter of the bottom of the chamber): apical chamber (0.8 mm x 0.8 mm x 2.8 mm) and basolateral chamber (2.8 mm x 0.8 mm x 0.8 mm). The total area of Caco-2/HT29-MTX cells exposed to flow was 6.2 mm^2.

The second generation GI tract μCCA was also fabricated from ½" thick plexiglass (McMaster-Carr) by Glenn Swann (School of Chemical and Biomolecular Engineering, Cornell University). The top and bottom pieces were machined to fit a 12 mm diameter Snapwell insert. Identical chambers were etched into the top and bottom pieces on the surface that contacted the membrane holding intestinal epithelial cells.

The chambers were 0.8 mm deep, 2.4 mm in diameter on the side facing the cell membrane, and 0.8 mm in diameter where the inlet and out let holes were drilled. The top and bottom pieces had two-step inlet and outlet channels drilled with a diameter of 740 μm (drill size number 69, Small Parts) for the top half of the channel and 610 μm (drill size number 73, Small Parts) for the bottom half of the channel. Figure 4.5 shows the second generation GI tract μCCA assembly.

4.2.6. μCCA toxicity experiments

4.2.6.1. First generation μCCA toxicity experiments

The bottom chambers of the GI tract μCCAs were first sterilized by soaking for 30 minutes in 70% EtOH and then placed in a 6-well plate. Polycarbonate, 0.4 μm pore size membranes were cut to 12 mm in diameter, sterilized by autoclaving in a dry cycle for 30 minutes, and placed in the bottom chamber. A sterile, 12 mm outer diameter (OD), 10 mm inner diameter (ID), 0.5 mm thick, silicone gasket was placed over the membrane (Grace Bio-Labs, Bend, OR, gasket was cut to the correct size from a silicone sheet). The membrane and gasket were held in place with a 12 mm OD, 10 mm inner diameter (ID) sterile washer. The membranes were coated with 8 $\mu g/cm^2$ Type I collagen dissolved in 0.02 M acetic acid for 1 hour and then washed with the same volume of PBS. Caco-2 cells were seeded onto the membranes at a concentration of 100,000 cells/cm^2, allowed to attach for 2 hours at 37^oC and 5% CO_2, and then each well of the 6-well plate was filled with 3 mL DMEM. Caco-2 cells were grown on the membrane for 16 days prior to experiments to allow for full coverage of the membrane and cell differentiation.

μCCA chips were cleaned with a solution of 70% sulfuric acid and 30% hydrogen peroxide (30% H_2O_2 solution) for 10 minutes at room temperature and then rinsed with DI water. After cleaning, 1 mm thick silicone gaskets (Grace Bio-Labs)

with holes cut out over the cell chambers were placed onto the chips to keep coating and cell suspensions within the proper compartments. The chips with gaskets over then were dried in an oven at 60^{o}C for 30 minutes to seal the two together, and then both were autoclaved in a dry cycle for 30 minutes.

The μCCA chips were first coated with 4 μg/cm^2 poly-D-lysine in PBS for 5 minutes at room temperature. The poly-D-lysine solution was removed from each chamber and each chamber was washed with an equal volume of PBS. The chips were then coated with 8 μg/cm^2 fibronectin in PBS for 1 hour at room temperature. The fibronectin solution was removed, L2 cells were seeded into the lung chamber at a concentration of 200,000 cells/cm^2, and HepG2/C3A cells were seeded into the liver chamber at a concentration of 250,000 cells/cm^2. The chips were kept at 37^{o}C and 5% CO_2 for 4 hours to allow the cells to attach and then the Petri dish holding the chips was filled with 25 mL of DMEM/F12. Cells were grown for 48 hours before toxicity experiments.

On the day of the toxicity experiments autoclaved, 0.25 mm ID diameter, Pharmed peristaltic pump tubing (Cole-Parmer, Vernon Hills, IL) was placed into a peristaltic pump (205S, Watson Marlow, Wilmington, MA) and DMEM/F12 was pumped at 10 rpm through the tubing to remove air bubbles. Tips from 200 μL gel loading tips (Fisher Scientific, Hampton, NH) were inserted into the ends of the peristaltic pump tubing and these tips fit securely into the inlet and outlet holes of the top and bottom pieces of the GI tract μCCA and plexiglass housing around the chip μCCA.

The GI tract μCCAs were assembled by placing a 0.5 mm thick gasket on the outer edge of the bottom piece and screwing the top and bottom pieces together tightly with the membrane holding Caco-2 cells in between the two pieces. The pump flow rate was decreased to 0.75 rpm or approximately 3.5 μL/min, and tubing from one

pump channel was used for the GI tract μCCA apical or top inlet and tubing from a second pump channel was used for the basolateral or bottom inlet. Once culture medium could be seen exiting the outlet channels on the apical and basolateral sides, tubing was also connected to the outlet channels. Medium was pumped through the GI tract μCCAs during chip assembly (~1 hour) to rid the devices of air bubbles.

The silicone gaskets were peeled off the top of the chips and the chips were then placed between two pieces of 1/8" thick machined plexiglass that were screwed together tightly. The top pieces of plexiglass had two-step inlet and outlet holes (740 μm for the top half and 610 μm for the bottom half) and were cleaned with 70% EtOH and treated with oxygen plasma in an Expanded Plasma Cleaner (Harrick Plasma, Ithaca, NY) for 1 minute before assembly to increase surface wettability and sterility [20]. The bottom pieces of plexiglass were etched with ~1.5 mm deep squares that were slightly larger than the chips. A 1 mm thick piece of silicone gasket (Grace Bio-Labs) was placed into each of these cavities to allow for a tight seal between the top piece of plexiglass, chip, and bottom plexiglass piece. The bottom piece was sterilized by soaking in 70% EtOH for 30 minutes prior to assembly. After removing the silicone gasket from a chip, it was placed into the bottom plexiglass piece and 200 μL of MEM was pipetted on top of the chip. When pipetting MEM onto the chips, care was taken to remove any air bubbles in the liquid and to keep the liquid from spilling off of the chip and into the plexiglass chamber. The top plexiglass piece was then lowered straight down onto the chip, and the top and bottom pieces were screwed together.

After the chips were assembled, the outlet tubing from the basolateral side of the GI tract μCCA was connected to the liver inlet of the chip. Tubing from a third pump channel was attached to the lung inlet. 23-gauge, sterile, stainless steel needles were inserted into the tubing starts and ends. These needles were inserted into a well

from an 8-well strip plate (Corning) sealed with a silicone cover (996050MR, BioTech Solutions, Mt. Laurel, NJ), which acted as a 200 μL culture medium reservoir and debubbler. The basolateral side of the GI tract μCCA and chip shared one reservoir that contained only DMEM/F12. The apical side of the GI tract μCCA had a different reservoir that contained DMEM/F12 only (control) or DMEM/F12 +30 mM APAP.

The system was operated at 37^{o}C and 5% CO_2 for 6 hours. At the end of the experiments, cells were stained with calcein, a viability stain, and MCB, a glutathione (GSH) stain. DMEM/F12 containing 5 μM calcein and 80 μM MCB was circulated through the GI tract and chip μCCAs for 30 minutes at 37^{o}C.

4.2.6.2. Second generation μCCA toxicity experiments

Polycarbonate, 0.4 μm pore size, 12 mm diameter Snapwell membranes were coated with 8 μg/cm^2 Type I collagen dissolved in 0.02 M acetic acid for 1 hour and then washed with the same volume of PBS. Caco-2 and HT29-MTX cells at a 3:1 ratio (Caco-2:HT29-MTX) were seeded onto the membranes at a concentration of 100,000 cells/cm^2. The cells were grown on the membrane for 16 days prior to experiments to allow for full coverage of the membrane and cell differentiation.

μCCA chips were cleaned with 70% sulfuric acid and 30% hydrogen peroxide (30% H_2O_2 solution) for 10 minutes at room temperature and then rinsed with DI water. A 1 mm thick silicone gasket (Grace Bio-Labs) with holes cut out over the corresponding cell chambers was placed onto the chips to keep coatings and cell suspensions within the proper compartments. The chips covered with gaskets were dried in an oven at 60^{o}C for 30 minutes and autoclaved in a dry cycle for 30 minutes.

The μCCA chips were coated with 4 μg/cm^2 poly-D-lysine in PBS for 5 minutes at room temperature. The poly-D-lysine solution was removed and each chamber was washed with an equal volume of PBS. The chips were next coated with 8 μg/cm^2 fibronectin in PBS for 1 hour at room temperature. The fibronectin solution

was removed, and HepG2/C3A cells were seeded into the liver chamber at a concentration of 250,000 cells/cm^2. The chips were kept at 37^{o}C and 5% CO_2 for 4 hours to allow the cells to attach and then the Petri dish holding the chips was filled with 25 mL of MEM. Cells were grown for 48 hours before toxicity experiments.

Prior to toxicity experiments, autoclaved, 0.25 mm ID diameter, Pharmed peristaltic pump tubing (Cole-Parmer) was placed into a Watson Marlow 205S peristaltic pump and MEM was pumped at 10 rpm through the tubing. Tips from 200 μL gel loading tips (Fisher Scientific), which fit securely into the inlet and outlet holes of the top and bottom pieces of the GI tract μCCA and plexiglass housing around the chip μCCA, were inserted into the ends of the peristaltic pump tubing.

The GI tract μCCAs were assembled by placing first placing a sterile silicone gasket into the bottom GI tract μCCA piece. The gasket dimensions were 0.5 mm thick, 14 mm diameter, and there was a 4 mm diameter hole in the middle of the gasket corresponding in location to the etched chamber in the bottom piece (Grace Bio-Labs, gasket was cut to the correct size from a silicone sheet). The Snapwell membrane was then detached from the insert that held it suspended in the 6 well plates and the membrane was placed into the bottom chamber. A second sterile, silicone gasket (0.5 mm thick and 12 mm in diameter with a 4 mm diameter hold in the middle corresponding in location to the etched chamber in the top piece) was placed inside of the Snapwell membrane on top of the cell monolayer, and a third sterile, silicone gasket (1 mm thick, 14 mm ID, 40 mm OD) was placed on the outer edge of the bottom GI tract μCCA piece. The top and bottom pieces were then screwed together tightly with the membrane holding Caco-2 and HT29-MTX cells in between the two pieces. The pump flow rate was decreased to 0.75 rpm or approximately 3.5 μL/min, and tubing from one pump channel was used for the GI tract μCCA apical or top inlet and tubing from a second pump channel was used for the basolateral or bottom inlet.

Once culture medium could be seen exiting the outlet channels on the apical and basolateral sides, tubing was also connected to the chip outlet. Medium was pumped through the GI tract μCCAs during chip assembly (~1 hour) to rid the devices of air bubbles.

The silicone gaskets were peeled off the top of the chips and the chips were then placed between two pieces of 1/8" thick machined plexiglass that were screwed together tightly. The top pieces of plexiglass had two-step inlet and outlet holes (740 μm for the top half and 610 μm for the bottom half) and were cleaned with 70% EtOH and treated with oxygen plasma in an Expanded Plasma Cleaner (Harrick Plasma) for 1 minute before assembly to increase surface wettability and sterility [20]. The bottom pieces of plexiglass were etched with ~1.5 mm deep squares that were slightly larger than the chips. A 1 mm thick piece of silicone gasket (Grace Bio-Labs) was placed into each of these cavities to allow for a tight seal between the top piece of plexiglass, chip, and bottom plexiglass piece. The bottom piece was sterilized by soaking in 70% EtOH for 30 minutes prior to assembly. After removing the silicone gasket from a chip, it was placed into the bottom plexiglass piece and 200 μL of MEM was pipetted on top of the chip. When pipetting MEM onto the chips, care was taken to remove any air bubbles in the liquid and to keep the liquid from spilling off of the chip and into the plexiglass chamber. The top plexiglass piece was then lowered straight down onto the chip, and the top and bottom pieces were screwed together.

After the chips were assembled, the outlet tubing from the basolateral side of the GI tract μCCA was connected to the inlet of the chip and a separate tube was connected to the outlet after medium began to pool at the outlet hole. 23-gauge, stainless steel needles were inserted into the tubing starts and ends. These needles were inserted into a well from an 8-well strip plate (Corning) sealed with a silicone cover (BioTech Solutions), which acted as a culture medium reservoir and debubbler.

The basolateral side of the GI tract μCCA and chip shared one reservoir that contained 200 μL of MEM. The apical side of the GI tract μCCA had a different reservoir that contained 250 μL of MEM (control) or MEM +30 mM, 10 mM, 3 mM, or 1 mM APAP.

The system was operated at 37^{o}C and 5% CO_2 for 24 hours. At the end of the experiments, cells were stained with calcein, a viability stain, and MCB, a glutathione (GSH) stain. MEM containing 5 μM calcein and 80 μM MCB was circulated through the GI tract and chip μCCAs for 30 minutes at 37^{o}C before imaging.

4.2.7. In vitro digestion

Acetaminophen toxicity experiments were also performed after subjecting the acetaminophen to an *in vitro* digestion and using the chyme mimic as the drug transport solution. The *in vitro* digestion/Caco-2 cell culture model was developed by Glahn et al. for studying iron bioavailability from food [21]. The compound of interest is subjected to an hour long pepsin digestion at 37^{o}C and pH 2. The pepsin is then de-activated by raising the pH to 5.5-6.5 with sodium bicarbonate, a pancreatin-bile solution is added to the mixture, the pH is readjusted to 7.0 with sodium bicarbonate, and the chyme mimic is placed in an insert over a Caco-2 monolayer. In the *in vitro* digestion/acetaminophen experiments, 30 mM, 10 mM, 3 mM, and 1 mM APAP were digested and a control, drug-free digest was also prepared. A 250 μL aliquot was placed into a third reservoir and the chyme mimic was circulated through the apical GI chamber for 2 hours. After two hours the apical chamber tubing was moved to a reservoir containing MEM with no drug, and 22 hours later cells were stained with calcein and MCB and imaged.

4.2.8. Fluorescence microscopy and image analysis

Fluorescent images were acquired with a Retiga CCD camera (Qimaging,

Burnaby, BC, Canada) mounted to an Olympus BX51 microscope (Olympus America Inc., Center Valley, PA) with a 10X objective. The microscope and camera were connected to a computer running the Image Pro Plus version 4.6 software package (Media Cybernetics Inc., Silver Springs, MD) in 12-bit grayscale format. Fluorescence from the calcein stain was collected with an EGFP cube (Ex 470/Em 610, Chroma Technology Corp., Rockingham, VT). Fluorescence from the MCB-GSH adduct was collected with a DAPI cube (Ex 360/Em 460). Both image types (calcein, MCB-GSH) were obtained in the same field of view; 2 images were taken for each lung compartment (first generation devices), 6 images were taken from each liver compartment (first and second generation devices), and 4 images were taken of the Caco-2/HT29-MTX monolayer (first and second generation devices). Images were analyzed for total area stained with Image Pro Plus software.

4.2.9. HPLC analysis

APAP concentration in experimental culture medium was determined using the protocol described by Wang et al. [22]. Briefly, 100 μL samples taken from the culture medium reservoirs were extracted with 100 μL of acetonitrile (first generation experiments) or 50 μL acetonitrile (second generation experiments) and centrifuged at 3,000 rpm for 10 minutes. A 100 μL injection (first generation experiments) or 50 μL injection (second generation experiments) of the supernatant was used for determination of APAP and metabolites by reverse-phase HPLC analysis. 2-acetamindophenol was used as an internal standard. A Waters 2690 separations module and Waters 996 photodiode array detector set at a wavelength of 254 nm were used (Waters Corporation, Milford, MA). Chromatogram analysis was performed using Millennium software (version 3.0, Waters). Separations were done on a 250 x 4.6 mm, RP18, 5 μm XTerra® column (Waters, first generation experiments) or 250 x 4.6 mm, 5 μm SUPELCOSIL™ ABZ-Plus column (Supelco, Bellefonte, PA, second

generation experiments). APAP was eluted with 7% acetonitrile (v/v in water) with 0.1% trifluoroacetic acid (v/v) at a flow rate of 1.8 mL/min. Comparison with APAP, 2-acetamindophenol, acetaminophen glucuronide (APAP-GLUC), or acetaminophen sulfate (APAP-SULF) standards was used for APAP, internal standard, and metabolite identification and quantification. Figure 4.6 shows the standard elution times of APAP, 2-acetamindophenol, APAP-GLUC, and APAP-SULF.

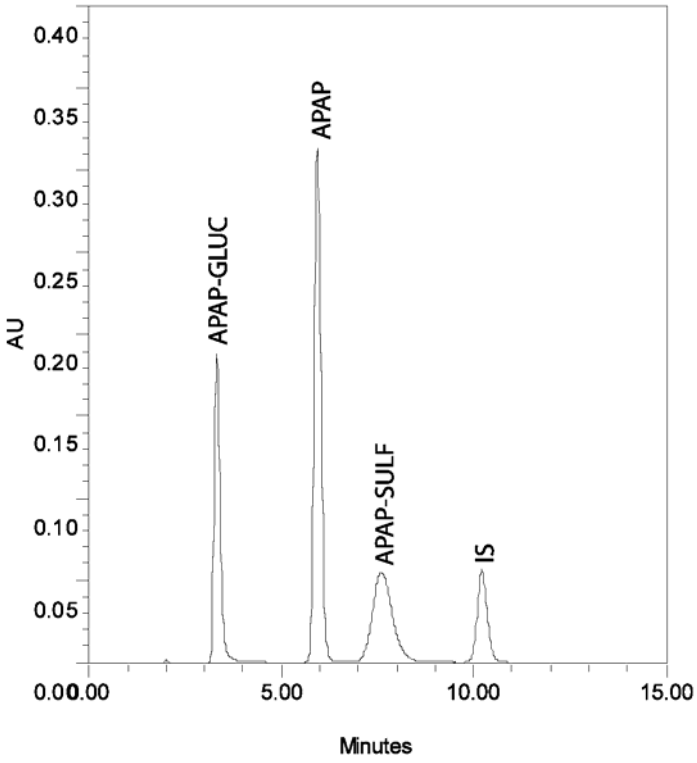

Figure 4.6. APAP, metabolite, and internal standard (IS) peaks. APAP and metabolites were eluted with 7% acetonitrile (v/v in water) with 0.1% trifluoroacetic acid (v/v) at a flow rate of 1.8 mL/min and a 250 x 4.6 mm, 5 μm SUPELCOSIL™ ABZ-Plus column. The retention times are as follows: APAP-GLUC, 3.2 minutes; APAP, 5.6 minutes; APAP-SULF, 7.2 minutes; and 2-acetamindophenol (IS), 9.8 minutes.

4.2.10. Physiologically based pharmacokinetic modeling

A PBPK model was developed for the distribution and metabolism of APAP in the human flow configuration (Figure 4.7A) and the second generation μCCA system

flow configuration (Figure 4.7B). The main purpose of this model was to aid in the development and design of the second generation μCCA system by validating the flow pattern. The organ or tissue volumes used in the simulations were obtained from Brown et al. [4]. Partition coefficients were calculated using the method described by Poulin and Theil, and the metabolic parameters for conversion of APAP to NAPQI, APAP-GLUC, and APAP-SULF in the liver were obtained from Patten et al. and Watari et al. [10, 23, 24]. The PBPK ordinary differential equations were solved with MATLAB version 7.1 (MathWorks, Natick, MA) using a fourth and fifth order Runge-Kutta-Fehlberg integration method. The PBPK code is shown in Appendix C.

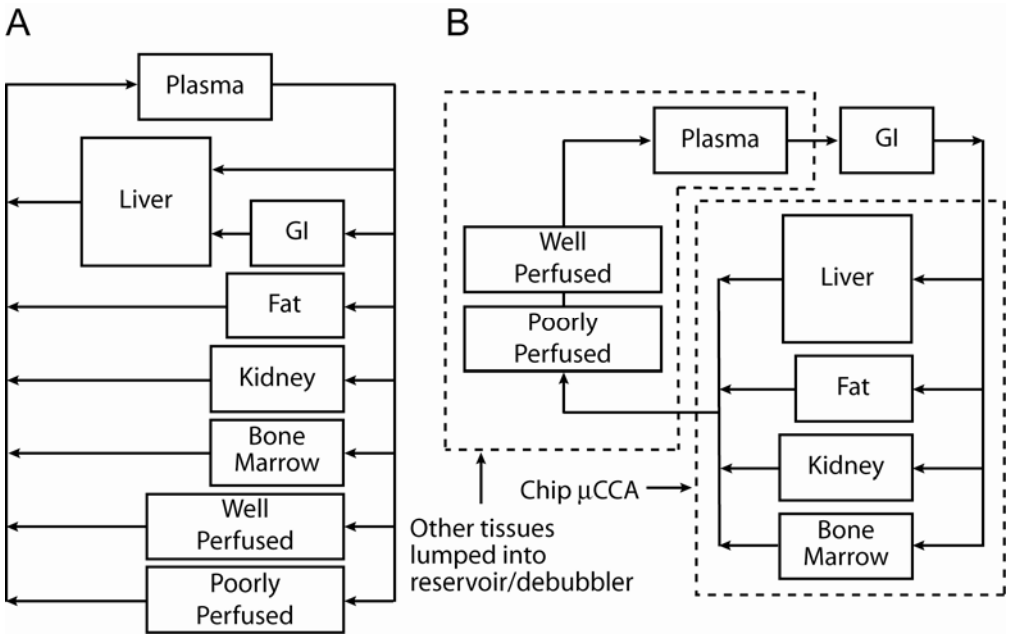

Figure 4.7. The physiologically correct, human blood flow pattern (A) and the medium flow pattern through the second generation μCCA system (B).

4.2.11. Statistical analysis

Results are expressed as mean ± standard error. Data was analyzed with GraphPad Prism version 4.00 for Windows (GraphPad Software, San Diego, CA). An unpaired Students's t-test or a one-way ANOVA with Tukey's post test was used to

compare differences between means and data was transformed when necessary to obtain equal sample variances. Differences were considered significant at $p < 0.05$.

4.3. First generation μCCA results

4.3.1. Design of the μCCAs

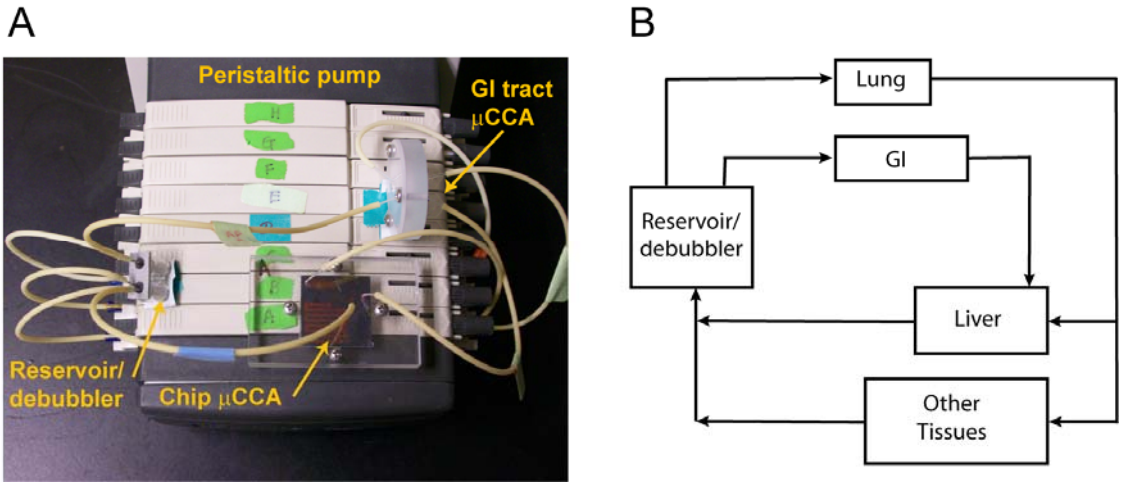

Figure 4.8. Photograph of the first generation chip and GI tract μCCA experimental set-up (A) and a PBPK schematic of the flow pattern (B).

Figure 4.7 shows a photograph of the chip and GI tract μCCA system. Three channels were used on the peristaltic pump for the two devices. The first channel pumped DMEM/F12 or DMEM/F12 +30 mM APAP through the apical chamber of the GI tract μCCA at ~3.5 μL/min. After the medium passed through the apical chamber of the GI tract μCCA, it recirculated to a reservoir containing 200 μL of DMEM/F12 or DMEM/F12 +30 mM APAP. The second channel pumped DMEM/F12 at ~3.5 μL/min into the lung chamber on the chip μCCA. After the culture medium passed through the lung chamber, 85% of the liquid went to the other tissues chamber and 15% went to the liver chamber. The third pump channel was used to pump liquid at ~3.5 μL/min into the basolateral side of the GI tract μCCA. All

liquid from the basolateral outlet of the GI tract μCCA then went through a second inlet to the liver chamber, mimicking first pass metabolism. The culture medium from the liver and other tissues chambers combined at the chip outlet and returned to a second reservoir containing 200 μL DMEM/F12 before being re-circulated to the lung and basolateral GI tract inlets. Table 4.1 compares the physiological parameter values for rat with those of the GI tract and chip μCCAs. The chip chambers and channels were designed so that the pressure drop was the same for each, allowing for a passive fluid flow split.

Table 4.1. Comparison between rat physiological parameter and μCCA design parameter values for the first generation μCCA system. Values for rat body weight, regional blood flow distribution, and organ residence times were taken from Brown et al. [4]. GI flow rates for the μCCA represent flow through the basolateral GI tract μCCA chamber.

Tissue	% Body weight (rat)	% Cardiac output (rat)	Residence time (s)
GI	2.7%	14%	26
Lung	0.50%	100%	1
Liver	3.4%	18%	27
Other	96%	82%	186

Tissue	% μCCA compartment volume	% Medium flow (μCCA)	Residence time (s)
GI	2.3%	100%	5
Lung	0.98%	100%	2
Liver	3.6%	115%	7
Other	93%	85%	243

4.3.2. Cell line selection

The L2 rat lung cell line was used to imitate the lung, a toxicity target tissue [6, 25]. L2 cells possess many of the characteristics of primary rat type II lung epithelial cells, including glutathione-S-transferase activity [26]. The HepG2/C3A cell line, which is a subclone of the HepG2 cell line, was used as a model for the liver. This cell line has detectable CYP1A and 2E1, UDP-glucuronyltransferase, sulfotransferase, and glutathione-S-transferase activity [27]. The Caco-2 cell line was used to mimic the intestinal epithelium. When seeded onto Type I collagen-coated inserts or culture

plates under normal culture conditions, Caco-2 cells differentiate into a polarized, enterocyte-like epithelial barrier that is morphologically and biochemically very similar to the small intestinal epithelium [28]. After a growth period of two to three weeks, the Caco-2 monolayers express tightly packed microvilli, tight junctions, and are capable of paracellular, transcellular, active, and transcytotic transport [29]. Type I collagen is used to model the epithelial basement membrane because it has been found to best stimulate proliferation, cell spreading, and differentiation in static Caco-2 cultures [30]. Caco-2 cells also express CYP1A, 2E1, UDP-glucuronyltransferase, sulfotransferase, and glutathione-S-transferase [31-33].

4.3.3. CYP1A and CYP2E1 activity

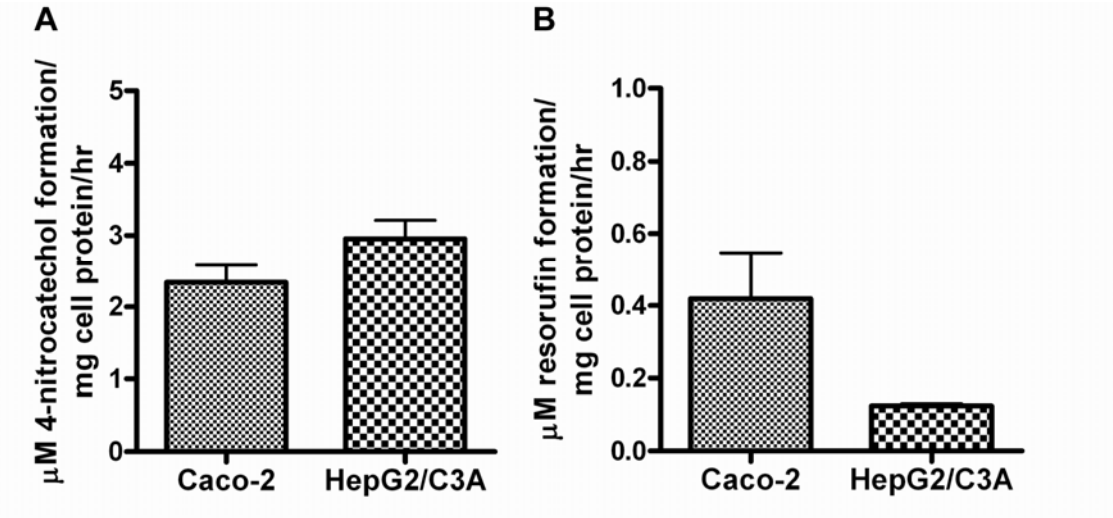

Figure 4.9. Metabolizing cell line CYP2E1 (A) and CYP1A (B) activity (n = 32).

The CYP1A and 2E1 activity of HepG2/C3A and Caco-2 cells was assessed using a fluorescent and colorimetric substrate (Figure 4.9). CYP2E1 activity is expressed as μM 4-nitrocatechol formation/mg cell protein/hr and CYP1A activity is expressed as μM resorufin formation/mg cell protein/hr. Both cell lines have detectable CYP1A and CYP2E1 activity under the culture conditions used for these experiments, although the values are much lower than those found in humans [27, 32].

4.3.4. μCCA acetaminophen toxicity

Culture medium with 30 mM APAP was pumped through the apical chamber of the GI tract μCCA for 6 hours. Culture medium without drug was pumped through the basolateral chamber of the GI tract μCCA and chip μCCA, therefore drug had to diffuse through the Caco-2 cell monolayer to reach the chip. After the 6-hour experiments, cells were stained with calcein and MCB to indicate viable cells and glutathione levels, respectively. Control experiments were run simultaneously without APAP in the GI tract μCCA apical chamber.

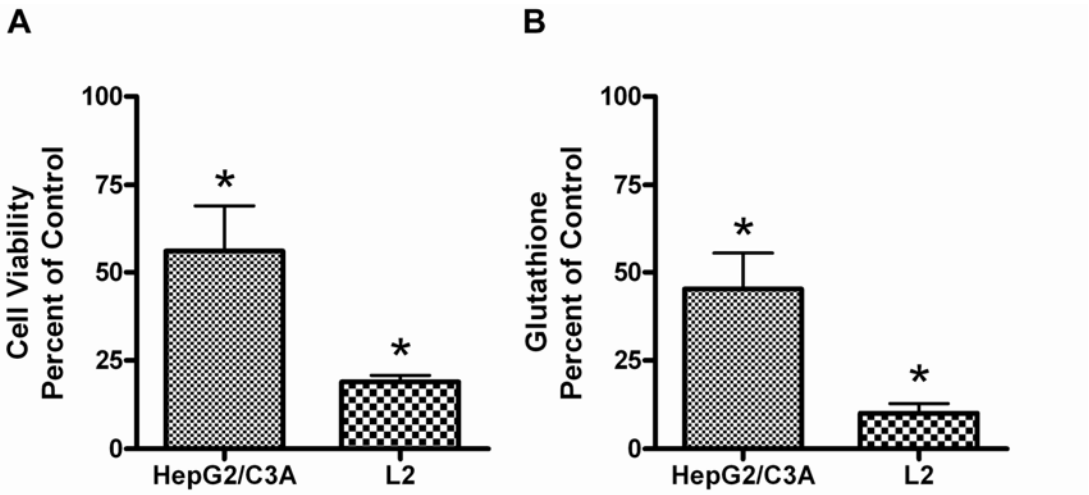

Figure 4.10. HepG2/C3A and L2 viability (A) and glutathione levels (B) after culture medium with 30 mM APAP was pumped through the apical chamber of the first generation GI tract μCCA for 6 hours. Controls had only culture medium pumped through the apical GI tract μCCA chamber. Values are expressed as a percent of control ± SEM. Differences in viability or glutathione levels between cells exposed to APAP and controls that are significant according to an unpaired Student's t-test are indicated with a * ($p < 0.05$, $n = 3$).

Figure 4.10A shows the cell viability results as a percent of control. The viability of HepG2/C3A cells decreased to 56% of the control and the viability of L2 cells decreased to 18% of the control. Figure 4.10B shows the cell glutathione levels as a percent of control. The HepG2/C3A glutathione levels decreased to 45% of the control and the L2 glutathione levels decreased to 10% of the control. Figure 4.11

shows the control (Figures 4.11A and 4.11C) and 30 mM APAP treated (Figures 4.11B and 4.11D) HepG2/C3A and L2 cells on the chip. The Caco-2 images were taken through ½" etched plexiglass, which did not allow for images that were of high enough quality for analysis. The Caco-2 cells were viable and the monolayers did remain intact in controls and after APAP exposure (data not shown).

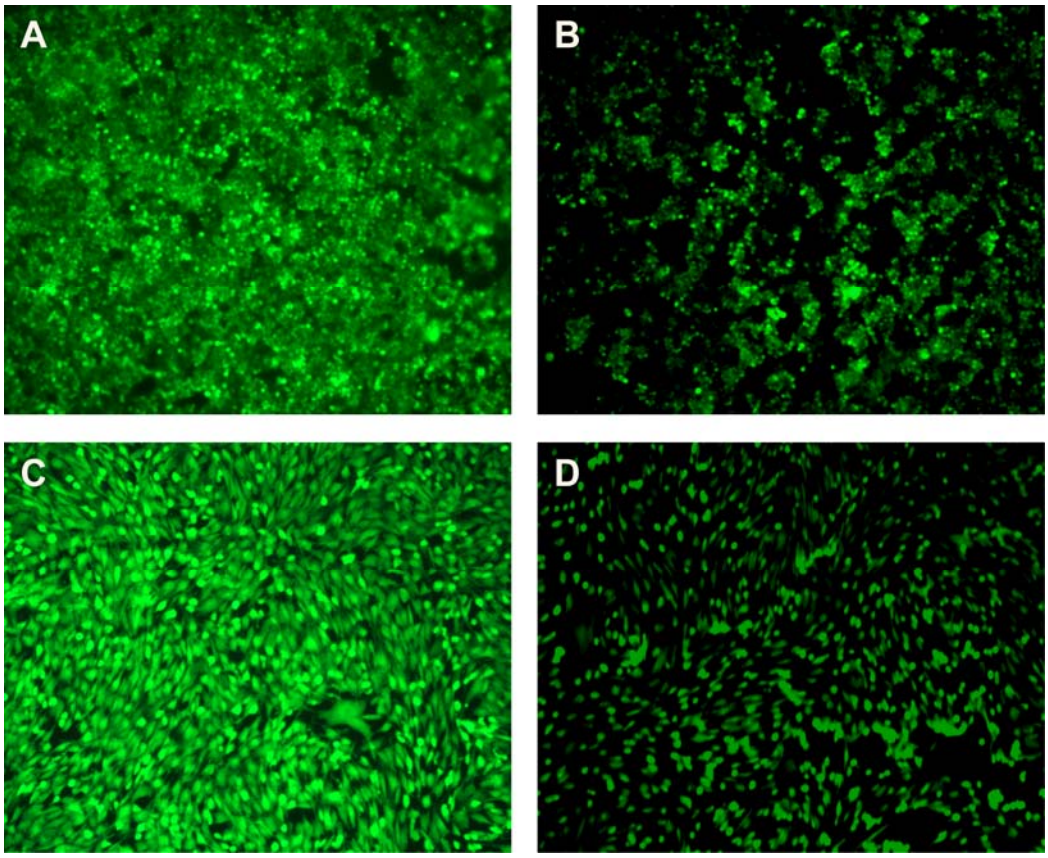

Figure 4.11. Comparison of control (A) and 30 mM APAP treated (B) HepG2/C3A cells and control (C) and 30 mM APAP treated (D) L2 cells on the chip μCCA after a 6 hour experiment where culture medium (control) or 30 mM APAP was pumped through the apical chamber of the GI tract μCCA.

HPLC analysis of the apical and basolateral GI tract μCCA culture medium revealed that the concentration of APAP in the basolateral chamber, and, therefore the medium circulating through the chip, reached 10 ± 2.6 mM. The APAP concentration in culture medium in the apical chamber decreased from 30 mM to 13 ± 3.1 mM after

the 6 hour experiment.

Experiments with only the chip μCCA were run with DMEM/F12 +30 mM APAP re-circulating for 6 hours. These experiments were done to determine the effects of adding the GI tract μCCA to the system. The result was 100% cell death for both HepG2/C3A and L2 cells (data not shown).

4.4. Second generation μCCA results

4.4.1. Design of the μCCAs

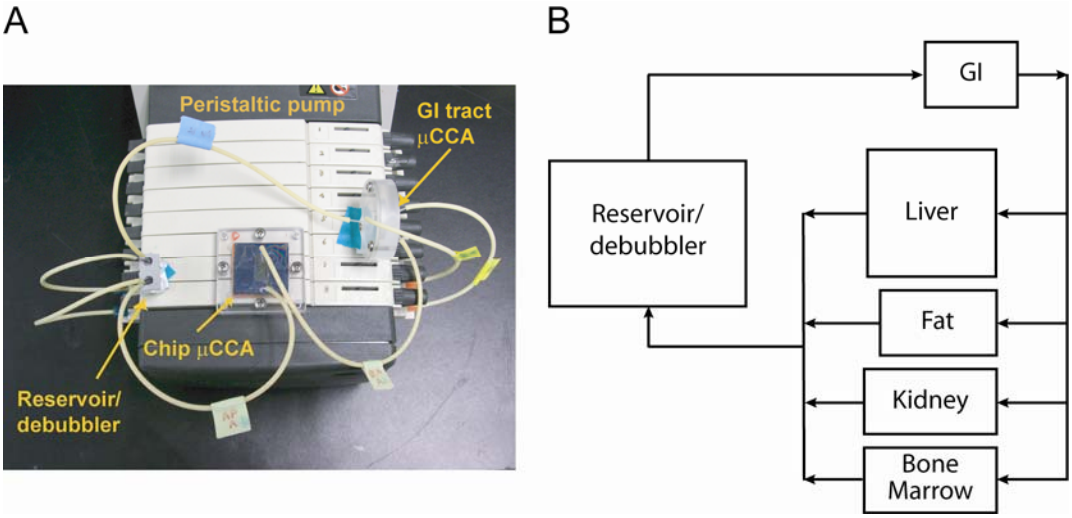

Figure 4.12. Photograph of the second generation chip and GI tract μCCA experimental set-up (A) and a PBPK schematic of the flow pattern (B).

Figure 4.12 shows a photograph of the connected second generation chip and GI tract μCCAs. Two channels were used on the peristaltic pump for the two devices. The first channel pumped MEM or MEM +30 mM, 10 mM, 3 mM, or 1 mM APAP through the apical chamber of the GI tract μCCA at ~3.5 μL/min. After the medium passed through the apical chamber of the GI tract μCCA, it returned to a reservoir containing 250 μL of MEM or MEM +APAP. The second channel pumped MEM at ~3.5 μL/min into the chip inlet. The flow immediately split after entering the chip and 41% of the flow went to the liver chamber, 35% went to the kidney chamber, 17%

went to the bone marrow chamber, and 7% went to the fat chamber. The culture medium chambers combined at the chip outlet and returned to a second reservoir containing 200 μL MEM before being recirculated to the basolateral GI tract inlet. Table 4.2 compares the physiological parameter values for humans with those of the μCCA. The chip chambers and channels were designed so that the pressure drop was the same for each, allowing for a passive fluid flow split. Design calculations are shown in Appendix B.

Table 4.2. Comparison between human physiological parameter and μCCA design parameter values for the second generation μCCA system. Values for human body weight, regional blood flow distribution, and organ residence times were taken from Brown et al. [4]. GI flow rates for the μCCA represent flow through the basolateral GI tract μCCA chamber.

Tissue	% Body weight (human)	% Caridac output (human)	Residence time (min)
GI	2.4%	19.6%	1.5
Liver	2.4%	25.9%	1.2
Kidney	0.4%	22.1%	0.2
Bone Marrow	2.1%	11.0%	2.4
Fat	14.3%	4.6%	38.5
Other	78.4%	16.8%	58.8

Tissue	% μCCA compartment volume	% Medium flow (μCCA)	Residence time (min)
GI	1.0%	100.0%	0.6
Liver	0.8%	41.0%	1.2
Kidney	0.1%	35.0%	0.2
Bone Marrow	0.7%	17.0%	2.4
Fat	4.5%	7.0%	38.5
Other	92.8%	100.0%	55.7

The practical design of a μCCA system requires that well perfused and poorly perfused tissues or organs not included in the study are lumped together with the plasma compartment as shown in Figure 4.7. Organs or tissues should be grouped together based on characteristics such as perfusion, drug or chemical partitioning, and metabolism, and can then be considered mathematically as a functionally equivalent bulk average [34]. Design constraints can also require that the medium flow pattern in μCCAs is modified from the physiologically correct blood flow pattern. In the second generation device, for example, the need to eliminate multiple inlets and outlets on the chip μCCA prevented a design that accurately mimicked first pass metabolism (i.e. all

culture medium from the GI tract μCCA flows directly to the liver compartment). The impact of lumping and changes to the flow pattern on chemical or drug pharmacokinetics can be examined by creating representative PBPK models.

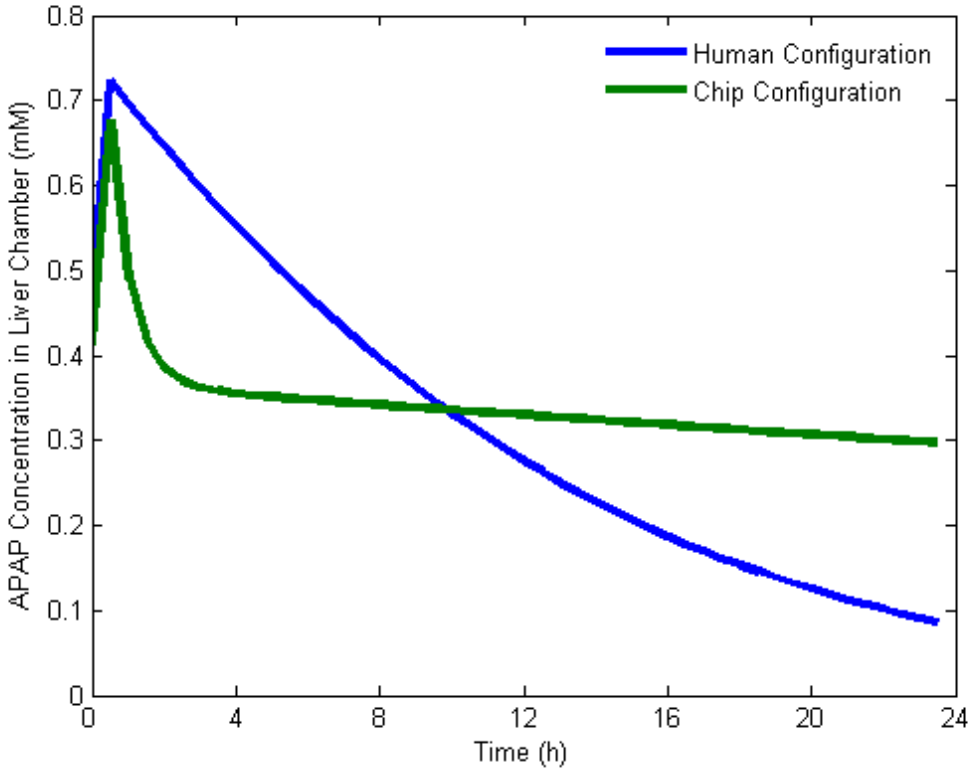

Figure 4.13. Comparison of PBPK predicted APAP distribution in the liver chamber for a human flow configuration and the second generation μCCA system flow configuration after a 1mM oral APAP dose. The APAP area under the curve (AUC) of the human configuration is 92% of the chip μCCA configuration APAP AUC after 24 hours.

Figure 4.13 shows the results of PBPK predicted APAP distribution to the liver compartment after a 1 mM oral dose for a physiologically correct flow structure and for the second generation μCCA system flow structure. These results show that for both configurations the maximum APAP concentration is reaches after 1 hour. In the chip μCCA configuration the APAP concentration rapidly decreases in the liver compartment over hours 2-3 and then gradually decreases for the remaining 21 hours,

while in the human configuration there is a steady APAP concentration decrease over hours 2-24 in the liver compartment. The area under the curve (AUC), which corresponds to the total drug exposure, for the human configuration liver compartment was 92% of the chip configuration liver compartment AUC after 24 hours. This means that both configurations receive approximately the same APAP dose over a 24 hour period.

4.4.2. Cell line selection

The HepG2/C3A cell line, which has detectable CYP1A and 2E1, UDP-glucuronyltransferase, sulfotransferase, and glutathione-S-transferase activity, was used to model the liver [27]. Co-cultures of the Caco-2 and HT29-MTX cell lines were used to mimic the absorptive entrocyte and mucus-secreting goblet cells of the intestinal epithelium, respectively. Caco-2 cells differentiate into a polarized, absorptive enterocyte-like epithelial barrier that is morphologically and biochemically very similar to the small intestinal epithelium [28]. HT29-MTX cells are a subpopulation of HT29 human colonic adenocarcinoma cells selected for resistance to methotrexate (MTX) that consist exclusively of differentiated, mucus-secreting, goblet-like cells that retain their differentiated phenotype after reversion to MTX-free medium [14]. Caco-2 cells have been shown to express CYP1A, CYP2E1, UDP-glucuronyltransferase, sulfotransferase and glutathione-S-transferase [31-33].

4.4.3. μCCA acetaminophen toxicity

Culture medium with APAP was pumped through the apical chamber of the GI tract μCCA for 24 hours. Culture medium without drug was pumped through the basolateral chamber of the GI tract μCCA and chip μCCA, therefore drug had to diffuse through the Caco-2/HT29-MTX cell monolayer to reach the chip. In experiments including digested APAP, chyme mimic contained drug was circulated

through the apical chamber for two hours, and then MEM with no drug was circulated through the apical chamber for the remaining 22 hours. After the 24-hour experiments, cells were stained with calcein and MCB to indicate viable cells and glutathione levels, respectively. Control experiments were run simultaneously without APAP in the GI tract μCCA apical chamber. In experiments including digestion, chyme mimic with no drug was circulated through control apical chambers for 2 hours, and MEM with no drug was circulated through the apical chamber for the remaining 22 hours. Viability and glutathione levels for liver cells are shown below. Glutathione levels are shown for the Caco-2/HT29-MTX monolayers. Calcein stain was used in the Caco-2/HT29-MTX monolayers to visualize monolayer integrity, and results were discarded if the monolayers did not remain intact.

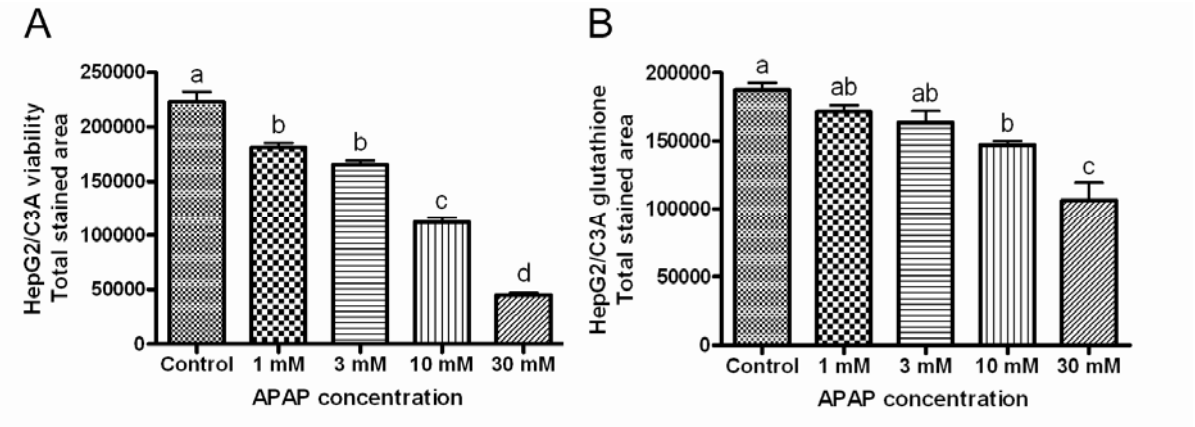

Figure 4.14. HepG2/C3A viability (A) and glutathione levels (B) after culture medium with APAP was pumped through the apical chamber of the second generation GI tract μCCA for 24 hours. Controls had only culture medium pumped through the apical GI tract μCCA chamber. Values are expressed as mean ± SEM. Bars with no letter in common are significant according to a one-way ANOVA with Tukey's post test ($p < 0.05$, $n = 3$).

The results in Figure 4.14 show that as the concentration of APAP in the apical GI chamber increases, the viability and glutathione concentration of the cells in the liver compartment decreases. The glutathione levels also decreased with increasing APAP concentration in the Caco-2/HT29-MTX membranes (Figure 4.15). Figure 4.16

shows representative photographs of HepG2/C3A cells after a 24 hour exposure to APAP in GI tract μCCA apical chamber culture medium.

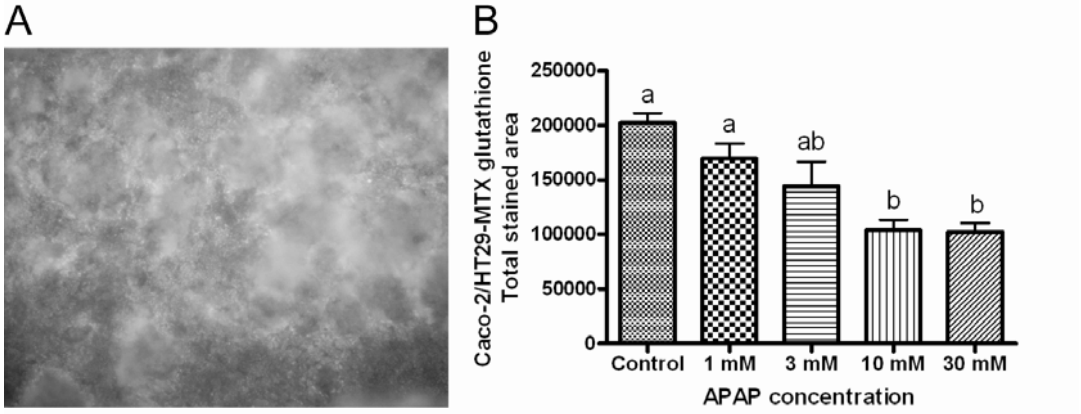

Figure 4.15. (A) A representative photograph of the Caco-2/HT29-MTX monolayer after a 24 hour exposure to APAP and staining with calcein. Calcein was used only to determine if the monolayer was intact and not for viability analysis. (B) Caco-2/HT29-MTX glutathione levels after culture medium with APAP was pumped through the apical chamber of the second generation GI tract μCCA for 24 hours. Controls had only culture medium pumped through the apical GI tract μCCA chamber. Values are expressed as mean ± SEM. Bars with no letter in common are significantly different according to a one-way ANOVA with Tukey's post test ($p < 0.05$, $n = 3$).

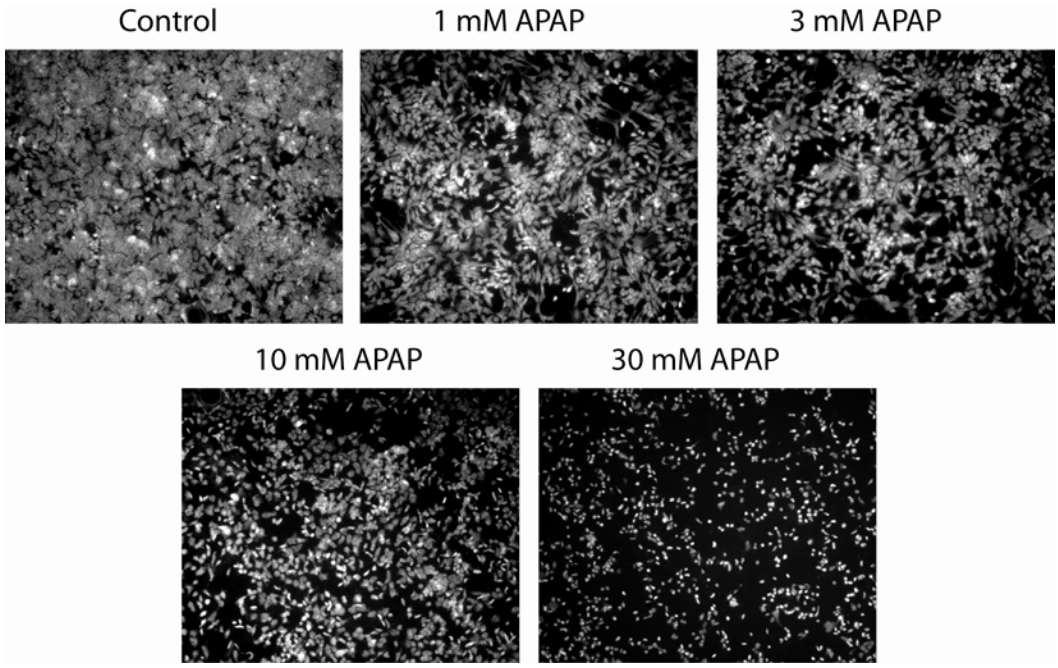

Figure 4.16. Representative photographs of HepG2/C3A liver cells after a 24 hour exposure to APAP in the GI tract μCCA apical chamber culture medium.

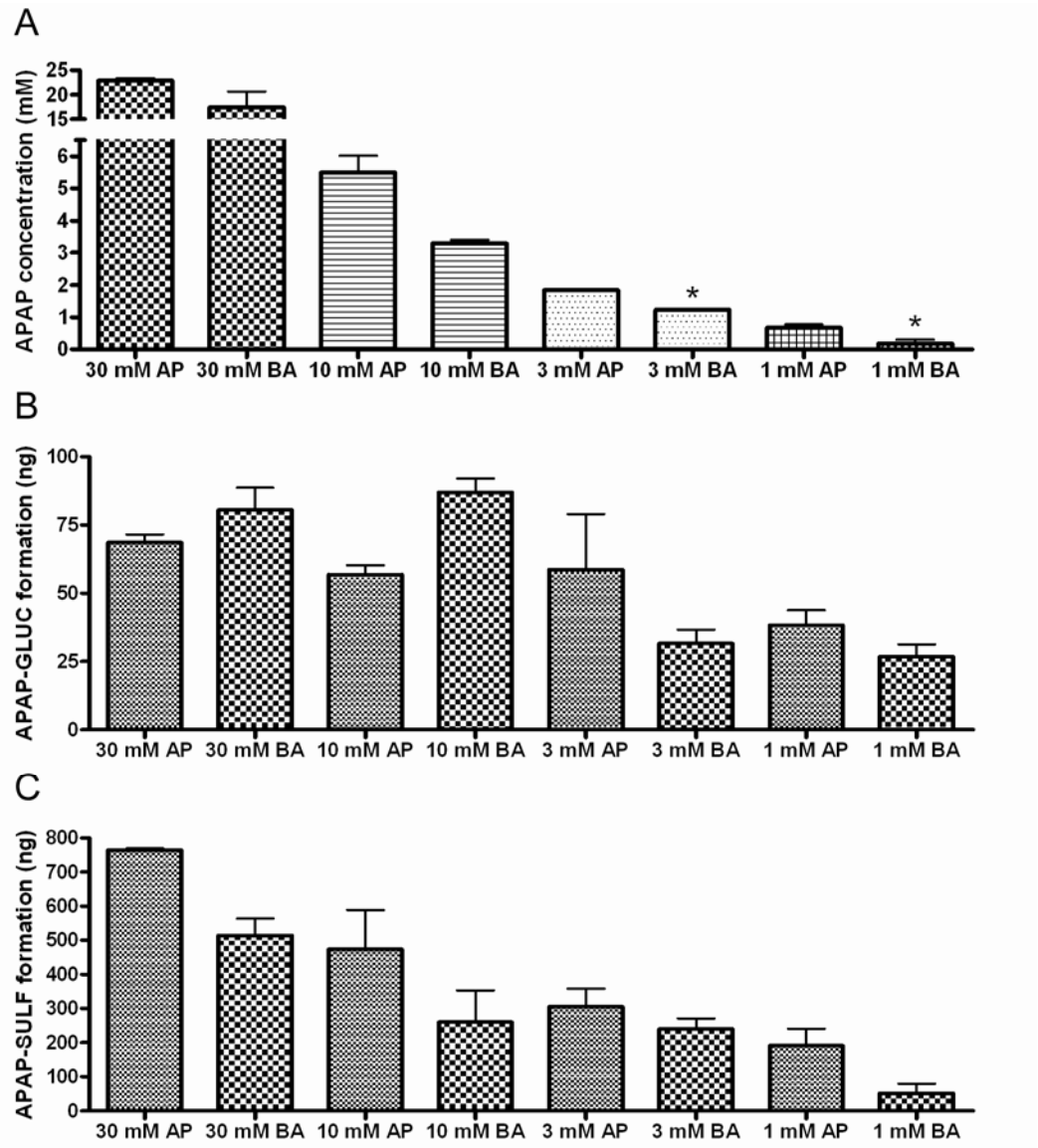

Figure 4.17. (A) APAP, (B) APAP-GLUC, and (C) APAP-SULF concentration after 24 hours in the apical GI reservoir (AP) and the basolateral GI/chip reservoir (BA). Values are expressed as mean ± SEM. Bars with a * are significant according to a one-way ANOVA with Tukey's post test ($p < 0.05$, $n = 3$).

Figure 4.17 shows the APAP and APAP metabolite concentration after 24 hours in the apical GI reservoir and the basolateral GI/chip reservoir. The APAP concentration was generally lower in the basolateral/chip reservoir, but this difference was statistically significant only for the 1 mM and 3 mM concentrations. The formation of APAP-GLUC remained fairly constant for all of the APAP

concentrations. This suggests that the UDP-glucuronyltransferase-catalyzed reaction was close to saturated even at low APAP exposure. The sulfotransferase activity was found to be much higher in these cell lines. The formation of APAP-SULF was approximately 13 times greater in the 30 mM apical chamber when compared with APAP-GLUC, and APAP-SULF formation generally decreased in the apical and basolateral chambers with decreasing APAP concentration, suggesting that at lower APAP concentrations this enzyme was not saturated.

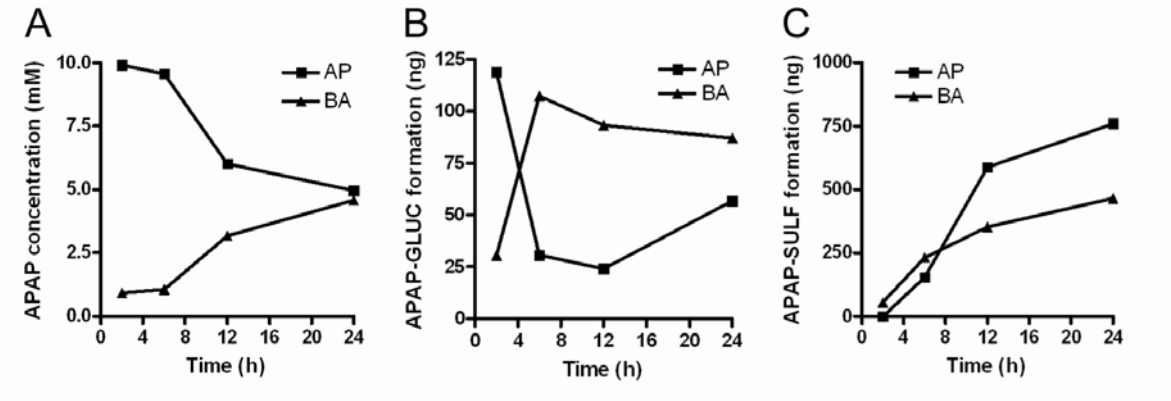

Figure 4.18. Results of HPLC analysis for a time course experiment with devices exposed to 10 mM APAP. (A) APAP, (B) APAP-GLUC, and (C) APAP-SULF concentrations at 2, 6, 12, and 24 hours (n = 1).

A time course experiment was performed with devices exposed to 10 mM APAP. The devices were disassembled at 2, 6, 12, and 24 hours to determine APAP and metabolite concentration in the apical and basolateral chambers. These results are shown in Figure 4.18. The concentration of APAP in the basolateral/chip reservoir gradually increased over the 24 hour period, but never reached equilibrium with the apical chamber. The formation of APAP-GLUC reached saturation after 6 hours in the basolateral chamber and chip, and decreased in the apical chamber after the first time point. APAP-SULF formation increased over the 24 hour period in the apical chamber and basolateral chamber/chip.

4.4.4. μCCA digested acetaminophen toxicity

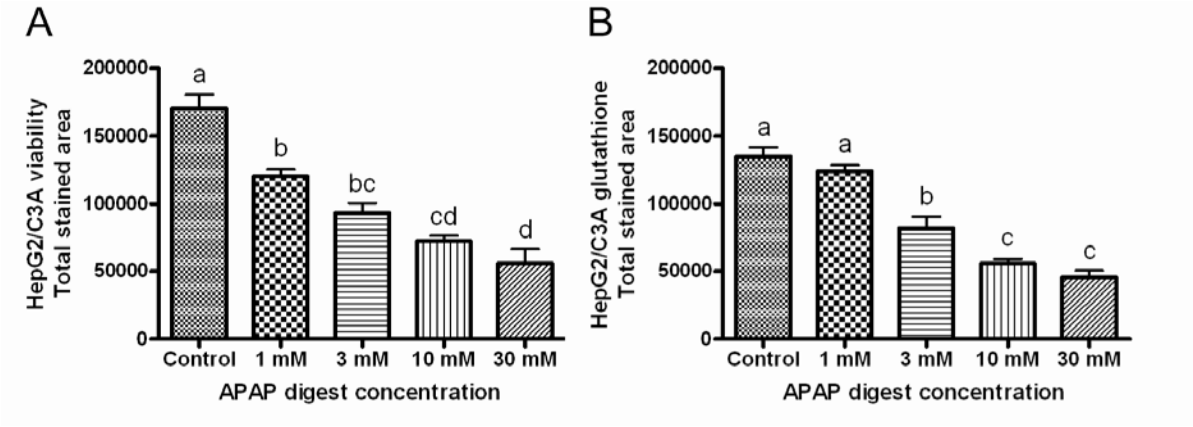

Figure 4.19. HepG2/C3A viability (A) and glutathione levels (B) after digested APAP was pumped through the apical chamber of the second generation GI tract μCCA for 2 hours followed by culture medium with no drug for 22 hours. Controls had chyme mimic with no APAP circulated through the apical GI tract μCCA chamber for 2 hours followed by culture medium with no drug for 22 hours. Values are expressed as mean ± SEM. Bars with no letter in common are significant according to a one-way ANOVA with Tukey's post test ($p < 0.05$, $n = 3$).

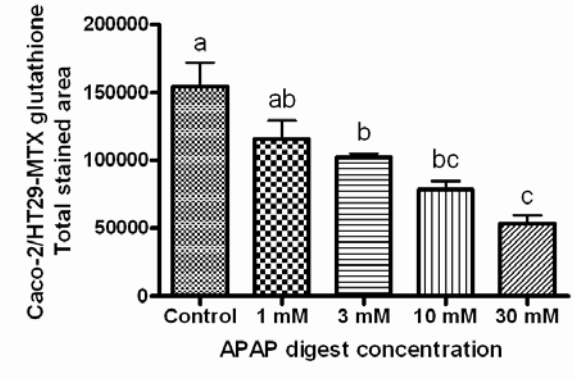

Figure 4.20. Caco-2/HT29-MTX glutathione levels after digested APAP was pumped through the apical chamber of the second generation GI tract μCCA for 2 hours followed by culture medium with no drug for 22 hours. Controls had chyme mimic with no APAP circulated through the apical GI tract μCCA chamber for 2 hours followed by culture medium with no drug for 22 hours. Values are expressed as mean ± SEM. Bars with no letter in common are significant according to a one-way ANOVA with Tukey's post test ($p < 0.05$, $n = 3$).

Figures 4.19 and 4.20 show the results for experiments with digested APAP. As the APAP concentration in the apical chamber increased, the viability of liver cells and the glutathione levels of liver cells and Caco-2/HT29-MTX cells decreased

significantly. Digestive enzymes in the chyme mimic did affect the viability of the liver cells, as the control viability for digestion experiments (Figure 4.19) was lower when compared with the control viability for experiments were only culture medium was circulated through the devices (Figure 4.14).

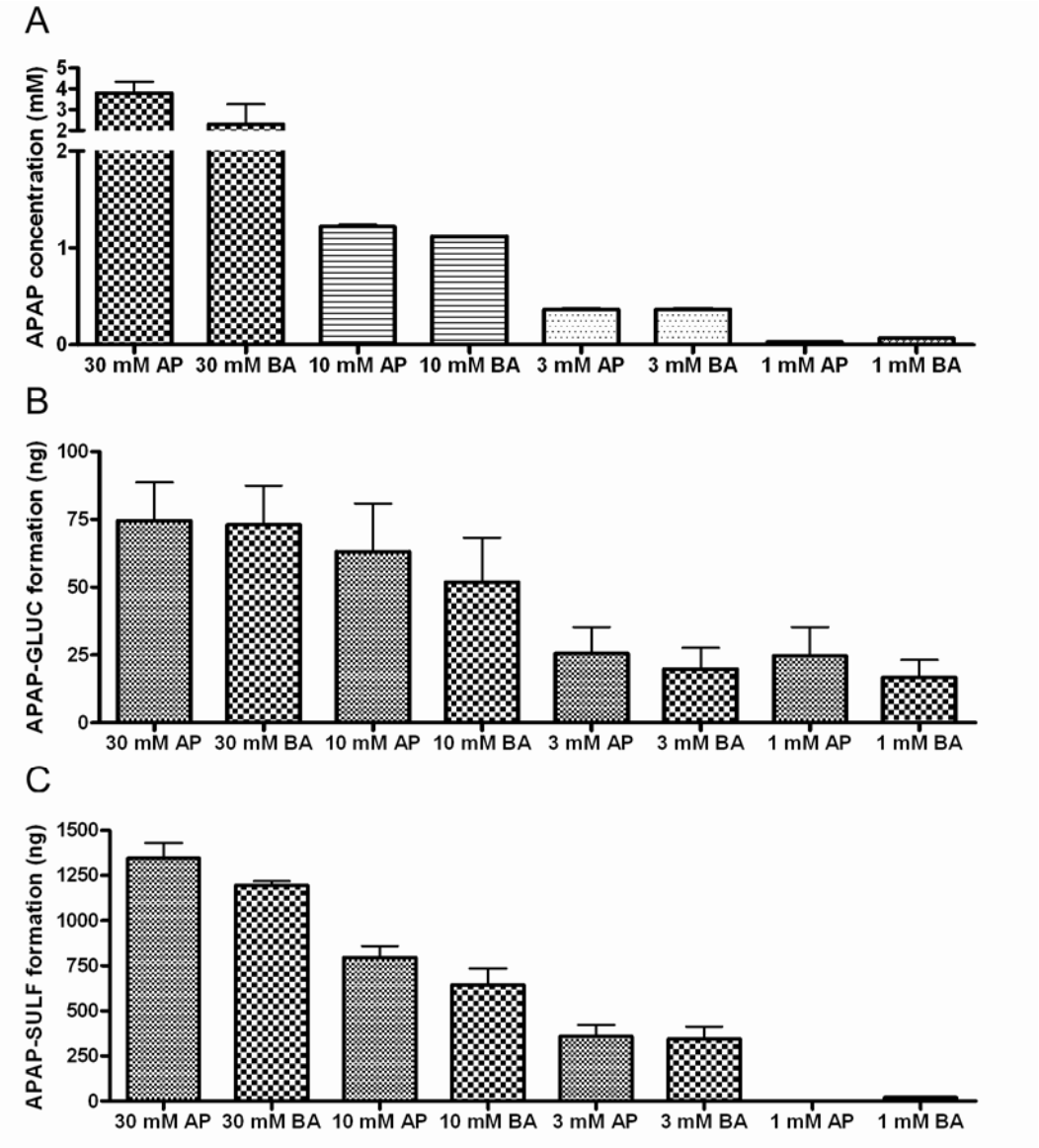

Figure 4.21. (A) APAP, (B) APAP-GLUC, and (C) APAP-SULF concentration for digested APAP after 24 hours in the apical GI reservoir (AP) and the basolateral GI/chip reservoir (BA). Values are expressed as mean ± SEM.

Figure 4.21 shows the APAP and APAP metabolite concentration after 24 hour experiments with digested APAP. The concentration of APAP in the apical and basolateral chambers was lower when compared with previous experiments where MEM containing APAP was circulated through the apical chamber for 24 hours. When the chyme mimic containing 30 mM APAP was used, for example, the concentration of APAP in the apical chamber and basolateral chamber/chip reached ~3.5 mM after 24 hours. There was no significant difference between the apical chambers and basolateral chambers/chips, which means that the APAP concentration reached equilibrium between the apical chambers and basolateral chambers/chips after 24 hours for all concentrations tested. The formation of APAP-GLUC decreased for lower APAP concentrations tested, which shows that at APAP concentrations lower than 1 mM UDP-glucuronyltransferase is not saturated. APAP-SULF formation was much greater than APAP-GLUC formation, and APAP-SULF generally decreased in the apical chamber and basolateral chamber/chip with decreasing APAP concentration.

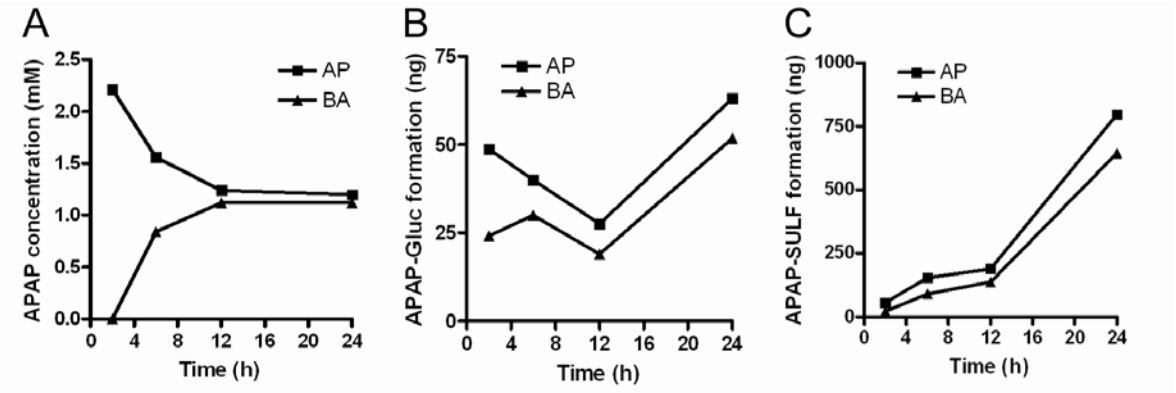

Figure 4.22. Results of HPLC analysis for a time course experiment with devices exposed to 10 mM digested APAP. (A) APAP, (B) APAP-GLUC, and (C) APAP-SULF concentration at 2, 6, 12, and 24 hours (n = 1).

Results from a time course experiment with 10 mM digested APAP are shown in Figure 4.22. The devices were disassembled at 2, 6, 12, and 24 hours to determine

APAP and metabolite concentration in the apical and basolateral chambers. The concentration of APAP in the basolateral/chip reservoir was very close to the concentration of APAP in the apical chamber by 12 hours, and equilibrium was reached by 24 hours. The formation of APAP-GLUC was relatively low and approximately the same in the apical chamber and basolateral chamber/chip. APAP-SULF formation increased over the 24 hour period in the apical chamber and basolateral chamber/chip at about the same rate.

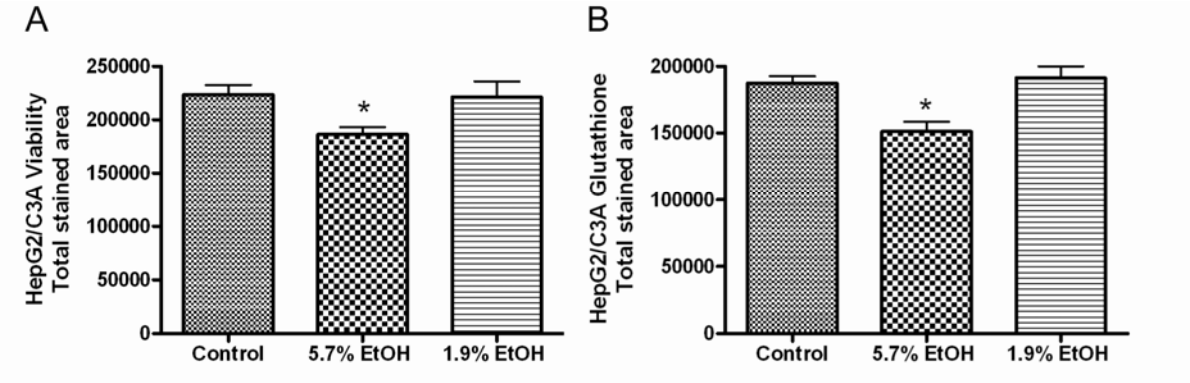

Figure 4.23. HepG2/C3A viability (A) and glutathione levels (B) after 5.7% or 1.9% ethanol was pumped through the apical chamber of the second generation GI tract μCCA for 24 hours. Controls had culture medium with no APAP circulated through the apical GI tract μCCA chamber for 24 hours. Values are expressed as mean ± SEM. Bars with a * are significant according to a one-way ANOVA with Tukey's post test ($p < 0.05$, $n = 3$).

APAP is not soluble in water and was dissolved at a concentration of 0.5 M in 95% ethanol before dilution in MEM or digestion. At high concentrations of APAP, this resulted in a significant amount (5.7% at 30 mM and 1.9% at 10 mM) of ethanol in the culture medium. Control experiments were performed to determine the effects of ethanol on liver cell viability, and these results are shown in Figure 4.23. It was found that there was significant cell death caused by 5.7% (v/v) ethanol (approximately 17%), but liver cells exposed to 1.9% ethanol were not significantly affected.

4.5. Discussion

Oral delivery is the preferred route of pharmaceutical administration due to the relatively low medical costs and relatively high patient comfort, compliance and convenience; but the intestinal wall acts as a biological barrier that both limits the uptake of and biotransforms drugs [35, 36]. Biotransformation occurs during transcellular absorption when pharmaceuticals come in contact with phase I and phase II enzymes [37]. The most notable phase I enzymes belong to the cytochrome P450 superfamily which oxidize compounds, especially chemicals or drugs that are hydrophobic and relatively insoluble, to form a reactive intermediate [38]. The reactive intermediate is then susceptible to conjugation by a phase II enzyme such as UDP-glucuronyltransferase, sulfotransferase, or glutathione-S-transferase [37]. The resulting conjugate is usually pharmacologically inactive and less lipid soluble than its precursor, allowing the conjugate to be excreted in bile or urine [38].

The membrane lining the small intestine is composed of two main cell types: enterocyte and goblet. Absorptive enterocytes make up about 90% of the cell population in the upper intestine, display very tight intracellular junctions, and are covered with 1 μm long, tightly packed projections called microvilli [39]. Microvilli further increase the surface area of the intestine available for absorption. The absorptive cells allow the passage of small molecules by one or more of four different routes: passive transcellular (through the cell), passive paracellular (between cells), active (energy-dependent) carrier-mediated and transcytosis (transport across the epithelium with uptake into coated vesicles) [40]. Any material that is absorbed in the intestine must first diffuse across the mucus layer, the epithelial cells lining the intestine, the lamina propria, and the endothelial cells that line the capillaries, but the epithelial cell layer has been shown to be the rate-limiting step [41]. Caco-2 cells mimic absorptive enterocytes, which are the most populous cells in the intestinal

epithelium. Caco-2 cells also develop tight junctions, possess microvilli, can transport small molecules by all four major transport routes, and express many phase I and phase II enzymes [29, 31-33]. These qualities, along with the fact that epithelial cell layer has been shown to be the most significant barrier to oral absorption; make Caco-2 cells an appropriate model for oral absorption studies.

APAP is a weak organic acid (pKa = 9.7) that is not ionized at pH 7 [38]. Because APAP is a small molecule and non-ionized at a physiological pH, it is able to passively diffuse through the small intestinal cell membrane. Passive diffusion of a drug involves the movement of drug molecules down a concentration gradient without the expenditure of energy; the rate of penetration of a drug across a membrane is related to the concentration gradient by Fick's Law [38].

APAP is also one of the most widely used analgesic and antipyretic drugs by children and adults worldwide, and the pharmacological side effects are thought to be based on the inhibition of prostaglandin synthesis [8, 42]. Therapeutic doses of immediate release APAP preparations are normally absorbed from the GI tract within one hour, while peak serum concentrations in acute overdose may be delayed for up to four hours [42]. A common tool that is used to predict potential hepatotoxic acetaminophen effects is the Rumack-Matthew scale [43]. The nomogram has a line from 200 mg/L serum APAP concentration at 4 hours to 50 mg/L at 12 hours after APAP overdose. Untreated patients with a serum APAP concentration above the line are considered at risk for hepatic damage. A 200 mg/L serum concentration is approximately 1 mM, which was the lowest APAP concentration tested with the μCCA devices.

At therapeutic levels APAP is generally considered safe, but high doses cause liver cell necrosis [44]. The liver toxicity is due to CYP bioactivation of APAP to a reactive metabolite, NAPQI [10]. The lung is also one of the major targets for

exposure to xenobiotics because it receives 100% of cardiac output, and in humans lung injury is a common result of APAP overdose [45, 46]. Studies with rat type II pneumocytes and alveolar macrophages suggest that CYP and/or prostaglandin synthetase are involved in APAP lung toxicity [47].

With the first generation GI tract μCCA we describe a prototype *in vitro* system that for the first time, although at a very basic level, mimics oral exposure to a drug, first pass metabolism, and the circulation of metabolites on a microscale. These results demonstrate that APAP can cross the Caco-2 cell monolayer and damage cells in the liver and lung compartments. The GI tract μCCA minimizes the toxicity of the APAP dose and acts as a barrier, however, as 30 mM APAP running through only the chip μCCA resulted in 100% cytotoxicity and the final concentration of APAP in the chip μCCA run together with the GI tract μCCA was approximately 10 mM. The GI tract μCCA could be minimizing the toxicity in one or a combination of the following ways: the concentration of the APAP could quickly reach near-equilibrium between the two μCCAs, and the extra medium flowing through the GI tract μCCA could dilute the concentration to a less toxic concentration; the Caco-2 cells could metabolize some of the drug into harmless compounds, preventing some of the APAP from reaching the liver and lung compartments; and/or the Caco-2 monolayer may truly act as a barrier and the drug may slowly diffuse into the basolateral chamber.

The primary markers for cell toxicity in the first generation μCCA system experiments were glutathione depletion and cell viability. After a 6 hour exposure to APAP approximately half of the liver cells remained, while only about 20% of the lung cells remained viable (Figure 4.10A). The APAP dose was less toxic to the HepG2/C3A cells, which does not mimic *in vivo* results. The L2 cell line, however, expresses fewer phase II enzymes than the HepG2/C3A cell line. The viability results were most likely due to the increased phase II enzyme activity of HepG2/C3A cells

when compared with the L2 cell line. The HepG2 cells were presumably able to detoxify a larger amount of APAP via the glucuronide and sulfation pathways. The glutathione levels in each cell compartment correlated with the number of viable cells remaining after the 6 hour APAP dose (Figure 4.10B). Caco-2 cells remained viable and the monolayers remained intact after a 6-hour, 30 mM APAP exposure (data not shown).

The first generation chip and GI tract μCCAs provide a framework for studying oral drug absorption and metabolism, but the system has several limitations. The chip was designed to mimic first pass metabolism in that all fluid circulating through the GI tract goes directly to the liver, but is diluted with fluid pumped directly to the liver. In order to achieve this effect two pump channels and two μCCA chip inlets were necessary. The peristaltic pump can only be run at a single flowrate, therefore the amount of medium pumped through the basolateral side of the GI tract μCCA was higher than desired and resulted in residence times that did not match physiological values. If the channel pumping to the basolateral chamber could have been run at 0.5 μL/min, for example, the residence times in the basolateral chamber and liver chamber would have been much closer to *in vivo* values. The two-inlet design of the chip and the addition of the GI tract μCCA made it very difficult to assemble and run the devices without letting air into the system. Air bubbles in the system often caused leakage and/or loss of cell viability [48], and experimental results from systems with an excessive amount of air bubbles had to be discarded. This issue with air bubbles necessitated the short experimental time frame (there were fewer problems with air bubbles during shorter experiments) and high drug concentrations (more physiologically relevant APAP concentrations did not have a noticeable effect on cells after only 6 hours).

These problems led to several improvements that were incorporated into the

second generation μCCA system (Figures 4.4 and 4.5). The second generation chip μCCA was designed with one inlet and outlet to reduce the amount of air that enters the system, which allowed for longer experiments and more physiologically realistic APAP concentrations. Goblet-like, mucus secreting cells were incorporated into the GI tract μCCA membrane to better mimic the cell composition *in vivo*. HPLC was used to determine the APAP and metabolite concentrations at different time points throughout the experiment. Finally, *in vitro* digestion of APAP was performed and this chyme mimic was pumped through the apical chamber of the GI tract, which better re-creates the absorption conditions in the upper small intestine.

The results generated using the second generation GI tract and chip μCCAs demonstrate that liver and intestinal epithelial cells in the chip and GI tract μCCAs respond to APAP in a dose dependent manner for APAP in culture medium or chyme mimic (Figures 4.14, 4.15, 4.19, and 4.20). As the concentration of APAP in culture medium or chyme mimic circulated through the apical chamber of the GI tract μCCA increased, the viability of the liver cells and the glutathione levels of the liver and intestinal epithelial cells decreased. Some decrease in cell viability was due to ethanol, the APAP solvent, for the 30 mM concentration (Figure 4.23). The formation of APAP-GLUC appeared to be saturated even at the lowest APAP concentrations, but the formation of APAP-SULF increased with increasing APAP dose (Figures 4.17 and 4.21).

When APAP was circulated through the second generation apical GI μCCA chamber in MEM for 24 hours the concentrations of APAP in the apical chamber and basolateral/chip chamber reached near equilibrium after 24 hours for the 30 mM and 10 mM concentrations (Figure 4.17). For the 3 mM and 1 mM concentrations the apical concentration was significantly higher than the basolateral chamber/chip concentration after 24 hours (Figure 4.17). The time course experiment with 10 mM

APAP showed that the APAP concentrations in the two chambers did not reach equilibrium until after the 12 hour time point (Figure 4.18). In this system absorption of APAP most likely occurs via passive diffusion down a concentration gradient, therefore complete absorption would mean that the concentration in the apical chamber and basolateral chamber/chip are equal. *In vivo,* APAP is completely absorbed within 1 hour at therapeutic doses. Peak serum concentrations in acute overdose, however, may be delayed for up to four hours, which means that complete absorption would be expected within 5-6 hours [42]. Passively diffused drugs diffuse through the intestinal epithelium at a constant rate, and the transport of passively diffused drugs through Caco-2 monolayers has been shown to correlate well with *in vivo* data [49]. Therefore one likely reason that APAP takes 2-3 times longer to reach equilibrium in the μCCA is the lower amount of surface area available for absorption in the device when compared with the small intestine *in vivo*. In future work, the surface area available for absorption could easily be increased in the devices.

When APAP was circulated through the apical GI chamber in chyme mimic, the APAP concentration in the apical chamber and basolateral chamber/chip reached near equilibrium after 24 hours for all concentrations studied (Figure 4.21). The time course experiment with 10 mM APAP showed that the APAP concentrations in the two chambers reached equilibrium by approximately 12 hours (Figure 4.22). The most likely explanation for why the system reached equilibrium more quickly when digested APAP was used is that the chyme mimic slightly damaged the Caco-2/HT29-MTX monolayer. This may have compromised the tight junctions and resulted in more drug passing through the monolayer.

In conclusion, a prototype GI tract μCCA has been developed and used together with a chip μCCA to demonstrate digestion, absorption through the intestinal epithelium, and metabolism by the liver. The μCCA system can overcome many of the

drawbacks found in traditional drug testing methods. Multiple cell types and re-circulating medium allow researchers to analyze the absorption and the systemic effects of the compound being studied and the effects of its metabolites in a way that mimics the dynamic, time dependent changes in drug concentration and metabolites after oral administration. Human cells can be used in the μCCAs, offering a superior method for predicting a potential drug's effect on humans and sparing animals. The μCCAs are also inexpensive to produce and use very little of the compound of interest. The development and incorporation of a physiologically realistic GI tract μCCA may offer a new tool to help understand the kinetics of orally delivered drug ADMET, to aid in the development of oral delivery strategies, to help to find correct oral dosages for new pharmaceuticals, and to potentially better predict the systemic toxicity of orally delivered drugs.

REFERENCES

1. DiMasi JA, Hansen RW, Grabowski HG. 2003. The price of innovation: New estimates of drug development costs. *Journal of Health Economics*. 22(2):151.

2. Agres T. 2005. Finding blockbusters a struggle. *Drug Discovery & Development*. 8(3):16-19.

3. Sankar U. 2005. The delicate toxicity balance in drug discovery. *The Scientist*. 19(15):32-34.

4. Brown RP, Delp MD, Lindstedt SL, Rhomberg LR, Beliles RP. 1997. Physiological parameter values for physiologically based pharmacokinetic models. *Toxicology and Industrial Health*. 13(4):407-484.

5. Sin A, Chin KC, Jamil MF, Kostov Y, Rao G, Shuler ML. 2004. The design and fabrication of three-chamber microscale cell culture analog devices with integrated dissolved oxygen sensors. *Biotechnology Progress*. 20(1):338-345.

6. Viravaidya K, Sin A, Shuler ML. 2004. Development of a microscale cell culture analog to probe naphthalene toxicity. *Biotechnology Progress*. 20(1):316-323.

7. Viravaidya K, Shuler ML. 2004. Incorporation of 3T3-L1 cells to mimic bioaccumulation in a microscale cell culture analog device for toxicity studies. *Biotechnology Progress*. 20(2):590-597.

8. Bessems JGM, Vermeulen NPE. 2001. Paracetamol (acetaminophen)-induced toxicity: Molecular and biochemical mechanisms, analogues and protective approaches. *Critical Reviews in Toxicology*. 31(1):55-138.

9. Corcoran GB, Mitchell JR, Vaishnav YN, Horning EC. 1980. Evidence that acetaminophen and n-hydroxyacetaminophen form a common arylating intermediate, n-acetyl-para-benzoquinoneimine. *Molecular Pharmacology*. 18(3):536-542.

10. Patten CJ, Thomas PE, Guy RL, Lee MJ, Gonzalez FJ, Guengerich FP, Yang CS. 1993. Cytochrome-p450 enzymes involved in acetaminophen activation by rat and human liver-microsomes and their kinetics. *Chemical Research in Toxicology*. 6(4):511-518.

11. Mitchell JR, Jollow DJ, Potter WZ, Gillette JR, Brodie BB. 1973. Acetaminophen-induced hepatic necrosis. 4. Protective role of glutathione. *Journal of Pharmacology and Experimental Therapeutics*. 187(1):211-217.

12. Qiu YC, Benet LZ, Burlingame AL. 1998. Identification of the hepatic protein targets of reactive metabolites of acetaminophen *in vivo* in mice using two-dimensional gel electrophoresis and mass spectrometry. *Journal of Biological*

Chemistry. 273(28):17940-17953.

13. Lee WM. 1995. Medical progress - drug-induced hepatotoxicity. *New England Journal of Medicine*. 333(17):1118-1127.

14. Lesuffleur T, Barbat A, Dussaulx E, Zweibaum A. 1990. Growth adaptation to methotrexate of HT-29 human colon-carcinoma cells is associated with their ability to differentiate into columnar absorptive and mucus-secreting cells. *Cancer Research*. 50(19):6334-6343.

15. Donato MT, Gomezlechon MJ, Castell JV. 1993. A microassay for measuring cytochrome-p450IA1 and cytochrome-p450IIB1 activities in intact human and rat hepatocytes cultured on 96-well plates. *Analytical Biochemistry*. 213(1):29-33.

16. Donato MT, Klocke R, Castell JV, Stenzel K, Paul D, Gomez-Lechon MJ. 2003. Constitutive and inducible expression of CYP enzymes in immortal hepatocytes derived from SV40 transgenic mice. *Xenobiotica*. 33(5):459-473.

17. Dicker E, McHugh T, Cederbaum AI. 1990. Increased oxidation of para-nitrophenol and aniline by intact hepatocytes isolated from pyrazole-treated rats. *Biochimica et Biophysica Acta*. 1035(3):249-256.

18. Bradford MM. 1976. Rapid and sensitive method for quantitation of microgram quantities of protein utilizing principle of protein-dye binding. *Analytical Biochemistry*. 72(1-2):248-254.

19. Kautzky F, Hartinger A, Kohler LD, Vogt H-J. 1996. *In vitro* cytotoxicity of antimicrobial agents to human keratinocytes. *Journal of the European Academy of Dermatology and Venereology*. 6(2):159-166.

20. Chai JN, Lu FZ, Li BM, Kwok DY. 2004. Wettability interpretation of oxygen plasma modified poly(methyl methacrylate). *Langmuir*. 20(25):10919-10927.

21. Glahn RP, Lee OA, Yeung A, Goldman MI, Miller DD. 1998. Caco-2 cell ferritin formation predicts nonradiolabeled food iron availability in an *in vitro* digestion/Caco-2 cell culture model. *Journal of Nutrition*. 128(9):1555-61.

22. Wang EJ, Li Y, Lin M, Chen LS, Stein AP, Reuhl KR, Yang CS. 1996. Protective effects of garlic and related organosulfur compounds on acetaminophen-induced hepatotoxicity in mice. *Toxicology and Applied Pharmacology*. 136(1):146-154.

23. Poulin P, Theil FP. 2002. Prediction of pharmacokinetics prior to *in vivo* studies. 1. Mechanism-based prediction of volume of distribution. *Journal of Pharmaceutical Sciences*. 91(1):129-156.

24. Watari N, Iwai M, Kaneniwa N. 1983. Pharmacokinetic study of the fate of acetaminophen and its conjugates in rats. *Journal of Pharmacokinetics and Biopharmaceutics*. 11(3):245-272.

25. Hopkinson D, Bourne R, Barile FA. 1993. *In vitro* cytotoxicity testing - 24-hour and 72-hour studies with cultured lung cells. *Atla-Alternatives To Laboratory Animals*. 21(2):167-172.

26. Shi MM, Kugelman A, Iwamoto T, Tian L, Forman HJ. 1994. Quinone-induced oxidative stress elevates glutathione and induces gamma-glutamylcysteine synthetase-activity in rat lung epithelial L2 cells. *Journal of Biological Chemistry*. 269(42):26512-26517.

27. Hewitt NJ, Hewitt P. 2004. Phase I and II enzyme characterization of two sources of HEPG2 cell lines. *Xenobiotica*. 34(3):243-256.

28. Hidalgo IJ, Raub TJ, Borchardt RT. 1989. Characterization of the human-colon carcinoma cell-line (Caco-2) as a model system for intestinal epithelial permeability. *Gastroenterology*. 96(3):736-749.

29. Artursson P, Karlsson J. 1991. Correlation between oral drug absorption in humans and apparent drug permeability coefficients in human intestinal epithelial (Caco-2) cells. *Biochemical and Biophysical Research Communications*. 175(3):880-885.

30. Basson MD, Turowski G, Emenaker NJ. 1996. Regulation of human (Caco-2) intestinal epithelial cell differentiation by extracellular matrix proteins. *Experimental Cell Research*. 225:301-305.

31. Borlak J, Zwadlo C. 2003. Expression of drug-metabolizing enzymes, nuclear transcription factors, and abc transporters in Caco-2 cells. *Xenobiotica*. 33(9):927-943.

32. Prueksaritanont T, Gorham LM, Hochman JH, Tran LO, Vyas KP. 1996. Comparative studies of drug-metabolizing enzymes in dog, monkey, and human small intestine cells, and in Caco-2 cells. *Drug Metabolism and Disposition*. 24(6):634-642.

33. Baranczykkuzma A, Garren JA, Hidalgo IJ, Borchardt RT. 1991. Substrate-specificity and some properties of phenol sulfotransferase from human intestinal Caco-2 cells. *Life Sciences*. 49(16):1197-1206.

34. Nestorov IA, Aarons LJ, Arundel PA, Rowland M. 1998. Lumping of whole-body physiologically based pharmacokinetic models. *Journal of Pharmacokinetics and Biopharmaceutics*. 26(1):21-46.

35. Lee HJ. 2002. Protein drug oral delivery: The recent progress. *Archives of*

Pharmaceutical Research. 25(5):572-584.

36. Lampen A, Bader A, Bestmann T, Winkler M, Witte L, Borlak JT. 1998. Catalytic activities, protein- and mRNA-expression of cytochrome p450 isoenzymes in intestinal cell lines. *Xenobiotica*. 28(5):429-441.

37. Doherty MM, Charman WN. 2002. The mucosa of the small intestine: How clinically relevant as an organ of drug metabolism? *Clinical Pharmacokinetics*. 41(4):235-253.

38. Rang HP, Dale MM, Ritter JM. 1999. Pharmacology. 4th ed. Edinburgh: Churchill Livingston.

39. Forstner JF, Forstner GG. 1994. Gastrointestinal mucus. Johnson LR, editor. Physiology of the gastrointestinal tract, 3rd ed. New York: Raven Press.

40. Artursson P, Palm K, Luthman K. 2001. Caco-2 monolayers in experimental and theoretical predictions of drug transport. *Advanced Drug Delivery Reviews*. 46(1-3):27-43.

41. Audus KL, Bartel RL, Hidalgo IJ, Borchardt RT. 1990. The use of cultured epithelial cells for drug transport and metabolism studies. *Pharmaceutical Research*. 7(5):435-451.

42. Kociancic T, Reed MD. 2003. Acetaminophen intoxication and length of treatment: How long is long enough? *Pharmacotherapy*. 23(8):1052-1059.

43. Rumack BH, Matthew H. 1975. Acetaminophen poisoning and toxicity. *Pediatrics*. 55(6):871-876.

44. Mitchell JR, Jollow DJ, Potter WZ, Davis DC, Gillette JR, Brodie BB. 1973. Acetaminophen-induced hepatic necrosis.1. Role of drug-metabolism. *Journal of Pharmacology and Experimental Therapeutics*. 187(1):185-194.

45. Dimova S, Hoet PHM, Nemery B. 2001. Xenobiotic-metabolizing enzyme activities in primary cultures of rat type II pneumocytes and alveolar macrophages. *Drug Metabolism and Disposition*. 29(10):1349-1354.

46. Baudouin SV, Howdle P, Ogrady JG, Webster NR. 1995. Acute lung injury in fulminant hepatic-failure following paracetamol poisoning. *Thorax*. 50(4):399-402.

47. Dimova S, Hoet PHM, Nemery B. 2000. Paracetamol (acetaminophen) cytotoxicity in rat type II pneumocytes and alveolar macrophages *in vitro*. *Biochemical Pharmacology*. 59(11):1467-1475.

48. Sin A, Reardon CF, Shuler ML. 2004. A self-priming microfluidic diaphragm

pump capable of recirculation fabricated by combining soft lithography and traditional machining. *Biotechnology and Bioengineering*. 85(3):359-363.

49. Lennernas H, Palm K, Fagerholm U, Artursson P. 1996. Comparison between active and passive drug transport in human intestinal epithelial (Caco-2) cells *in vitro* and human jejunum *in vivo*. *International Journal of Pharmaceutics.* 127:103-107.

CHAPTER 5

CONCLUSIONS AND RECOMMENDATIONS

5.1. Conclusions

Our group has developed an *in vitro* cell culture model of the gastrointestinal tract that includes digestion, physiologically realistic cell populations, and a mucus layer. The applications of this model include predicting iron bioavailability, studying the effects of oral exposure to nanoparticles, and measuring the metabolism and toxicity of ingested chemicals or drugs.

Co-cultures of Caco-2 and HT29-MTX represent the two major cell types found in the human intestinal epithelium. HT29-MTX cells form a physiologically realistic mucus layer that may interact with food digests and influence iron bioavailability predictions. In preliminary studies, increasing ratios of HT29-MTX cells decreased the amount of ferritin formation in high available iron digests such as those containing ferrous iron, heme iron, and whole ferritin molecules. For low available iron digests, which present iron to the cells in mostly ferric form, increasing the ratio of HT29-MTX cells had no effect on ferritin formation. The physiologically relevant ratios of 90:10 and 75:25 (Caco-2:HT29-MTX) offer the best compromise between model response and the presence of a mucus layer.

A physiologically realistic, cell culture model of the intestinal epithelium was used to study the sublethal effects of oral nanoparticle exposure. Iron, which is an essential nutrient that is transported across the intestinal epithelium via complex, highly regulated, protein-assisted vesicular and nonvesicular mechanisms, was chosen as a model compound. These preliminary results suggest that nanoparticle size,

concentration, and charge influence iron uptake and transport after oral exposure. Low doses ($2x10^9$ 50 nm particles/mL or $1.25x10^8$ 200 nm particles/mL) of carboxylated, non-ionized, or aminated particles had no effect on iron uptake and transport. Mid doses of 50 nm carboxylated particles ($2x10^{11}$ particles/mL) did not influence iron uptake, but significantly decreased iron transport in Caco-2/HT29-MTX monolayers. Mid doses of 200 nm carboxylated particles ($1.25x10^{10}$ particles/mL) also did not affect iron uptake, but significantly decreased iron transport in +M cells monolayers. High doses of 50 nm carboxylated particles ($2x10^{13}$ particles/mL) increased iron uptake and transport in Caco-2/HT29-MTX and +M cells monolayers. High doses of 200 nm carboxylated particles ($1.25x10^{12}$ particles/mL) significantly decreased iron uptake in Caco-2/HT29-MTX monolayers and increased iron transport in Caco-2/HT29-MTX and +M cells monolayers. Mid doses of non-ionized 50 nm and 200 nm particles and 200 nm aminated particles had no effect on iron uptake or transport. Aminated, 50 nm particles at mid doses increased iron uptake in Caco-2/HT29-MTX and +M cells monolayers and increased iron transport in Caco-2/HT29-MTX monolayers.

A GI tract μCCA has been developed and used together with a chip μCCA in proof of concept experiments to demonstrate digestion, absorption through the intestinal epithelium, and metabolism by the liver. With the GI tract and chip μCCA system we describe a prototype *in vitro* method that for the first time, although at a very basic level, mimics oral exposure to a drug, first pass metabolism, and the circulation of metabolites on a micron-sized scale. These results demonstrate that APAP crosses the Caco-2/HT29-MTX cell monolayer and is metabolized by HepG2 liver cells, resulting in liver cell toxicity.

5.2. Recommendations

5.2.1. Caco-2 and HT29-MTX co-cultures used for iron bioavailability studies

For future studies with Caco-2 and HT29-MTX co-cultures in the *in vitro* digestion/cell culture model, it is recommended that the physiologically realistic ratios of 90:10 and 75:25 (Caco-2:HT29-MTX) are used. These ratios offer the best compromise between model response and the presence of a mucus layer. In digests with low available iron there was very little difference in cell ferritin formation between Caco-2 monolayers and co-cultures (Figure 2.9), and it is unclear if the minor differences between Caco-2 and co-cultures in low iron bioavailability conditions mean that the cells present absorb all available iron or that the mucus layer in the co-cultures aids in iron absorption and helps to compensate for the lack of Caco-2 cells. Experiments in the future studying the effects of co-cultures in the presence of iron absorption inhibitors such as tannic acid could help to determine if the mucus layer aids in iron absorption from low available iron digests.

Experiments characterizing the *in vitro* digestion/co-culture culture model without 15,000 MWCO dialysis membrane inserts were performed in an effort to make model conditions closer to those *in vivo*. The 15,000 MWCO dialysis membranes are used to protect the cell monolayers from digestive enzymes in samples, but also add an artificial barrier to iron absorption. In these experiments the cells were exposed to the chyme mimic for 24 hours, and it was hypothesized that the mucus layer would mimic its function *in vivo* and protect the cell monolayer from digestive enzymes. Dilution of the digests with culture medium by a factor of 5.5 increased cell survival, but overall the changes in cell ferritin formation after direct exposure to digest were most likely due to cell damage. In the small intestine, there is a loosely adherent mucus layer and a layer that is firmly attached to the mucosa that is

approximately 15 μm thick in the human duodenum [1, 2]. The mucus layer formed by HT29-MTX cells is about 10 μm thick (Figure 2.1) and mimics the firmly adherent mucus layer *in vivo*. Co-cultures of Caco-2 and HT29-MTX and the addition of porcine mucin to the culture medium may better recreate *in vivo* conditions (i.e. the loosely and firmly adherent mucus layers) and allow for *in vitro* digestion/iron bioavailability experiments without the 15,000 MWCO inserts.

The bacterial community in the gastrointestinal tract has been shown to play a major role in host health. Bacterial functions include metabolic activities that result in the recovery of energy and absorbable nutrients, important trophic effects on intestinal epithelial cells and on immune structure and function, and the protection of the host against pathogenic microbes [3]. Bacteria have also been shown to modulate gene expression related to nutrient absorption, mucosal barrier fortification, xenobiotic metabolism, angiogenesis, and postnatal intestinal maturation [4]. Future work with the *in vitro* digestion/co-culture model could benefit from including gut flora due to the role of bacteria in nutrient absorption gene expression and absorbable nutrient recovery.

5.2.2. In vitro models for the evaluation of oral nanoparticle exposure toxicity

This *in vitro* intestinal epithelial model used to study the effects of nanoparticle exposure provides a new tool to assess nanoparticle toxicity following ingestion, new metrics for measuring sublethal effects, and new data on the relationship between physicochemical properties of nanoparticles and their ability to disrupt cellular behavior. Similar disruptions in nutrient absorption could be possible with other inorganic elements such as calcium, copper, and zinc that require passive or active transport systems to be absorbed through the intestinal epithelium. Fat-soluble vitamins such as vitamins A, D, E, and K are absorbed only after micellization by

pancreatic lipase [5]. The micelles, due to their small size and hydrophilic surface, are able to gain proximity to the brush border and facilitate the diffusion of their contents into the phospholipid membrane of the epithelial layer. Hydrophobic, charged nanoparticles could potentially disrupt the formation of micelles, micelle interactions with the epithelial layer, and nutrient diffusion through the phospholipids layer. Interesting future studies would use the *in vitro* digestion/co-culture model for predicting iron bioavailability to study uptake of other inorganic elements (calcium, copper, or zinc) or fat soluble vitamins (A, D, E, and K) in the presence of nanoparticles. This work could help to determine if nanoparticle exposure affects the absorption of additional nutrients. The *in vitro* digestion/Caco-2 model has been used in the past to predict cartenoid, copper, calcium, and zinc bioavailability.

Orally delivered nanoparticles have been shown to be taken up into the liver, spleen, blood, and bone marrow of rats [6]. Copper nanoparticles, but not copper microparticles, have also been shown to be toxic to mice after oral exposure; the kidney, liver, and spleen were found to be target organs of the copper nanoparticles [7]. These is very little data on the effects of oral exposure to nanoparticles, and the GI tract μCCA coupled with the chip μCCA offers an excellent tool to rapidly screen nanoparticles for toxic effects. The second generation chip μCCA was designed with a kidney, liver, fat, and bone marrow compartment to mimic the potential target toxicity and storage sites for nanoparticles.

The *in vitro* intestinal epithelium model with mucus and M cells could also be used to study the mechanical effects (i.e. effects on tight junctions) of pathogenic bacteria exposure. Studies with pathogenic bacteria and specific virulence factors indicate four major mechanisms by which these pathogens may act on tight junctions: direct cleavage of tight junctional structural proteins, modification of the actin cytoskeleton, activation of cellular signal transduction, and triggering transmigration

of polymorphonuclear cells across the epithelial cell barrier [8]. The intestinal epithelium model offers a physiologically realistic, high throughput method for evaluating the effects of pathogenic bacteria exposure, although the addition of a bacteriostatic antibiotic such as tetracycline to the culture medium would be necessary to inhibit the bacterial growth and prevent complete bacterial contamination of the mammalian/bacterial co-cultures. New therapeutics or better drug delivery methods could be developed from studies of these pathogens and the cellular processes and proteins they disrupt.

5.2.3. GI tract μCCA for studying orally administered compound ADMET

Experiments with APAP and the GI tract and chip μCCAs showed that the passively diffused drug took longer to completely absorb in the *in vitro* system when compared with *in vivo* data; the μCCA took approximately 12 hours to equilibrate, while complete absorption in acute overdose is expected within 5 hours [9]. It is likely that the reason APAP takes 2-3 times longer to reach equilibrium in the μCCA is the lower amount of surface area available for absorption in the device when compared with the small intestine *in vivo*. The Caco-2 cells express microvilli, which increase the absorptive surface area by about 20 times, but cannot form folds or villi [10]. In future work, the surface area available for absorption in the GI tract μCCA should be increased several fold to better mimic *in vivo* conditions. This can be done easily by modifying the size of the apical and basolateral chambers in the GI tract μCCA. If the entire Snapwell membrane holding Caco-2 and HT29-MTX cells were exposed to flow, for example, the surface area available for absorption would increase by a factor of ~18 (0.062 cm^2 to 1.12 cm^2).

Future improvements to the GI tract μCCA could include the addition of peristalsis. The intestinal mucosa is repetitively subjected to physical forces that

induce deformation. These forces include villous motility, peristaltis, segmentation, and pressure and shear stress generated by the movement of the luminal contents [11]. Previous studies have shown that cyclic strain with an amplitude (10% strain) and frequency (10 deformations per minute) similar to those seen *in vivo* induce Caco-2 cell proliferation, differentiation, and intracellular signaling [11]. Laminar shear flow over HT29 colon carcinoma monolayers has been shown to influence cellular functions including cell morphology, cytoskeletal arrangements, and intracellular signaling [12]. To date, no *in vitro* permeability data has been published for devices that incorporate cyclic strain or both shear flow and cyclic strain.

Figure 5.1. The GI tract μCCA that includes cyclic strain and shear flow and is based on the micropump developed by Sin et al. [13].

A GI tract μCCA that includes cyclic strain and based on the micropump developed by Sin et al. has been fabricated (Figure 5.1) [13]. The top piece, which makes up the pump chamber, is machined poly-methylemethacrylate (PMMA). The next layer is a sheet of poly-dimethylsiloxane (PDMS). The center spacer is machined PMMA that will allow for shear flow to pass over a Caco-2 cell monolayer. The fourth layer is a microporous, PDMS membrane onto which Caco-2 cells are cultured. The bottom piece, which comprises the valve seats and connecting channels, is machined PMMA. Synthetic ruby balls sit in the valve seats to form one-way check valves. The

μCCA is actuated using oscillating air pressure controlled by a three-way solenoid valve. A syringe pump provides physiologically realistic shear flow over the Caco-2 monolayer within the device, and the movement of the diaphragm will provide cyclic strain. The device will also pump at flow rates (~3.5 μL/min) compatible with the other μCCA devices being developed. When the GI tract μCCA is connected with a chip μCCA that mimics the other tissues and organs in the body, the GI tract μCCA will be capable of re-circulating culture medium through the system, eliminating the need for an external peristaltic pump. Preliminary experiments have been performed with this device, but more extensive characterization studies are necessary [14].

Other improvements to the GI tract μCCA could include the addition of gut flora and variations in pH, which would better mimic *in vivo* conditions. After improvements have been made, the next recommended level of validation for the system would be a direct comparison between the μCCA system and animals for drug, chemical, or nanoparticle absorption, distribution, metabolism, elimination, and toxicity (ADMET).

REFERENCES

1. Atuma C, Strugala V, Allen A, Holm L. 2001. The adherent gastrointestinal mucus gel layer: Thickness and physical state *in vivo*. *American Journal of Physiology-Gastrointestinal and Liver Physiology*. 280(5):G922-G929.

2. Newton JL, Jordan N, Pearson J, Williams GV, Allen A, James OFW. 2000. The adherent gastric antral and duodenal mucus gel layer thins with advancing age in subjects infected with helicobacter pylori. *Gerontology*. 46(3):153-157.

3. Guarner F, Malagelada J-R. 2003. Gut flora in health and disease. *The Lancet*. 361(9356):512.

4. Hooper LV, Wong MH, Thelin A, Hansson L, Falk PG, Gordon JI. 2001. Molecular analysis of commensal host-microbial relationships in the intestine. *Science*. 291(5505):881-884.

5. Basu TK, Donaldson D. 2003. Intestinal absorption in health and disease: Micronutrients. *Best Practice & Research Clinical Gastroenterology*. 17(6):957-79.

6. Jani P, Halbert GW, Langridge J, Florence AT. 1989. The uptake and translocation of latex nanospheres and microspheres after oral-administration to rats. *Journal of Pharmacy and Pharmacology*. 41(12):809.

7. Chen Z, Meng HA, Xing GM, Chen CY, Zhao YL, Jia GA, Wang TC, Yuan H, Ye C, Zhao F and others. 2006. Acute toxicological effects of copper nanoparticles *in vivo*. *Toxicology Letters*. 163(2):109-120.

8. Sears CL. 2000. Molecular physiology and pathophysiology of tight junctions v. Assault of the tight junction by enteric pathogens. *American Journal of Physiology-Gastrointestinal and Liver Physiology*. 279(6):G1129-1134.

9. Kociancic T, Reed MD. 2003. Acetaminophen intoxication and length of treatment: How long is long enough? *Pharmacotherapy*. 23(8):1052-1059.

10. DeSesso JM, Jacobson CF. 2001. Anatomical and physiological parameters affecting gastrointestinal absorption in humans and rats. *Food and Chemical Toxicology*. 39(3):209-228.

11. Zhang J, Li W, Sumpio BE, Basson MD. 2003. Fibronectin blocks p38 and jnk activation by cyclic strain in Caco-2 cells. *Biochemical and Biophysical Research Communications*. 306:746-749.

12. Haier J, Nicolson GL. 1999. Role of cytoskeleton in adhesion stabilization of human colorectal carcinoma cells to extracellular matrix components under

dynamic conditions of laminar flow. *Clinical & Experimental Metastasis*. 17:713-721.

13. Sin A, Reardon CF, Shuler ML. 2004. A self-priming microfluidic diaphragm pump capable of recirculation fabricated by combining soft lithography and traditional machining. *Biotechnology and Bioengineering*. 85(3):359-363.

14. Kung F. 2007. Effects of shear flow and cyclic strain on drug diffusion through Caco-2 monolayers [Master of Engineering]. Ithaca: Cornell University, Department of Biomedical Engineering.

APPENDIX A

DEVELOPMENT OF AN *IN VITRO* MODEL OF IRON TRANSPORT INCLUDING THE IRON REGULATING PROTEIN HEPCIDIN

A.1. Introduction

In some cases, absorption of compounds through the intestinal epithelium is regulated by feedback mechanisms. Iron is an essential nutrient in the body that is absorbed from food through the intestinal epithelium, but there is a delicate balance between iron absorption, utilization, and loss in the human body. An excess of systemic iron exceeds the capacity of the proteins that sequester it and catalyzes the formation of free radicals [1]. Free radicals go on to attack cell membranes, proteins, and DNA, causing tissue damage [2]. A lack of iron, on the other hand, results in anemia, which is characterized by not having enough hemoglobin to adequately oxygenate tissues [2]. Because the body has no significant mechanism for getting rid of excess iron, iron balance is dependent on tightly linking body iron requirements with intestinal iron absorption from food.

Hepcidin, a recently discovered, liver-produced protein, has been shown to be the principle protein involved in iron regulation [3]. Intestinal iron absorption increases with decreased iron stores, increased erythropoietic activity in bone marrow, anemia, or hypoxia [3]. Iron absorption decreases in the presence of inflammation [3]. Each of these previously mentioned factors also regulate the expression of hepcidin. Intestinal iron absorption varies inversely with liver hepcidin expression and the protein also causes rapid sequestration of iron by reticuloendothelial cells and the liver [3].

In the small intestinal enterocyte, dietary iron is reduced to the ferrous state (Fe^{3+} to Fe^{2+}) by duodenal ferric reductase (Dcytb), transported into the cell by divalent metal iron transporter 1 (DMT1), and stored within the cell as ferritin [3]. Iron is released by ferroportin into circulation and oxidized by hephaestin [3]. Iron is normally bound in the blood stream by the iron transport protein transferrin. Hepatocytes take up iron from the circulation as wither free iron or transferrin-bound iron through transferrin receptors 1 and 2. Transferrin receptor 2 (TFR2) may serve as a sensor of circulating transferrin-bound iron and influence the expression of hepcidin, as decreased hepcidin expression has been observed when the gene for TFR2 is mutated [4]. Hepcidin response is also controlled by HFE (a gene that when mutated is responsible for Type 1 hereditary hemochromatosis, an iron overload disease) and HJV (a gene that when mutated is responsible for Type 2 hereditary hemochromatosis) [5]. Hepcidin is secreted into circulation, where it down-regulates ferroportin iron release from enterocytes, macrophages, and hepatocytes [6]. IL-6, a mediator of inflammation, also induces hepcidin secretion, making hepcidin an acute-phase protein (any protein whose plasma concentration increases or decreases by 25% or more during certain inflammatory disorders) [7]. The sequestering of iron caused by hepcidin makes iron less available to microorganisms for use as a growth factor. Hepcidin has also been shown to have chemotherapeutic activity; the protein acts similarly to defensins and disrupts the bacterial membrane [8]. The hepcidin signaling pathway activated by IL-6 is not known, but Lee, et al. showed that mice homozygous for targeted HFE disruption and TFR2 mutation produced hepcidin in response to endotoxin injection [9]. The isolated hepatocytes of HFE and TFR2 knockout mice also produced hepcidin in response to IL-6 exposure. These results indicate that the IL-6-induced hepcidin signaling pathway does not require HFE or TFR2.

A method for measuring iron transport through Caco-2 monolayers was

developed by Gangloff et al. [10]. The effects of the iron status (i.e. iron loaded or iron deficient) of the cells and of iron chelators were tested. Gangloff et al. designed their experiments based on *in vivo* data of intestinal iron absorption showing that iron transport increases in iron deficient patients, including those with iron deficiency anemia and hypoxia [2]. Chelators bind iron ions and keep iron in solution, and some chelators, such as ascorbic acid (AA), reduce iron from Fe^{3+} to Fe^{2+}, the latter of which is the more absorbable form [10]. This reduction circumvents the need for Dcytb to reduce the iron before transport into the cell by DMT1 and aids in iron absorption. In the experiments, Caco-2 cells were plated onto Transwell® inserts and grown for a period of 15 days with normal culture medium containing fetal bovine serum. The cells were then given serum free medium with iron supplements varying in molarity and with varying chelators. It was expected that more iron would be taken up and transported in the iron-deficient cells and the cells exposed to iron absorption-enhancing chelators. Gangloff et al. found that iron uptake followed physiological trends, but iron transport was not related to iron status or chelator. The lack of effect of iron status on iron transport, which does not agree with known physiological response, led the researchers to believe that the Caco-2 monolayers alone may be inadequate for iron transport studies [10].

Munoz-Galarza compared iron transport and uptake in Transwell inserts to iron transport and uptake in a dynamic, laminar flow system [11]. In stagnant Transwell cultures, Munoz-Galarza found a significant difference between iron transport and uptake in iron loaded and iron deficient Caco-2 cells. In the laminar flow device, however, there was a significant difference between iron loaded and iron deficient cells only for iron uptake [11]. The iron regulatory protein hepcidin most likely accounts for the *in vitro-in vivo* discrepancies in the previous two *in vitro* iron transport models.

The role of hepcidin on *in vitro* iron absorption can be investigated by exposing Caco-2 and Hep3B co-cultures to iron loaded conditions, iron deficient conditions, IL-6, or hepcidin before performing iron transport studies. This could result in a more physiologically accurate model of iron absorption, and experiments of this type have never been reported. Caco-2 cells express the Dcytb, DMT1, ferroportin, and hephaestin proteins [12]. Caco-2 cells also store intracellular iron within the iron storage protein ferritin [12]. Hep3B cells have been shown to express the mRNA for hepcidin [13].

A.2. Material and Methods

A.2.1. Chemicals, enzymes, and hormones

All chemicals, enzymes, and hormones were purchased from Sigma Chemical Company (St. Louis, MO) unless otherwise stated. All glassware used in sample preparation and analysis was washed, soaked in 10% hydrochloric acid (HCl) and 10% nitric acid overnight, and rinsed with 18 MΩ water to avoid iron contamination.

A.2.2. Cell culture

Caco-2 and Hep3B (American Type Culture Collection, Manassas, VA) were routinely cultured as described for Caco-2 and HepG2/C3A in section 3.2.2. Caco-2 cells were seeded into 8 μg/cm^2 Type I collagen-coated (Becton Dickinson, Bedford, MA), 0.4 μm pore size, 24 mm polycarbonate Transwell inserts (Corning Life Sciences, Corning, NY) at a concentration of 100,000 cells/cm^2. Hep3B cells were seeded onto the 8 μg/cm^2 Type I collagen-coated bottom of a separate 6 well plate at a concentration of 20,000 cells/cm^2. After 1 day, half of the Caco-2 Transwells were moved into the Hep3B plates. DMEM with FBS was used in the apical chamber and MEM with FBS was used in the basolateral chamber for 14 days. On day 14, very low

iron (<8 μg Fe/L) MEM (see section 3.2.2. for low iron medium description) was added to the top chamber of the inserts and low iron MEM was added to the lower compartment with one of the following treatments: unsupplemented (low iron MEM only), +66 uM iron as Fe-NTA (nitrilotriacetic acid disodium salt) in a 1:2 molar ratio, +66 uM iron as holo-transferrin (iron saturated transferrin), 20 ng/mL IL-6 (R&D Systems, Minneapolis, MN), or 10 μm hepcidin (Peptides International, Louisville, KY). The unsupplemented treatment provides an iron deficient condition, Fe-NTA provides an iron overload condition that mimics plasma iron exceeding the capacity of transferrin, holo-transferrin provides an additional iron overload condition and may also interact with TFR2, IL-6 treatment mimics inflammation, and hepcidin is the iron regulatory protein. Medium containing the same treatments was renewed on day 15 and iron uptake and transport experiments were performed on day 16. Apical and basolateral culture medium was saved on days 14, 15 and 16 for later analysis with a Pro-hepcidin ELISA kit (DRG International, Inc., Mountainside, NJ) or mass spectrometry.

A.2.3. TER measurement

TER was measured as described in section 3.2.3 with an ENDOHM-24 SNAP chamber from World Precision Instruments (Sarasota, FL). Inserts with a TER of 450-650 Ω/cm^2 were used in experiments.

A.2.4. ^{59}Fe uptake and transport experiments

Iron uptake and transport experiments were performed as described in section 3.2.5.

A.3. Results

Figure A.1 compares the results of iron transport through Caco-2 monolayers

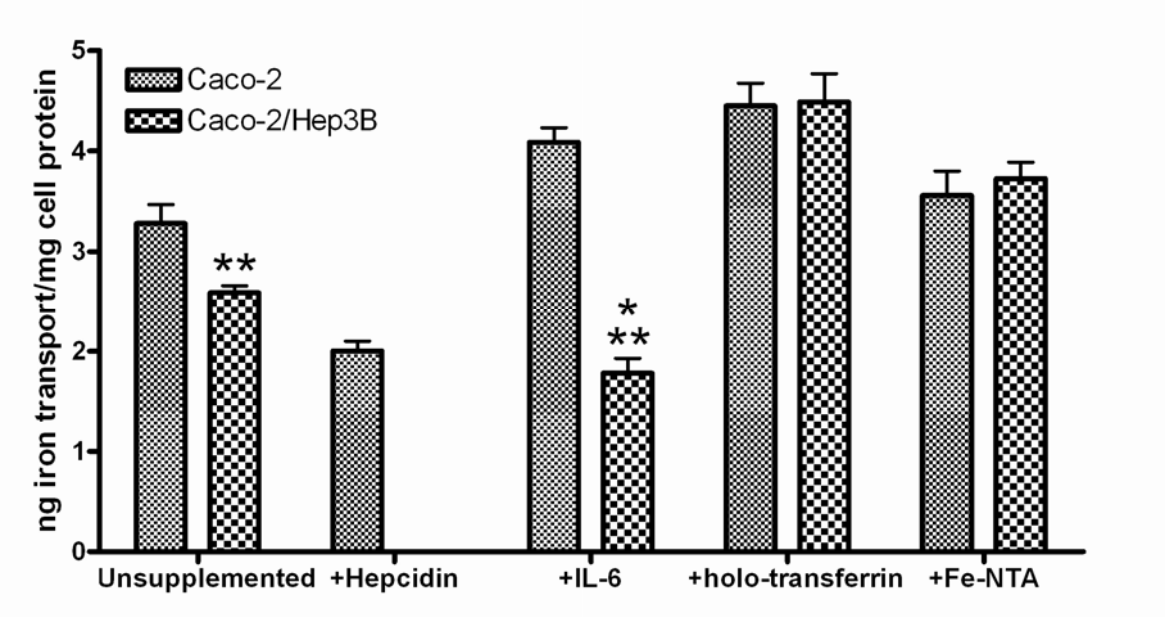

Figure A.1. Caco-2 and Caco-2/Hep3B iron transport results. Differences between Caco-2 and co-culture transport that are significant are indicated with a *. Differences between unsupplemented and +IL-6 co-culture treatments that are significant are indicated with a **. Statistical significance between treatments was determined with Turkey's pairwise comparison test with a family error rate of 0.05 (n = 6, n = 3 for hepcidin treatment).

to Caco-2 monolayers co-cultured with Hep3B cells. The experiment was based on the hypothesis that Hep3B cells would upregulate hepcidin production in response to iron overload and inflammation conditions, which would then decrease iron transport. The IL-6 treatment was the only condition where the amount of iron transported by the Caco-2 and Caco-2/Hep3B co-culture treatments was statistically different. In addition, the unsupplemented co-culture transported a significantly higher amount of iron than the IL-6-treated co-culture and the IL-6 treatment iron transport was statistically the same as iron transport in wells treated with 10 μm hepcidin. The decrease in iron transport for co-cultures exposed to IL-6 could be caused by hepcidin binding to the ferroportin iron efflux protein and inhibiting iron transport. These results agree with data collected by Nemeth et al. and Lin et al., who showed that hepcidin mRNA transcription in Hep3B cells is up-regulated in response to IL-6 but not to Fe-NTA or holo-transferrin [13, 14]. Lin et al. concluded that up regulation of

hepcidin expression by iron loading requires intact hepatic architecture or extrahepatic signals [14].

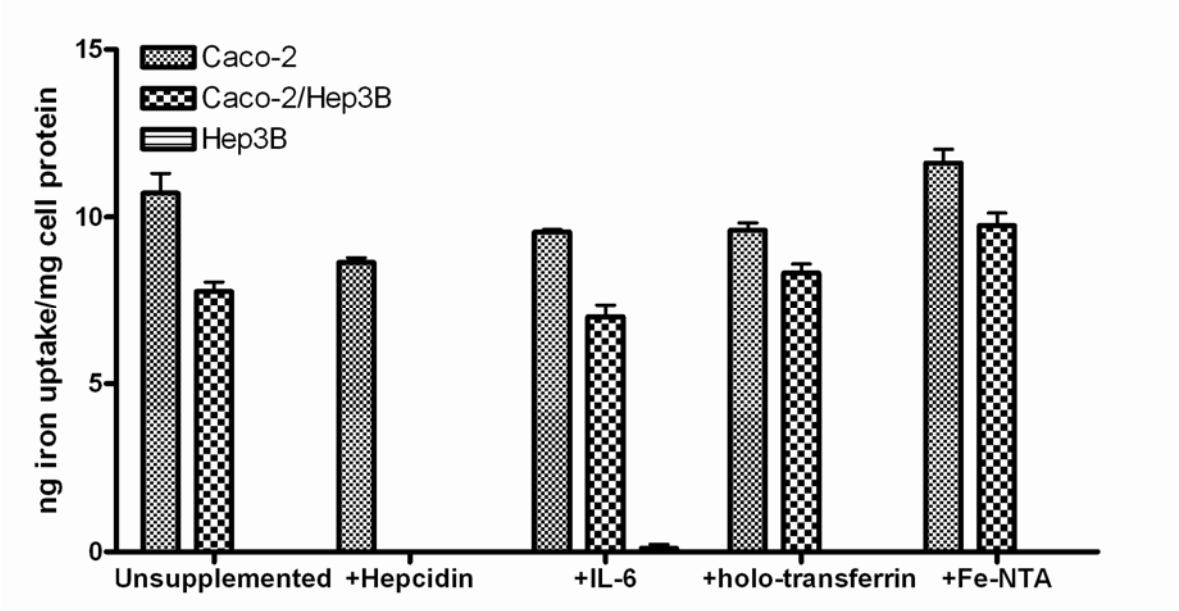

Figure A.2. Caco-2, Caco-2/Hep3B, and Hep3B iron uptake results. Differences between Caco-2 and Caco-2/Hep3B uptake that are significant according to Turkey's pairwise comparison test with a family error rate of 0.05 are indicated with a * (n = 6, n = 3 for hepcidin treatment).

Figure A.2 shows the iron uptake results. In all cases the co-cultures took up less iron than the Caco-2 monolayers. Figure A.3 shows the ferritin formation for all cell types at each treatment. In the Fe-NTA and holo-transferrin treatments the co-cultured Caco-2 cells display more iron loading the Caco-2 cells cultured alone. The Hep3B cells show very high ferritin formation after the addition of Fe-NTA. This behavior is expected, as liver cells are a major iron storage site *in vivo*. The increased iron loading and decreased ^{59}Fe uptake in the co-cultures is most likely the result of excess stored iron in the liver cells. This could indicate that the Hep3B cells are responding to the iron status of the medium by releasing iron stores when the medium becomes iron deficient.

The uptake of iron by Caco-2 cultures is similar for all treatments. The co-cultures show the same behavior. Uptake was high for both iron loaded and iron

deficient treatments because the $^{59}FeCl_3$ delivered to the cells was chelated with ascorbic acid. AA is a reducing agent that enhances iron absorption. AA was used as a chelator to maximize iron uptake and the amount of iron available for transport, which would presumably make differences in transport more apparent.

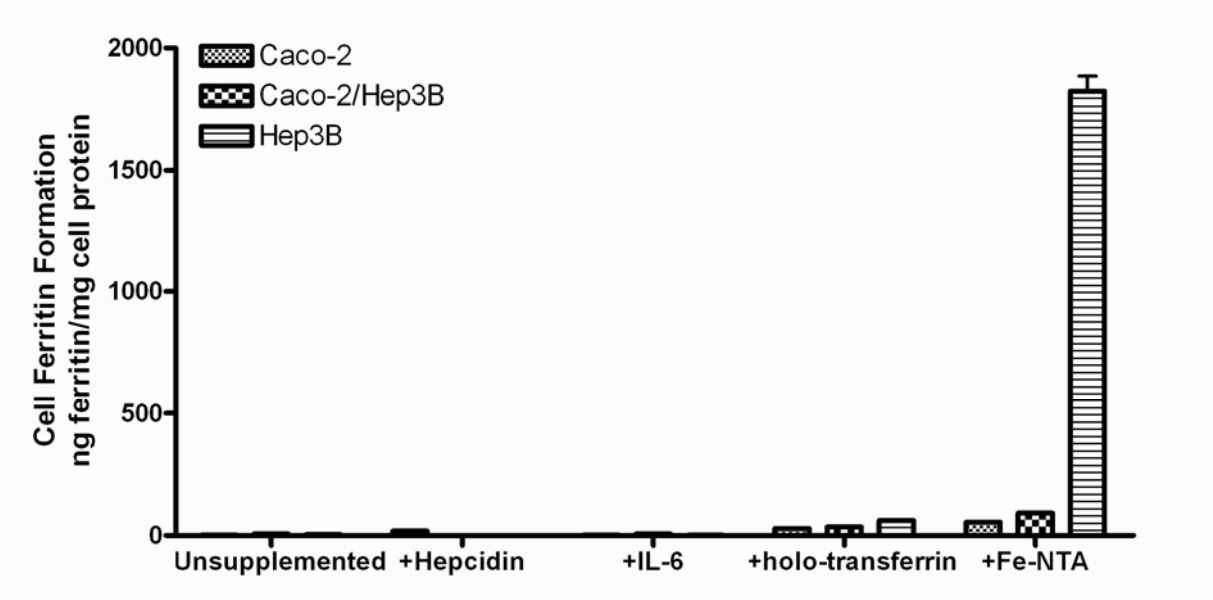

Figure A.3. Caco-2, Caco-2/Hep3B, and Hep3B ferritin formation results.

Culture medium was assayed for hepcidin using a pro-hepcidin ELISA. All results were negative for the peptide. Medium samples were then analyzed with electrospray single quadrupole mass spectrometry, MALDI-TOF mass spectrometry, and Q trap electrospray ionization-based hybrid triple quadrupole/linear ion trap mass spectrometry, but hepcidin was not detected.

A.4. Conclusions

These results show that there are interesting differences in iron transport when Caco-2 and Hep3B cells are co-cultured and exposed to iron loaded conditions, iron deficient conditions, or IL-6. Hepcidin could not be detected in the culture medium (except for in the cultures treated with 10 μm hepcidin), however, even with one the most sensitive mass spectrometers available. Hepcidin may be produced by Hep3B

cells and hepcidin may be what is affecting the iron transport in Caco-2 cells, but proving the peptide is present would be necessary before making this claim.

REFERENCES

1. Conrad ME, Umbreit JN. 2002. Pathways of iron absorption. *Blood Cells, Molecules, and Diseases*. 29(3):336-355.

2. Andrews NC. 1999. Disorders of iron metabolism. *The New England Journal of Medicine*. 341(26):1986-1995.

3. Fleming RE, Bacon BR. 2005. Orchestration of iron homeostasis. *New England Journal of Medicine*. 352(17):1741-1744.

4. Nemeth E, Roetto A, Garozzo G, Ganz T, Camaschella C. 2005. Hepcidin is decreased in TFR2 hemochromatosis. *Blood*. 105(4):1803-1806.

5. Celec P. 2005. Hemojuvelin: A supposed role in iron metabolism one year after its discovery. *Journal of Molecular Medicine*. 83(7):521-525.

6. Nemeth E, Tuttle MS, Powelson J, Vaughn MB, Donovan A, Ward DM, Ganz T, Kaplan J. 2004. Hepcidin regulates cellular iron efflux by binding to ferroportin and inducing its internalization. *Science*. 306:2090-2093.

7. Nemeth E, Valore EV, Territo M, Schiller G, Lichtenstein A, Ganz T. 2003. Hepcidin, a putative mediator of anemia and inflammation, is a type II acute phase protein. *Blood*. 101:2461-2463.

8. Krause A, Neitz S, Magert HJ, Schulz A, Forssmann WG, Schula-Knappe P, Adermann K. 2000. Leap-1, a novel highly disulfide-bonded human peptide, exhibits antimicrobial activity. *FEBS Letters*. 480:147-150.

9. Lee P, Peng H, Gelbart T, Beutler E. 2004. The IL-6 and lipopolysaccharide-induced transcription of hepcidin in HFE-, transferrin receptor 2-, and B2-microglobulin-deficient hepatocytes. *Proceedings of the National Academy of Sciences*. 101(25):9263-9265.

10. Gangloff MB, Lai C, Van Campen D, Miller DD, Norvell WA, Glahn RP. 1996. Ferrous iron uptake but not transfer is down-regulated in Caco-2 cells grown in high iron serum-free medium. *Journal of Nutrition*. 126:3118-3127.

11. Munoz-Galarza JO. 2002. Development of an *in vitro* microscale cell culture analog of the intestinal epithelium [Master of Science]. Ithaca: Cornell University, Department of Chemical Engineering.

12. Han OH, Wessling-Resnick M. 2002. Copper repletion enhances apical iron uptake and transepithelial iron transport by Caco-2 cells. *American Journal of Physiology-Gastrointestinal and Liver Physiology*. 282(3):G527-G533.

13. Nemeth E, Rivera S, Gabayan V, Keller C, Taudorf S, Pedersen BK, Ganz T.

2004. IL-6 mediates hypoferremia of inflammation by inducing the synthesis of the iron regulatory hormone hepcidin. *The Journal of Clinical Investigation*. 113(9):1271-1276.

14. Lin L, Nemeth E, Rivera S, Gabayan V, Ganz T. 2004. *In vitro* analysis of iron regulated hepcidin expression. Abstract #130.3. Experimental Biology, April 17th-April 21st; Washington D.C.

APPENDIX B

DESIGN CALCULATIONS FOR THE SECOND GENERATION CHIP μCCA

Definitions

$\mu m := 10^{-6} m$ $\mu L := 10^{-6} L$ $Poise := \frac{Pa \cdot s}{10}$ $cP := \frac{Poise}{100}$

$\rho := 1.1 \frac{gm}{mL}$ Density of culture medium at 37 ° C. From Sun HB and H Yokota. Bone (2000) 28(3): 303.

$h_1 := 30 \cdot \mu m$ $h_2 := 100 \mu m$

$\nu := 0.03 \cdot \frac{cm^2}{s}$ Kinematic viscosity of culture medium at 37 ° C. Taken from Sun HB and H Yokota. Bone (2000) 28(3): 303.

$\mu := \rho \cdot \nu$ $\mu = 3.3 \times 10^{-3} Pa \cdot s$ dynamic viscosity of culture medium at 37° C.

$d_{cl} := 8 \mu m$ diameter of cells

$h_{cl} := \begin{pmatrix} 4 \\ 4 \\ 4 \\ 4 \end{pmatrix} \cdot \mu m$ height of cells

$V_{cell} := \frac{\pi}{4} \cdot d_{cl}^2 \cdot h_{cl}$ $V_{cell} = \begin{pmatrix} 201.062 \\ 201.062 \\ 201.062 \\ 201.062 \end{pmatrix} \mu m^3$ Volume of cell assuming spherical geometry

$A_{cell} := \frac{\pi}{4} \cdot d_{cl}^2$ $A_{cell} = 50.265\ \mu m^2$ Area of cell assuming spherical geometry

$Nch := 4$ Number of chambers

$chambers = \begin{pmatrix} liver \\ fat \\ kidney \\ marrow \end{pmatrix}$

$w_{ch} := \begin{pmatrix} 8.25 \\ 0.5 \\ 3.1 \\ 7.5 \end{pmatrix} \cdot mm$ width of chambers

$L_{ch} := \begin{pmatrix} 8.25 \\ 114.9596 \\ 3.1 \\ 7.5 \end{pmatrix} \cdot mm$ length of chambers

$$h_{ch} := \begin{pmatrix} h_1 \\ h_2 \\ h_1 \\ h_1 \end{pmatrix}$$ depth of chambers

$$Q_{ch} := \begin{pmatrix} 1.47 \\ 0.25 \\ 1.26 \\ 0.61 \end{pmatrix} \cdot \frac{\mu L}{min}$$ flowrate through each chamber

$$Q_f := \sum_{i=0}^{Nch-1} Q_{ch_i} \qquad Q_f = 3.59 \frac{\mu L}{min}$$ Flow rate from pump @ 0.75 rpm

$$uav_{ch} := \left(\left| \begin{array}{l} \text{for } i \in 0, 1 .. Nch - 1 \\ \quad uav_{ch_i} \leftarrow \dfrac{Q_{ch_i}}{h_{ch_i} \cdot w_{ch_i}} \\ uav_{ch} \end{array} \right. \right)$$

$$\tau_{ch} := \left| \begin{array}{l} \text{for } i \in 0, 1 .. Nch - 1 \\ \quad \tau_{ch_i} \leftarrow \dfrac{w_{ch_i} \cdot L_{ch_i} \cdot \left(h_{ch_i} - h_{cl_i} \right)}{Q_{ch_i}} \\ \tau_{ch} \end{array} \right.$$

$$uav_{ch} = \begin{pmatrix} 98.99 \\ 83.333 \\ 225.806 \\ 45.185 \end{pmatrix} \frac{\mu m}{s}$$ Linear velocity

$$\tau_{ch} = \begin{pmatrix} 1.204 \\ 22.072 \\ 0.198 \\ 2.398 \end{pmatrix} min$$ Residence time in each chamber

$$\gamma := \left| \begin{array}{l} \text{for } i \in 0, 1 .. Nch - 1 \\ \quad \gamma_i \leftarrow \dfrac{8 \cdot \dfrac{Q_{ch_i}}{w_{ch_i} \cdot h_{ch_i}} \cdot \mu}{h_{ch_i} - h_{cl_i}} \\ \gamma \end{array} \right.$$

$$\gamma = \begin{pmatrix} 1.005 \\ 0.229 \\ 2.293 \\ 0.459 \end{pmatrix} \frac{dyne}{cm^2}$$ Shear stress per unit area on cells

$$N_c := \left| \begin{array}{l} \text{for } i \in 0, 1 .. Nch - 1 \\ \quad N_{c_i} \leftarrow 4 \cdot \dfrac{w_{ch_i} \cdot L_{ch_i}}{\pi \cdot d_{cl}^{\,2}} \\ N_c \end{array} \right.$$

$$N_c = \begin{pmatrix} 1.354 \times 10^6 \\ 1.144 \times 10^6 \\ 1.912 \times 10^5 \\ 1.119 \times 10^6 \end{pmatrix}$$ Number of cells in each chamber if confluent

$$D_H := \left| \begin{array}{l} \text{for } i \in 0, 1 .. Nch - 1 \\ \quad D_{H_i} \leftarrow \dfrac{4 \cdot w_{ch_i} \cdot \left(h_{ch_i} - h_{cl_i} \right)}{2 \cdot w_{ch_i} + 2 \cdot \left(h_{ch_i} - h_{cl_i} \right)} \\ D_H \end{array} \right.$$

$$D_H = \begin{pmatrix} 51.837 \\ 161.074 \\ 51.567 \\ 51.82 \end{pmatrix} \mu m$$ Hydraulic diameter

$$Re_H := \left| \begin{array}{l} \text{for } i \in 0, 1 .. Nch - 1 \\ \quad Re_{H_i} \leftarrow \dfrac{D_{H_i} \cdot \dfrac{Q_{ch_i}}{w_{ch_i} \cdot \left(h_{ch_i} - h_{cl_i} \right)} \cdot \rho}{\mu} \\ Re_H \end{array} \right.$$

$$Re_H = \begin{pmatrix} 1.974 \times 10^{-3} \\ 4.661 \times 10^{-3} \\ 4.479 \times 10^{-3} \\ 9.006 \times 10^{-4} \end{pmatrix}$$

Reynolds number based on hydraulic diameter.
Flow is laminar because Re < 2100

$$f_{ch} := \frac{16}{Re_H} \qquad f_{ch} = \begin{pmatrix} 8.107 \times 10^{3} \\ 3.433 \times 10^{3} \\ 3.573 \times 10^{3} \\ 1.777 \times 10^{4} \end{pmatrix}$$ friction factor for each chamber

$$Pd_{ch} := \left| \begin{array}{l} \text{for } i \in 0, 1 .. Nch - 1 \\ \quad Pd_{ch_i} \leftarrow \frac{2 \cdot L_{ch_i}}{D_{H_i}} \cdot \left[\frac{Q_{ch_i}}{w_{ch_i} \cdot \left(h_{ch_i} - h_{cl_i} \right)} \right]^2 \cdot \rho \cdot f_{ch_i} \\ Pd_{ch} \end{array} \right.$$

$$Pd_{ch} = \begin{pmatrix} 37.033 \\ 40.617 \\ 32.074 \\ 15.377 \end{pmatrix} Pa$$ Pressure drop through chambers

Pressure drop through the distributors is calculated with the Ergun equation (Treybal, Mass Transfer Ops, 3rd ed., pg 200; TP155.T81 @ Carpenter)

$w_{baf} := 100 \cdot \mu m$ width of baffles. Left these at 100 because the P drop is smaller and easier to balance

$h_{baf} := 30 \cdot \mu m$ height of baffles

$\varepsilon := 0.75$ void fraction

$$w_{bafin} := \begin{pmatrix} 342 \\ 63 \\ 263 \\ 139 \end{pmatrix} \cdot \mu m$$ Width of distributor inlet

$L_{baf} := 0.5 \cdot w_{ch}$ Length of distributor

$$V_{dist} := \varepsilon \cdot L_{baf} \cdot w_{baf} \cdot h_{baf}$$

$$V_{dist} = \begin{pmatrix} 9.281 \times 10^{-3} \\ 5.625 \times 10^{-4} \\ 3.487 \times 10^{-3} \\ 8.437 \times 10^{-3} \end{pmatrix} \mu L$$ Volume of distributors

The distributor is not a straight channel, therefore there is a dependence of velocity on length. These equations are derived from the Ergun equation for a right triangular entrance.

$$A := \frac{150 \cdot Q_{ch} \cdot (1 - \varepsilon)^2 \cdot \mu}{\varepsilon^3 \cdot w_{baf}^2 \cdot h_{baf}}$$

$$B := \frac{1.75 \cdot Q_{ch}^2 \cdot \rho \cdot (1 - \varepsilon)}{\varepsilon^3 \cdot w_{baf} \cdot h_{baf}^2}$$

$$A = \begin{pmatrix} 5.989 \\ 1.019 \\ 5.133 \\ 2.485 \end{pmatrix} \frac{mg}{\mu m \cdot s^2} \qquad B = \begin{pmatrix} 7.608 \\ 0.22 \\ 5.59 \\ 1.31 \end{pmatrix} \frac{mg}{s^2}$$

$$Pd_{baf} := \left| \begin{array}{l} \text{for } i \in 0, 1 .. Nch - 1 \\ \quad Pd_{baf_i} \leftarrow A_i \cdot \ln\left(\frac{L_{baf_i} + w_{bafin_i}}{w_{bafin_1}} \right) - B_i \cdot \left(\frac{1}{L_{baf_i} + w_{bafin_1}} - \frac{1}{w_{bafin_1}} \right) \\ Pd_{baf} \end{array} \right.$$

$$Pd_{baf} = \begin{pmatrix} 15.41 \\ 1.636 \\ 9.929 \\ 8.288 \end{pmatrix} Pa$$ Pressure drop through the distributors

The chamber exit has no baffles and is shorter (30/30/120 triangles with a trimmed top)

$w_{chex} := w_{bafin}$ width of chamber exit

$$L_{chin} := \frac{w_{ch}}{\tan\left(\frac{\pi}{3}\right)}$$ beginning of trimmed top exit

$$L_{chex} := L_{chin} - \frac{w_{chex}}{2 \cdot \tan\left(\frac{\pi}{3}\right)} \qquad L_{chex} = \begin{pmatrix} 4.664 \\ 0.27 \\ 1.714 \\ 4.29 \end{pmatrix} mm$$ end of exit from chamber

$$Pd_{chex} := \left| \begin{array}{l} \text{for } i \in 0, 1 .. Nch - 1 \\ \quad Pd_{chex_i} \leftarrow \dfrac{-32 \cdot \mu \cdot Q_{ch_i}}{h_{ch_i}} \cdot \displaystyle\int_{L_{chin_i}}^{L_{chex_i}} \left(\dfrac{1}{2 \cdot h_{ch_i}} + \dfrac{1}{2 \cdot x \cdot \tan\left(\frac{\pi}{3}\right)} \right)^3 dx \\ \\ Pd_{chex} \end{array} \right.$$

$$Pd_{chex} = \begin{pmatrix} 39.854 \\ 0.018 \\ 26.76 \\ 6.728 \end{pmatrix} Pa$$

$$Pd_{chambers} := Pd_{ch} + Pd_{baf} + Pd_{chex}$$

$$Pd_{chambers} = \begin{pmatrix} 92.296 \\ 42.27 \\ 68.763 \\ 30.394 \end{pmatrix} Pa$$

Pressure drop for all chambers and their distributors and exits, fat is actually only Pd_{ch} because it is just connected channels

Channel (piping) dimensions

$$w_p := \begin{pmatrix} 342 \\ 63 \\ 263 \\ 139 \end{pmatrix} \cdot \mu m \qquad L_p := \begin{pmatrix} 21.209 \\ 10.3378 \\ 22.6822 \\ 22.6568 \end{pmatrix} \cdot mm \qquad h_p := \begin{pmatrix} 100 \\ 100 \\ 100 \\ 100 \end{pmatrix} \cdot \mu m$$

$$Q_p := Q_{ch} \qquad Q_p = \begin{pmatrix} 1.47 \\ 0.25 \\ 1.26 \\ 0.61 \end{pmatrix} \frac{\mu L}{min}$$

flowrate into each channel

$Nstreams := 4$ 4 fluid pathways

$Nbend_p := \begin{pmatrix} 2 \\ 4 \\ 4 \\ 2 \end{pmatrix}$ number of bends in pathways

$P_p := 2 \cdot w_p + 2 \cdot h_p$ $P_p = \begin{pmatrix} 884 \\ 326 \\ 726 \\ 478 \end{pmatrix} \mu m$ Perimeter of pipes

$u_{av} := \left| \begin{array}{l} \text{for } i \in 0, 1 .. Nstreams - 1 \\ \quad u_{av_i} \leftarrow \dfrac{Q_{p_i}}{w_{p_i} \cdot h_{p_i}} \\ u_{av} \end{array} \right.$ $u_{av} = \begin{pmatrix} 0.716 \\ 0.661 \\ 0.798 \\ 0.731 \end{pmatrix} \dfrac{mm}{s}$ Average velocity in each pipe section

$D_{Hp} := \left| \begin{array}{l} \text{for } i \in 0, 1 .. Nstreams - 1 \\ \quad D_{Hp_i} \leftarrow \dfrac{4 w_{p_i} \cdot h_{p_i}}{P_{p_i}} \\ D_{Hp} \end{array} \right.$ $D_{Hp} = \begin{pmatrix} 154.751 \\ 77.301 \\ 144.904 \\ 116.318 \end{pmatrix} \mu m$ Hydraulic diameter

$Re_{Hp} := \left| \begin{array}{l} \text{for } i \in 0, 1 .. Nstreams - 1 \\ \quad Re_{Hp_i} \leftarrow \dfrac{D_{Hp_i} \cdot u_{av_i} \cdot \rho}{\mu} \\ Re_{Hp} \end{array} \right.$ $Re_{Hp} = \begin{pmatrix} 0.037 \\ 0.017 \\ 0.039 \\ 0.028 \end{pmatrix}$ Hydraulic Reynold's number for pipes, flov is laminar because Re < 2100

$$f_p := \frac{16}{Re_{Hp}} \qquad f_p = \begin{pmatrix} 432.98 \\ 938.88 \\ 414.857 \\ 564.197 \end{pmatrix}$$

Friction factor for laminar flow in pipes

$K := 1.5$ Pressure drop for fitting (T, side outlet), K~1.5

$$Pd_p := \left| \begin{array}{l} \text{for } i \in 0, 1 .. Nstreams - 1 \\ \quad Pd_{p_i} \leftarrow \frac{2 \cdot L_{p_i}}{D_{Hp_i}} \cdot \left(u_{av_i}\right)^2 \cdot \rho \cdot f_{p_i} \\ Pd_p \end{array} \right. \qquad Pd_p = \begin{pmatrix} 66.997 \\ 120.83 \\ 91.087 \\ 129.34 \end{pmatrix} Pa$$

Pressure drop for channels

$$Pd_f := \left| \begin{array}{l} \text{for } i \in 0, 1 .. Nstreams - 1 \\ \quad Pd_{f_i} \leftarrow \frac{K \cdot \left(u_{av_i}\right)^2 \cdot \rho}{2} \cdot Nbend_{p_i} \\ Pd_f \end{array} \right. \qquad Pd_f = \begin{pmatrix} 8.468 \times 10^{-4} \\ 1.443 \times 10^{-3} \\ 2.104 \times 10^{-3} \\ 8.827 \times 10^{-4} \end{pmatrix} Pa$$

Pressure drop for fittings

$Pd_{stream} := Pd_{chambers} + Pd_p + Pd_f$

$$Pd_{stream} = \begin{pmatrix} 159.294 \\ 163.101 \\ 159.852 \\ 159.734 \end{pmatrix} Pa$$

These values should be within ~5% of each other

$Pd_{fat} := Pd_{ch} + Pd_p + Pd_f$ $\qquad Pd_{fat} = \begin{pmatrix} 104.031 \\ 161.448 \\ 123.163 \\ 144.718 \end{pmatrix} Pa$

fat is 2nd value down

Summary

$$Pd_{stream} = \begin{pmatrix} 159.294 \\ 163.101 \\ 159.852 \\ 159.734 \end{pmatrix} Pa \qquad Q_{ch} = \begin{pmatrix} 1.47 \\ 0.25 \\ 1.26 \\ 0.61 \end{pmatrix} \frac{\mu L}{min}$$

$$w_p = \begin{pmatrix} 342 \\ 63 \\ 263 \\ 139 \end{pmatrix} \mu m \qquad Q_f = 3.59 \frac{\mu L}{min}$$

$$V_{chip} := \sum_{i=0}^{Nstreams-1} w_{p_i} \cdot L_{p_i} \cdot h_{p_i} + \left[\sum_{j=0}^{Nch-1} \left[w_{ch_j} \cdot L_{ch_j} \cdot \left(h_{ch_j} - h_{cl_j} \right) + V_{dist_j} \right] \right]$$

$V_{chip} = 10.724\,\mu L$ Total volume of chip

$$\tau_{chip} := \frac{V_{chip}}{Q_f}$$

$\tau_{chip} = 179.227\,s$ Total residence time on chip

APPENDIX C

SECOND GENERATION μCCA SYSTEM PBPK CODE

```
%PBPK model for acetaminophen in human configuration
%Acetaminophen (APAP) metabolized to NAPQI, APAP-GLUC, APAP-SULF

function [t,x] = PBPK(APAP,timespan)

%{
x(1): APAP in lumen
x(2): APAP in GI
x(3): APAP in liver
x(4): APAP in kidney
x(5): APAP in marrow
x(6): APAP fat
x(7): APAP in well perfused organs (lung)
x(8): APAP in poorly perfused organs (muscle)
x(9): APAP in blood plasma
%}

% concentration (nmol/ml or nmol/g)
init_cond = zeros(9,1);

init_cond(1) = APAP;
init_cond(2) = 0;
init_cond(3) = 0;
init_cond(4) = 0;
init_cond(5) = 0;
init_cond(6) = 0;
init_cond(7) = 0;
init_cond(8) = 0;
init_cond(9) = 0;

% time span in hour
time=[0 timespan*60];
[t,x] = ode45(@PBPK_ODE,time,init_cond);

% function definition
function dxdt=PBPK_ODE(t,x)

dxdt = zeros(9,1);

% parameters

% organ size (ml); Tox. Ind. Health. 13(4):407
V_LMN = 1000;
V_G = 1190;
V_L = 1820;
V_K = 280;
```

```
V_M = 1400;
V_F = 14980;
V_W = 560;
V_P = 28000;
V_B = 5530;

% flow rates (ml/min); Tox. Ind. Health. 13(4):407, Handbook of
Essential Pharmacokinetics, Pharmacodynamics and Drug Metabolism for
Industrial Scientists.
Q_G = 1100;
Q_L = 1450;
Q_K = 1240;
Q_M = 120;
Q_F = 260;
Q_W = 1400;
Q_P = 750;
Q_B = 5600;

% Partition coefficients; J. Pharm. Sci. (2002)91(1):129
P_APAP_G = 0.795;
P_APAP_L = 0.831;
P_APAP_K = 0.85;
P_APAP_M = 0.5;
P_APAP_F = 0.513;
P_APAP_W = 0.864;
P_APAP_P = 0.819;

% enzyme kinetic parameters
Vm_CYP_L = 328;     % nmol/min/g; Chem. Res. Toxicol. (1993)6:511
Km_CYP_L = 677;     % nmol/mL
Vm_AG_L = 2.76;     % nmol/min/g; J. Pharmaco.
                    Biopharm.(1983)11(3):245
Km_AG_L = 915;      % nmol/mL
Vm_AS_L = 4.92;     % nmol/min/g; J. Pharmaco.
                    Biopharm.(1983)11(3):245
Km_AS_L = 109;      % nmol/mL

Kabs_APAP = 0.354;  % 1/hr, Kabs = 2*Peff/R, R = 1.75, Peff = 0.3096
                    cm/hr; Int. J. Pharm. (1999)20(2):119

% Unbound fraction
f_B_APAP = 1;

% ODEs
% APAP_LMN
dxdt(1) = (-1*Kabs_APAP*x(1)*V_LMN)/V_LMN;
% APAP_G
dxdt(2) = (Kabs_APAP*x(1)*V_LMN + Q_G*x(9) - Q_G*x(2)/P_APAP_G)/V_G;
% APAP_L
dxdt(3) = (((Q_L-Q_G)*x(9) - Q_L*x(3)/P_APAP_L + Q_G*x(2)/P_APAP_G -
Vm_CYP_L*f_B_APAP*x(3)/(Km_CYP_L+(f_B_APAP*x(3)))-
Vm_AS_L*f_B_APAP*x(3)/(Km_AS_L+(f_B_APAP*x(3)))-
Vm_AG_L*f_B_APAP*x(3)/(Km_AG_L+(f_B_APAP*x(3))))*V_L)/V_L;
```

```
% APAP_K
dxdt(4) = (Q_K*x(9) - Q_K*x(4)/P_APAP_K)/V_K;
% APAP_M
dxdt(5) = (Q_M*x(9) - Q_M*x(5)/P_APAP_M)/V_M;
% APAP_F
dxdt(6) = (Q_F*x(9) - Q_F*x(6)/P_APAP_F)/V_F;
% APAP_W
dxdt(7) = (Q_W*x(9) - Q_W*x(7)/P_APAP_W)/V_W;
% APAP_P
dxdt(8) = (Q_P*x(9) - Q_P*x(5)/P_APAP_P)/V_P;
% APAP_B
dxdt(9) = (Q_L*x(3)/P_APAP_L + Q_K*x(4)/P_APAP_K + Q_M*x(5)/P_APAP_M
+ Q_F*x(6)/P_APAP_F + Q_W*x(7)/P_APAP_W + Q_P*x(8)/P_APAP_P -
Q_B*x(9))/V_B;
```

```
%PBPK model for acetaminophen in chip configuration
%Acetaminophen (APAP) metabolized to NAPQI, APAP-GLUC, APAP-SULF

function [t,x] = PBPK(APAP,timespan)

%{
x(1): APAP in lumen
x(2): APAP in GI
x(3): APAP in liver
x(4): APAP in kidney
x(5): APAP in marrow
x(6): APAP fat
x(7): APAP in well perfused organs (lung)
x(8): APAP in poorly perfused organs (muscle)
x(9): APAP in blood plasma
%}

% concentration (nmol/ml or nmol/g)
init_cond = zeros(9,1);

init_cond(1) = APAP;
init_cond(2) = 0;
init_cond(3) = 0;
init_cond(4) = 0;
init_cond(5) = 0;
init_cond(6) = 0;
init_cond(7) = 0;
init_cond(8) = 0;
init_cond(9) = 0;

% time span in hour
time=[0 timespan*60];
[t,x] = ode45(@PBPK_ODE,time,init_cond);

% function definition
function dxdt=PBPK_ODE(t,x)

dxdt = zeros(9,1);

% parameters

% organ size (ml); Tox. Ind. Health. 13(4):407
V_LMN = 1000;
V_G = 1190;
V_L = 1820;
V_K = 280;
V_M = 1400;
V_F = 14980;
V_W = 560;
V_P = 28000;
V_B = 5530;
```

```
% flow rates (ml/min); Tox. Ind. Health. 13(4):407, Handbook of
Essential Pharmacokinetics, Pharmacodynamics and Drug Metabolism for
Industrial Scientists.
Q_G = 1100;
Q_L = 1450;
Q_K = 1240;
Q_M = 120;
Q_F = 260;
Q_W = 1400;
Q_P = 750;
Q_B = 5600;

% Partition coefficients; J. Pharm. Sci. (2002)91(1):129
P_APAP_G = 0.795;
P_APAP_L = 0.831;
P_APAP_K = 0.85;
P_APAP_M = 0.5;
P_APAP_F = 0.513;
P_APAP_W = 0.864;
P_APAP_P = 0.819;

% enzyme kinetic parameters
Vm_CYP_L = 328;     % nmol/min/g; Chem. Res. Toxicol. (1993)6:511
Km_CYP_L = 677;     % nmol/mL
Vm_AG_L = 2.76;     % nmol/min/g; J. Pharmaco.
                    Biopharm.(1983)11(3):245
Km_AG_L = 915;      % nmol/mL
Vm_AS_L = 4.92;     % nmol/min/g; J. Pharmaco.
                    Biopharm.(1983)11(3):245
Km_AS_L = 109;      % nmol/mL

Kabs_APAP = 0.354;  % 1/hr, Kabs = 2*Peff/R, R = 1.75, Peff = 0.3096
                    cm/hr; Int. J. Pharm. (1999)20(2):119

% Unbound fraction
f_B_APAP = 1;

% ODEs
% APAP_LMN
dxdt(1) = (-1*Kabs_APAP*x(1)*V_LMN)/V_LMN;
% APAP_G
dxdt(2) = (Kabs_APAP*x(1)*V_LMN + Q_G*x(9) - Q_G*x(2)/P_APAP_G)/V_G;
% APAP_L
dxdt(3) = 0.41*((((Q_L-Q_G)*x(9) - Q_L*x(3)/P_APAP_L +
Q_G*x(2)/P_APAP_G -
Vm_CYP_L*f_B_APAP*x(3)/(Km_CYP_L+(f_B_APAP*x(3)))-
Vm_AS_L*f_B_APAP*x(3)/(Km_AS_L+(f_B_APAP*x(3)))-
Vm_AG_L*f_B_APAP*x(3)/(Km_AG_L+(f_B_APAP*x(3))))*V_L)/V_L);
% APAP_K
dxdt(4) = 0.35*(((Q_K - Q_G)*x(9) - Q_K*x(4)/P_FT_K +
Q_G*x(2)/P_FT_G)/V_K);
% APAP_M
dxdt(5) = 0.17*(((Q_M - Q_G)*x(9) - Q_M*x(5)/P_FT_P +
Q_G*x(2)/P_FT_G)/V_M);
```

```
% APAP_F
dxdt(6) = 0.07*(((Q_F - Q_G)*x(9) - Q_F*x(6)/P_FT_F +
Q_G*x(2)/P_FT_G)/V_F);
% APAP_W
dxdt(7) = (Q_W*x(9) - Q_W*x(7)/P_APAP_W)/V_W;
% APAP_P
dxdt(8) = (Q_P*x(9) - Q_P*x(8)/P_APAP_P)/V_P;
% APAP_B
dxdt(9) = (Q_L*x(3)/P_APAP_L + Q_K*x(4)/P_APAP_K + Q_M*x(5)/P_APAP_M
+ Q_F*x(6)/P_APAP_F + Q_W*x(7)/P_APAP_W + Q_P*x(8)/P_APAP_P -
Q_B*x(9))/V_B;
```